On the design of broadband electrodynamical loudspeakers and multiway loudspeaker systems

ON THE DESIGN OF BROADBAND ELECTRODYNAMICAL LOUDSPEAKERS AND MULTIWAY LOUDSPEAKER SYSTEMS

ADRIANUS JOZEF MARIA KAIZER

ON THE DESIGN OF BROADBAND ELECTRODYNAMICAL LOUDSPEAKERS AND MULTIWAY LOUDSPEAKER SYSTEMS

PROEFSCHRIFT

ter verkrijging van de graad van doctor in de technische wetenschappen aan de Technische Hogeschool Eindhoven, op gezag van de rector magnificus, prof.dr. F.N. Hooge, voor een commissie aangewezen door het college van dekanen in het openbaar te verdedigen op dinsdag 14 januari 1986 te 16.00 uur

door

ADRIANUS JOZEF MARIA KAIZER

geboren te Amsterdam

Dit proefschrift is goedgekeurd door de
promotoren: Prof. Dr.-Ing. H.-J. Butterweck
Prof. Dr.Ir. J.G. Niesten

co-promotor: Dr.Ir. J.M. van Nieuwland

CIP-GEGEVENS KONINKLIJKE BIBLIOTHEEK, DEN HAAG

Kaizer, Adrianus Jozef Maria

On the design of broadband electrodynamical loudspeakers and multiway loudspeaker systems / Adrianus Jozef Maria Kaizer. - [S.l. : s.n.]. - Fig., tab.
Proefschrift Eindhoven. - Met lit. opg., reg.
ISBN 90-9001162-5
SISO 665.53 UDC 534.87 UGI 650
Trefw.: luidsprekers.

Dankbetuiging

Bij deze wil ik mijn dank uitspreken aan allen die in welke vorm dan ook hebben bijgedragen aan de totstandkoming van dit proefschrift, in het bijzonder aan:

De directie van het Philips Natuurkundig Laboratorium voor de mogelijkheid die mij geboden is dit proefschrift te schrijven en voor al de faciliteiten, welke mij ter beschikking zijn gesteld om deze publikatie te verwezenlijken.

Mijn kollega's van het Natuurkundig Laboratorium en in het bijzonder Ing. C.P. Janse voor de vele nuttige diskussies.

Table of contents

1. Introduction

A loudspeaker is a transducer that is designed to convert electric energy into acoustic energy. Its object is to generate an acoustic pressure wave[1], that resembles the electric signal as closely as possible.
This thesis discusses the design and optimization of an electrodynamic loudspeaker. The designer of such a loudspeaker can take advantage of a theoretical model, from which the behavior of a specific loudspeaker can be predicted. At low frequencies this model is relatively simple: the loudspeaker behaves as a rigid piston and the sound radiation is almost equal to that of a plane piston in a rigid baffle [1]. At higher frequencies some deviations from this simple model occur: the loudspeaker diaphragm is not rigid any more, it shows a "break-up". Also the influence of the cone depth on the sound radiation must be accounted for. Both effects exert an influence on the steady-state and transient response of the loudspeaker.

Section 2 of this thesis presents a description of a lumped parameter model of an electrodynamic loudspeaker, in terms of an electric analogous circuit. Such a simple model can be used to derive many properties of the loudspeaker and can serve as a basis for further discussions.

To judge the quality of a practical loudspeaker we need one or more figure(s) of merit for its behavior and some criteria for an optimum design.
To this end we consider a loudspeaker as a transmission system with the electrical voltage at the terminals as the input signal and the sound pressure at a space point (throughout assumed to lie on the loudspeaker axis) as the output signal. The interrelation between the input and output signal is quantitatively characterized by the impulse response or (equivalently) by the Fourier transform of this impulse response, the complex-valued transfer function, under the assumption that the loudspeaker can be viewed as a linear, time-invariant system.
The impulse response is defined as the sound pressure due to an electric Dirac impulse. An *ideal* loudspeaker can be defined such that its impulse response is a Dirac impulse itself. This implies that its acoustic response is a delayed replica of the electrical excitation. As a consequence the magnitude of its transfer function has a constant value as a function of frequency, while the phase response is linear.
However, these properties can be obtained in a limited frequency range only, because a nonvanishing response from DC to infinite frequencies is physically unrealizable. Therefore we define a *semi-ideal* loudspeaker as one for which the above requirements are satisfied only within the range of audible frequencies.
Particularly the magnitude of the transfer function of a semi-ideal loudspeaker has a constant value for all audible frequencies. This requirement is widely accepted [1,2]; it is checked with the aid of a swept sine wave as an electric excitation signal [3].
As for the transient response of a semi-ideal loudspeaker, many measurement methods and representations have been developed, for example the tone burst response and the cumulative spectra [4], but the interpretation and the formulation of an optimization criterion is problematic. Nevertheless, all information about the transient behavior of the loudspeaker is contained in its impulse response. The problem is then, how to extract this information from the impulse response, or to find a representation that allows the formulation of an optimization criterion for the transient behavior.
A new and promising representation for the transient behavior of a loudspeaker is the Wigner distribution of the impulse response. The Wigner distribution can be used to recognize some physical processes in a loudspeaker and to define an optimization criterion for its transient behavior. This Wigner distribution is discussed in Section 3.

The influence of the diaphragm break-up on the sound radiation can be predicted by calculating the vibrations of a nonrigid loudspeaker diaphragm numerically, which is the topic of Section 4.
The influence of the cone depth on the sound radiation is treated in Section 5.1. In that section we calculate the sound radiation from a radiating surface by solving the Helmholtz equation numerically.

The next point is the necessity to divide the total frequency range into different parts that are covered by separate loudspeakers. This makes it necessary to design a loudspeaker for each separate frequency range and yields the problem of how to combine different loudspeakers. To increase the freedom in combining different loudspeakers into one system we apply an electrical crossover network. The consequences of this network for the frequency response have been extensively discussed elsewhere [5,6]. A numerical technique for the optimization of the crossover network can be found in Ref. [34]. The network may also, however, affect the transient behavior, and this is discussed in Sections 5.2 and 5.3.

[1]) The human ear is an acoustic pressure receiver [1,28].

So far the loudspeaker has been assumed to be a linear system. However, an actual electrodynamic loudspeaker shows small nonlinearities that give rise to distortion components in its response. An overview of possible nonlinearities in a practical electrodynamic loudspeaker is given in Section 6. This section also presents a model of the nonlinear loudspeaker behavior, which can be used to predict the low frequency distortion of a loudspeaker.
Finally Section 7 presents some conclusions.

2. The lumped parameter model of an electrodynamic loudspeaker

The main part of an electrodynamic loudspeaker is a vibrating diaphragm radiating sound into space. The vibration of the diaphragm is maintained by an electrodynamic motor, i.e. an electrically driven voice coil in a static magnetic field. The construction of such a loudspeaker is shown in Fig. 2.1 for a cone-shaped loudspeaker. The diaphragm can be plane-, cone- or dome-shaped, the last especially for high-frequency loudspeakers.

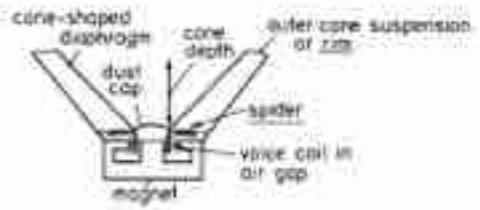

Fig. 2.1. Cross-section of an electrodynamic cone-type loudspeaker.

The diaphragm is suspended at the outer edge by means of a flexible surround or rim and at the inner edge by a so-called spider. This rotationally symmetrical spider centers the voice coil in the air gap of the magnet system. It has a small stiffness for axial and a much larger stiffness for radial movements of the voice coil. The air gap has a static radial magnetic field, which is maintained by a permanent magnet.
The simplified mechanical behavior of the loudspeaker is that of a mass-spring system. The spring is formed by the outer edge suspension and the spider[1]. The mass is formed by the diaphragm, the voice coil, the effective suspension moving mass and the mass of the air load.
Again in a simplifying model, the sound radiation can be viewed as a one-port with a certain "radiation impedance". This view excludes the description of directional effects, but admits a correct interpretation in terms of power: the power dissipated in the one-port is the radiated sound power.
The simple mass-spring model and the one-port model of the sound radiation together form the "lumped parameter model" of a loudspeaker. It allows the formulation of some approximate analytical expressions for the loudspeaker sound radiation due to an electrical input voltage.

[1]) A loudspeaker is usually mounted in a closed box with a limited volume. This acoustic box volume at the back of the diaphragm acts as a mechanical spring at low frequencies. In our model this spring, which cannot be neglected, is incorporated in the spider spring constant.

The lumped parameter model of the loudspeaker involves the following assumptions:

- The diaphragm of the loudspeaker is rigid, i.e. the shape of the diaphragm does not alter when the diaphragm is in motion.
- The radiation impedance is equal to that of a plane, rigid piston in an infinite baffle, the influence of the nonplane shape of the diaphragm on the radiation impedance being ignored. This is a good approximation at low frequencies, where the wavelength is much larger than the cone depth or dome height.

The properties of such a rigid diaphragm loudspeaker can be represented in an electrical analogon, the so-called impedance-type analogous circuit of Fig. 2.2 [7]. In the analogous circuit the relations between the electrical and mechanical quantities are represented by a gyrator.

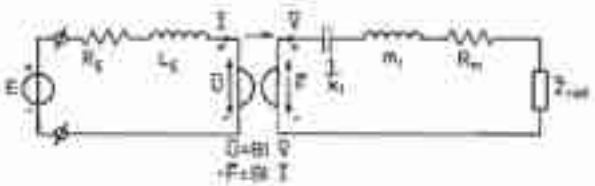

Fig. 2.2. Impedance-type analogous circuit for an electrodynamic loudspeaker.

The parameters in the circuit are:

R_E	: electrical resistance of the voice coil	[Ω]
L_E	: inductivity of the voice coil[2]	[H]
$\bar{I}$	: voice coil current	[A]
$\bar{U}$	: induced voltage in the voice coil due to its motion	[V]
B	: air gap flux density	[T]
l	: effective length of the voice coil wire	[m]
$\bar{F}$	: Lorentz force on the voice coil	[N]
$\bar{V}$	: velocity of the voice coil	[m/s]
k_t	: total spring constant	[N/m]
m_t	: total moving mass, without air load mass	[kg]
R_m	: mechanical damping (force over velocity)	[N.s/m]

The mechanical radiation impedance $\bar{Z}_{rad}$ can be written in the form:

$$\bar{Z}_{rad} = R_{rad}(\omega) + \mathrm{j}\, X_{rad}(\omega)\,, \qquad 2.1$$

and its frequency dependence is shown in Fig. 2.3.

[2]) This inductivity exhibits a weak frequency dependence due to eddy currents in the iron central pole.

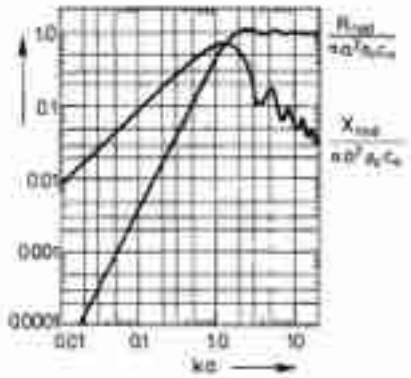

Fig. 2.3. The normalized real and imaginary parts of the mechanical radiation impedance of a plane, circular and rigid piston in an infinite baffle versus frequency. k is the wave number and a is the radius of the piston. (After Beranek [1])

The quantity $X_{rad}(\omega)/\omega$ is the "air load mass" m_1, which is constant at low frequencies.
For a plane, circular and rigid piston in an infinite baffle the following low- and high-frequency approximations are valid [1,8]:

$$\overline{Z}_{rad} = \frac{\rho_0 \omega^2 \pi a^4}{2 c_0} + j \frac{8 \rho_0 \omega a^3}{3}, \text{ for } \omega \ll \omega_1, \qquad 2.2$$

$$\overline{Z}_{rad} = \rho_0 c_0 \pi a^2 + j \frac{2 \rho_0 c_0^2 a}{\omega}, \text{ for } \omega \gg \omega_1, \qquad 2.3$$

where ρ_0 is the density of air, c_0 is the sound velocity, a is the radius of the piston and ω is the angular frequency.
The circular frequency where the acoustical wavelength equals the circumference of the piston is the transition frequency:

$$\omega_1 = \frac{c_0}{a}. \qquad 2.4$$

If we add the air load mass m_1 (due to the radiation impedance) to the transducer masses we get the total moving mass:

$$m_t = m_1 + m_t. \qquad 2.5$$

Many properties of the loudspeaker can be derived from this simplified model. As an example we derive an expression for the efficiency of the loudspeaker at low frequencies. Also we discuss the frequency dependence of the sound power response under constant-amplitude electrical excitation.

2.1 The loudspeaker efficiency as a function of the frequency

The transducer vibratory behavior of. Fig. 2.2, is that of a simple mass-spring system:

$$\overline{F} = \left(R_m + j \omega m_t + \frac{k_t}{j\omega} + R_{rad}\right) \overline{V}. \qquad 2.6$$

The electrical source is loaded by the impedance

$$\overline{Z}_t = R_E + j\omega L_E + \frac{(Bl)^2}{(R_m + R_{rad}) + j\left(\omega m_t - \frac{k_t}{\omega}\right)} \qquad 2.7$$

The influence of the inductivity L_E is relatively weak and will be ignored throughout the remaining part of this section.
The power supplied by the generator equals:

$$P_E = \tfrac{1}{2} \overline{I}\, \overline{I}^* \, \mathrm{Re}\{\overline{Z}_t\} = \tfrac{1}{2} \overline{I} \left\{ R_E + \frac{(Bl)^2 (R_m + R_{rad})}{(R_m + R_{rad})^2 + \left(\omega m_t - \frac{k_t}{\omega}\right)^2} \right\}, \qquad 2.8$$

where Re means "real part of" and $\hat{I} = |\overline{I}|$ stands for the amplitude of the current.
The radiated power is given by

$$P_a = \tfrac{1}{2} \overline{V}\, \overline{V}^* \, \mathrm{Re}\{\overline{Z}_{rad}\} = \tfrac{1}{2} \hat{V}^2 R_{rad}. \qquad 2.9$$

Combination of $-\overline{F} = Bl\,\overline{I}$ and Eqs. 2.6 and 2.9 yields

$$P_a = \tfrac{1}{2} \frac{(Bl)^2 \hat{I}^2 R_{rad}}{(R_m + R_{rad})^2 + \left(\omega m_t - \frac{k_t}{\omega}\right)^2}. \qquad 2.10$$

It is convenient to introduce three dimensionless variables: the mechanical, electrical and acoustical quality factors Q_m, Q_E and Q_{rad}:

$$Q_m = \frac{1}{R_m} (k_t m_t)^{1/2}, \qquad 2.11$$

$$Q_E = \frac{R_E}{(Bl)^2} (k_t m_t)^{1/2}, \qquad 2.12$$

$$Q_{rad} = \frac{1}{R_{rad}} (k_t m_t)^{1/2}, \qquad 2.13$$

the last being frequency-dependent.
The electrical quality factor Q_E is independent of the voice coil wire length L. It can easily be shown that the resistance R_E equals

$$R_E = \frac{\sigma_w L^2}{V_w}, \qquad 2.14$$

where σ_{wc} and V_w are the resistivity and the volume of the voice coil material respectively. Rewriting Eq. 2.12 yields

$$Q_E = \frac{\sigma_{wc}}{V_w \cdot B^2} (k_s m_s)^{1/2}, \qquad 2.15$$

which is independent of the voice coil wire length.
The resonance frequency of the mass spring system is given by

$$\omega_0 = \left(\frac{k_s}{m_s}\right)^{1/2}. \qquad 2.16$$

Using Eqs. 2.8 and 2.10, regarding Eqs. 2.9 and 2.13 through 2.16, and assuming $Q_{rad} > Q_m$, the following relation for the efficiency is found:

$$\eta(\omega) = \frac{P_a}{P_E} = \frac{1}{Q_{rad} Q_E \left\{\frac{1}{Q_m^2} + \frac{1}{Q_E Q_m} + \left(\frac{\omega}{\omega_0} - \frac{\omega_0}{\omega}\right)^2\right\}}. \qquad 2.17$$

2.2 The sound power response as a function of the frequency

The next quantity of interest is the radiated power $P_a(\omega)$ as a function of frequency. Using Eqs. 2.7 and 2.11 through 2.13, we can rewrite Eq. 2.10 in the form:

$$P_a = \frac{1}{2} \frac{R_{rad}(\omega) \cdot \hat{E}^2}{Q_E^2 (Bl)^2 \left\{\frac{1}{Q_0^2} + \left(\frac{\omega}{\omega_0} - \frac{\omega_0}{\omega}\right)^2\right\}}, \qquad 2.18$$

where Q_0 is the total quality factor defined by

$$\frac{1}{Q_0} = \frac{1}{Q_m} + \frac{1}{Q_E} + \frac{1}{Q_{rad}}. \qquad 2.19$$

The acoustical quality factor is frequency-dependent, but its value is much larger than those of the electrical and mechanical quality factors and we may write:

$$\frac{1}{Q_0} \approx \frac{1}{Q_m} + \frac{1}{Q_E}, \qquad 2.20$$

which is independent of frequency.
For frequencies $\omega < \omega_t$ the radiation resistance R_{rad} is proportional to ω^2 (cf. Eq. 2.2):

$$R_{rad} \propto \omega^2. \qquad 2.21$$

The frequency-dependent part of Eq. 2.18 is given by

$$\left| \frac{\left(\frac{\omega}{\omega_0}\right)^2}{\frac{1}{Q_0^2} + \left(\frac{\omega}{\omega_0} - \frac{\omega_0}{\omega}\right)^2} \right|, \quad \omega < \omega_t, \qquad 2.22$$

and its behavior as a function of frequency with parameter Q_0 is plotted in Fig. 2.4.

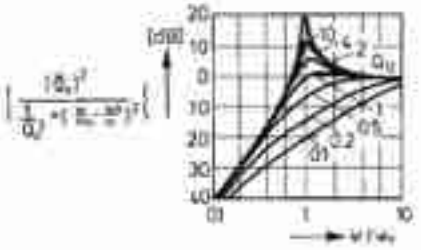

Fig. 2.4. The frequency dependence of the radiated power with parameter Q_0

An actual loudspeaker is designed with $\omega_0 < \omega_t$ and Fig. 2.4 shows that $Q_0 \approx 1$ is an optimum choice if the power response should be flat. This flatness of the power response is due to the compensation of the decreasing diaphragm velocity (inversely proportional to the frequency for $\omega > \omega_0$) by the increasing radiation resistance (direct proportional to the squared frequency for $\omega < \omega_t$). This flat part of the power response is the theoretical operating frequency range of the loudspeaker:

$$\omega_0 < \omega < \omega_t. \qquad 2.23$$

At frequencies below the resonance frequency the diaphragm velocity is asymptotically proportional to the frequency and the radiated power will be proportional to ω^4.
At frequencies above the transition frequency the radiation resistance is constant and the radiated power will be inversely proportional to the squared frequency.
Fig. 2.5 shows the behavior of P_a as a function of frequency with $Q_0 \approx 1$ in accordance with the rigid piston theory

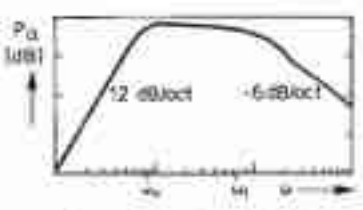

Fig. 2.5. The power P_a as a function of the frequency

The acoustic pressure expressed in dB will show the same frequency dependence as the acoustic power, provided that the directivity remains small.

2.3 The need for a multiway loudspeaker system

A theoretical operating frequency range of the electrodynamic loudspeaker is the constant part of $P_a(\omega)$, i.e. $\omega_0 < \omega < \omega_t$. The lower limiting frequency of the range is determined by the resonant frequency

ω_0 of the mass-spring system of the loudspeaker in its enclosure and the upper limiting frequency is determined by the transition frequency ω_t (cf. Eq. 2.4), which is inversely proportional to the linear dimensions of the loudspeaker.
However, a small lower limiting frequency and a high upper limiting frequency make contrary demands on the size of the loudspeaker.
The maximum radiated power of the loudspeaker equals (see Eqs. 2.2 and 2.9):

$$P_{a_{max}} = \frac{\rho_0 \omega^2 \pi a^4}{c_0} \hat{V}^2_{max} = \frac{\rho_0 \omega^4 \pi a^4}{c_0} \hat{U}^2_{max} \qquad 2.24$$

where $\hat{V}_{max}$ and $\hat{U}_{max}$ are the maximum velocity and excursion capability of the loudspeaker diaphragm, respectively.
Equation 2.24 shows that the radiation of a certain acoustic power requires a larger diaphragm excursion capability, if the lowest frequency to be reproduced is decreased. The excursion capability of an actual loudspeaker is mechanically limited, which makes demands on the minimum diaphragm area. Such a minimum diaphragm area, however, puts a limit on the maximum frequency to be reproduced. Also the loudspeaker will show an increasing directivity if we increase the frequency. Therefore the frequency range of a practical broadband loudspeaker system is divided into two or more frequency parts. Each of these parts is reproduced by a separate loudspeaker. The low frequency loudspeaker or woofer is characterized by a relatively large radiating diaphragm surface and a large excursion capability. The high frequency loudspeaker or tweeter is characterized by a relatively small radiating diaphragm surface and a small excursion capability. For a smooth transition between these two frequency regions an intermediate loudspeaker can be used: the midrange loudspeaker or "squawker".

2.4 Discussion

The lumped parameter model is a useful tool in the design of an electrodynamic loudspeaker. However, it shows some shortcomings:

- The sound radiation above the transition frequency is much larger than that predicted with the lumped parameter model. This is caused by the nonrigidity of the diaphragm at higher frequencies. During movement, the shape of the diaphragm will vary as a function of time (break-up) and the sound radiation will be more complicated than that predicted from this model (Section 4).
- The radiation impedance of a cone- or dome-shaped diaphragm is not equal to that of a plane, rigid piston in an infinite baffle. The sound radiation from such a nonplane diaphragm will show peaks and dips, which cannot be predicted with the simple rigid piston radiation model (section 5).
- The actual loudspeaker shows nonlinearities, while the lumped parameter model contains only linear elements (Section 6).

3. Time-frequency distributions of loudspeakers: the application of the Wigner distribution*

Chapter 3 contains a reprint of the article:
C.P. Janse and A.J.M. Kaizer, Time-Frequency Distributions of Loudspeakers: the Application of the Wigner Distribution,
JAES, vol 31, no. 4, April 1983.

CORNELIS P. JANSE AND ARIE J. M. KAIZER

Philips Research Laboratories, 5600 MD Eindhoven, The Netherlands

The application of the Wigner distribution in the analysis of loudspeakers is discussed. The Wigner distribution of a signal can be interpreted as a distribution of the signal energy in time and frequency. It is a basic time–frequency distribution, and it has properties that allow simple physical interpretations. Furthermore the Wigner distribution facilitates the interpretation of other time–frequency distributions since these distributions can be expressed as a convolution of the Wigner distribution and a weight function determined by the particular distribution considered. The Wigner distribution of the impulse response of a loudspeaker can therefore provide useful information about the transient behavior of the loudspeaker, and it enables a designer to formulate optimization criteria for this behavior.

0 INTRODUCTION

A loudspeaker is a transducer which converts electric energy into acoustic energy. An important quantity of such a transducer is the sound pressure at a point in space as a function of time as a result of the electric voltage applied to the loudspeaker connections. This function is determined both by the impulse response of the loudspeaker as well as by the Fourier transform of this impulse response, the complex-valued transfer function.

The impulse response is defined as the sound pressure at a point in space as a function of time as the result of an electric Dirac pulse [1] applied to the electrical connections of the loudspeaker.

Although the impulse response fully determines the transient behavior of the loudspeaker, this information is not easily visualized by inspection of it, and this hampers the constitution of optimization criteria based on this function. To cope with this problem in the past many transforms or measurements have been developed for evaluation of the response of a loudspeaker. Their purpose is twofold: to give an insight into the physical processes that play a role in a loudspeaker and to determine optimization criteria for the behavior of a loudspeaker. A short review of some functions and measuring methods that have been used in audio engineering follows.

1) *Impulse Response*. The impulse response can be approximated, for a limited bandwidth, by the response of the system to a pulse with a finite width [2], [3]. However, as remarked before, it is difficult to extract relevant information or optimization criteria from the impulse response.

2) *Transfer Function*. The transfer function contains the amplitude and phase characteristics as a function of frequency. The amplitude characteristic in particular has been used in order to optimize the steady-state response of a loudspeaker (flat curve). The amplitude and phase characteristics can be determined by means of a slowly swept sine wave [4], or dynamically by a rapidly swept sine wave or chirp [3], [5]. Also they can be calculated from the Fourier transform of the impulse response.

3) *Group Delay*. The group delay is defined as the negative of the derivative with respect to frequency of the phase characteristic of the transfer function [1]:

$$t_g(\omega) = -\frac{d\phi(\omega)}{d\omega}.$$

The group delay can give an indication of the position of the acoustic center of the transducer.

4) *Tone-Burst Response [4]*. The tone-burst response determines the attack and decay response of a system

* Presented at the 71st Convention of the Audio Engineering Society, Montreux, Switzerland, 1982 March 2–5; revised November 2, 1982.

for a single frequency.

5) *Cumulative Spectra [2].* The cumulative spectra determine the attack and decay responses of the system for a frequency region.

6) *The White-Noise Autocorrelation Function.* This function determines the transient behavior of a filter [6].

In this paper we introduce a new tool in the loudspeaker field: the Wigner distribution. This distribution was proposed by Wigner [7]—as far back as in 1932—for application in quantum mechanics. It was "rediscovered" by Ville [8] and de Bruijn [9] who has given it a sound mathematical foundation, and was recently recognized by Claasen and Mecklenbräuker [10]–[13] as being a powerful tool for time–frequency analysis of signals. Its potential application for audio systems was briefly mentioned by Gerzon in a comment [14].

Because the Wigner distribution of a signal can, with some care, be interpreted as a distribution of the signal energy in time and frequency, it also has an interesting application in the description and interpretation of loudspeaker behavior, where both time and frequency response play such an important role.

We will show that with the Wigner distribution it is possible to interpret the physical processes occurring in practical loudspeakers, and this leads the way to formulate criteria for optimizing the transient behavior of loudspeakers in an elegant way.

The paper is divided into two parts. The first part, Section 1, gives a brief signal-theoretical review of the Wigner distribution and other time–frequency distributions. A very detailed description of the signal-theoretical background of the Wigner distribution can be found in the references [10]–[12]. Here we restrict ourselves to a formulation of the definition and the most important properties, which will allow the reader to understand the material of Section 2 without need to go deeply into the references. Moreover we will give a discussion of the application of the Wigner distribution to study the transient behavior of filters and other linear systems. In Section 2 we will elaborate on the practical application of the Wigner distribution, in particular for loudspeaker systems.

1 THEORETICAL PART

In this part some theoretical properties of general time–frequency distributions are described, while specific attention is paid to the properties of the Wigner distribution.

Section 1.1 gives a general class of time–frequency distributions and a set of possible properties which can be useful when comparing different distributions.

Several known time–frequency distributions are discussed in Section 1.2. The Wigner distribution appears to be a basic time–frequency distribution, in the sense that the other distributions can be described as a convolution of the Wigner distribution and some window function. The specific properties of the Wigner distribution are described in Section 1.3.

Since most practical applications of the Wigner distribution will involve digital processing of sampled data, a numerical evaluation of this time–frequency distribution is required. This comprises the effects of windowing and sampling, which will be discussed in Section 1.4. In this section also a discussion is given of the analytic signal, which will be used frequently when analyzing loudspeakers with the Wigner distribution. In Section 1.5 the relation between this Wigner distribution and two other distributions, often used in the field of audio engineering, namely, the cumulative spectrum and the spectrogram, is discussed.

Some introductory examples of applications are given in Section 1.6, where the Wigner distributions of well-known filter responses are discussed.

This theoretical part is mainly based on the articles by Claasen and Mecklenbräuker [10]–[12]. Part I of their paper [10] discusses the properties of the Wigner distribution for continuous-time signals, and the properties for discrete-time signals are discussed in part II of their paper [11]. Finally, in part III of their paper [12] the relation is given between the Wigner distribution and several other distributions.

1.1. A General Class of Time–Frequency Distributions

In order to extract detailed information on the transient behavior of a system from its impulse response, several different time–frequency distributions have been proposed. For example, the spectrogram and the cumulative spectrum in the audio field. These distributions generally have different properties. An efficient way to compare them systematically is to consider a general class of time–frequency distributions that includes them all.

This general class of time–frequency distributions was introduced by Cohen [15], [16]. Each member of this class is given by

$$C_f(t, \omega; \phi) = \frac{1}{2\pi} \int_{-\infty}^{\infty} \int_{-\infty}^{\infty} \int_{-\infty}^{\infty} e^{j\xi u - \omega\tau - \xi t} \phi(\xi, \tau) \times f\left(u + \frac{\tau}{2}\right) f^*\left(u - \frac{\tau}{2}\right) du\, d\tau\, d\xi \quad (1)$$

where $f(u)$ is the time signal, $f^*(u)$ is its complex conjugate, and ϕ is a so-called kernel function, representative of the particular distribution function.

In order to be able to give a particular distribution an interpretation as a distribution of its energy in time and frequency, the distribution has to possess certain properties. These properties prescribe certain constraints on the kernels. When we determine the kernel of a particular distribution that belongs to the Cohen class, it is possible to study its properties in a systematic way. A suitable set of properties was proposed by Claasen and Mecklenbräuker [12]. These properties and the corresponding constraints on the kernels are listed in Table 1.

The first two properties are very useful, because they

Table 1. Different properties P_i and the corresponding constraints on the kernels. $F(\omega)$ is the Fourier transform of the time signal $f(t)$.

	Properties	Constraint on Kernel
P_1	$\frac{1}{2\pi}\int_{-\infty}^{\infty} C_f(t, \omega; \phi)\, d\omega = \lvert f(t)\rvert^2$	$\phi(\xi, 0) = 1$ for all ξ
P_2	$\int_{-\infty}^{\infty} C_f(t, \omega; \phi)\, dt = \lvert F(\omega)\rvert^2$	$\phi(0, \tau) = 1$ for all τ
P_3	If $g(t) = f(t - t_0)$ then $C_g(t, \omega; \phi) = C_f(t - t_0, \omega; \phi)$	$\phi(\xi, \tau)$ does not depend on t
P_4	If $g(t) = f(t)e^{j\omega_0 t}$ then $C_g(t, \omega; \phi) = C_f(t, \omega - \omega_0; \phi)$	$\phi(\xi, \tau)$ does not depend on ω
P_5	$C_f(t, \omega; \phi) = C_f^*(t, \omega; \phi)$	$\phi(\xi, \tau) = \phi^*(-\xi, -\tau)$
P_6	If $f(t) = 0$ for $\lvert t\rvert > T$ then $C_f(t, \omega; \phi) = 0$ for $\lvert t\rvert > T$	$\int_{-\infty}^{\infty} e^{j\xi t}\phi(\xi, \tau)\, d\xi = 0$ for $\lvert\tau\rvert < 2\lvert t\rvert$
P_7	If $F(\omega) = 0$ for $\lvert\omega\rvert > \Omega$ then $C_f(t, \omega; \phi) = 0$ for $\lvert\omega\rvert > \Omega$	$\int_{-\infty}^{\infty} e^{-j\tau\omega}\phi(\xi, \tau)\, d\tau = 0$ for $\lvert\xi\rvert < 2\lvert\omega\rvert$
P_8	$\frac{\int_{-\infty}^{\infty} t C_f(t, \omega; \phi)\, dt}{\int_{-\infty}^{\infty} C_f(t, \omega; \phi)\, dt} = t_g(\omega)$	$\phi(0, \tau) = 1$ for all τ $\frac{\partial}{\partial\xi}\phi(\xi, \tau)\Big\rvert_{\xi=0} = 0$ for all τ
P_9	$\frac{\int_{-\infty}^{\infty} \omega C_f(t, \omega; \phi)\, d\omega}{\int_{-\infty}^{\infty} C_f(t, \omega; \phi)\, d\omega} = \Omega(t)$	$\phi(\xi, 0) = 1$ for all ξ $\frac{\partial}{\partial\tau}\phi(\xi, \tau)\Big\rvert_{\tau=0} = 0$ for all ξ
P_{10}	$C_f(t, \omega; \phi) \geq 0$ for all t and ω	$\phi(\xi, \tau)$ is the ambiguity function of some function $w(t)$

enable us to consider the distribution as a distribution of energy. The integration of C_f over all frequencies at a fixed time t is the instantaneous power at that time, and the integration of C_f over all times at a fixed frequency is the energy spectral density at that frequency. If either of the properties is satisfied, then the integral over all times and frequencies will equal the total signal energy.

Properties P_3 and P_4 state that shifts in time and frequency give corresponding shifts in the distribution. The next property, P_5, which is very convenient from a practical point of view, is that the distribution is real-valued.

The finite support properties P_6 and P_7 are important. They state that if a signal is bounded in time or frequency, then its distribution will also be bounded in the same time or frequency.

The next two properties can be very useful for signal analysis. Property P_8 has the consequence that the center of gravity or average in the time direction at a fixed frequency of the distribution of the impulse response of a linear time-invariant system is equal to the group delay of the system at that frequency. The definition for the group delay of such a system can be found in the Introduction. The property P_9 states that the center of gravity in the frequency direction at a fixed time of the distribution of a complex-valued signal is equal to the instantaneous frequency.

The last property, P_{10}, is the positivity of the distribution for all times and frequencies. It can be stated that this property is one of the requirements that enable us to interpret the distribution as an energy distribution. However, this property is incompatible with the properties P_6–P_9 [12]. The corresponding constraint has been given in [17] and has the consequence that C_f is a spectrogram with a window function $w(t)$. Therefore the only positive definite distribution functions of the Cohen class are the spectrograms.

If we accept negative values in the distribution, it can be asked whether the distribution still has the physical interpretation of an energy distribution. The occurrence of negative values is consistent with Heisenberg's uncertainty relation which prohibits an arbitrarily sharp frequency discrimination with an arbitrarily sharp time discrimination [12]. Also, we can never assign an exact energy value to a time–frequency point of a distribution. We always have to satisfy Heisenberg's uncertainty relation which requires an averaging over a certain area in the time-frequency plane. In general we prefer the properties P_6–P_9 rather than the positivity property.

Various distributions exist of which the kernel satisfies P_1–P_9 [12], so to choose between these distributions we need an additional criterion. An important criterion is the spread of the square magnitude of $C_f(t, \omega; \phi)$ which is discussed in [18]. The spread of the square

magnitude is taken because large alternating contributions can occur, as can be seen from the various formulas for the distributions of the chirp (see Section 1.2). In that case we can make our choice with the demand of a minimum spread of the square magnitude of $C_f(t, \omega; \phi)$.

1.2 Some Known Time–Frequency Distributions

In Table 2 some known time–frequency distributions with their kernels are listed. With the aid of Table 1 the corresponding properties can be derived. From the set of properties we can judge the usefulness of the particular distribution.

As an example we compare the representation of a chirp, that is, a signal with a linearly increasing frequency:

$$f(t) = e^{j\frac{1}{2}\alpha t^2} \tag{2}$$

where αt is the instantaneous frequency, for the Wigner and Rihaczek distributions.

The Wigner distribution of the chirp is equal to [10]:

$$W_f(t, \omega) = 2\pi\delta(\omega - \alpha t) . \tag{3}$$

This is exactly what we would intuitively expect: a distribution which is concentrated around the line $\omega = \alpha t$.

The representation of the chirp signal obtained by the Rihaczek distribution can be shown to be

$$C_f(t, \omega; \phi) = \sqrt{\frac{2\pi}{\alpha}} \exp\left(j \frac{(\omega - \alpha t)^2}{2\alpha} - j\frac{\pi}{4}\right) \tag{4}$$

while the real part of the Rihaczek distribution gives

$$C_f(t, \omega, \phi) = \sqrt{\frac{2\pi}{\alpha}} \cos\left(\frac{(\omega - \alpha t)^2}{2\alpha} - \frac{\pi}{4}\right) . \tag{5}$$

Although the real part of the Rihaczek distribution has the same set of properties P_1–P_9 as the Wigner distribution, it has a large spread around the line $\omega = \alpha t$. This can be understood if we realize that a distribution may have large alternating contributions and still satisfy P_1–P_9. Therefore we also consider the spread $S(t_0, \omega_0)$ of the square magnitude at a point (t_0, ω_0) of the (t, ω) plane:

$$S^2(t_0, \omega_0) = \int_{-\infty}^{\infty}\int_{-\infty}^{\infty} ((t - t_0)^2 + (\omega - \omega_0)^2) \times |C_f(t, \omega; \phi)|^2 \, dt \, d\omega . \tag{6}$$

In [18] it is shown that this spread of the square magnitude is minimal for the Wigner distribution. This is especially clear when we compare the representation of both distributions for the chirp signal. It can be concluded that the Wigner distribution is the better of the two. From Eq. (1) and Table 2 [or Eq. (9)] it can be found that any member of the Cohen class can be considered as a two-dimensional convolution of the Wigner distribution with a window function:

$$C_f(t, \omega, \phi) = \frac{1}{2\pi}\int_{-\infty}^{\infty}\int_{-\infty}^{\infty} \varphi(t - \tau, \omega - \xi) \times W_f(\tau, \xi) \, d\tau \, d\xi \tag{7}$$

where

$$\varphi(t, \omega) = \frac{1}{2\pi}\int_{-\infty}^{\infty}\int_{-\infty}^{\infty} e^{j(\xi t - \omega\tau)}\phi(\xi, \tau) \, d\xi \, d\tau . \tag{8}$$

This means that any other distribution of the Cohen class can be considered as a spread version of the Wigner distribution. Therefore the Wigner distribution can be considered as the basic distribution of the Cohen class. It is often easier to explain the properties of other distributions in terms of the Wigner distribution than directly from the distribution itself. This will be clear when we discuss the spectrogram and the cumulative spectra in Section 1.5.

The Wigner distribution will be discussed further in Section 1.3.

1.3 The Wigner Distribution

In this section the properties that are important for the application of the Wigner distribution to loudspeakers will be emphasized. For this reason we shall discuss only the auto-Wigner distribution and not the more general cross-Wigner distribution [10].

The Wigner distribution can be evaluated both from the time signal $f(t)$ [10]:

$$W_f(t, \omega) = \int_{-\infty}^{\infty} e^{-j\omega\tau} f\left(t + \frac{\tau}{2}\right) f^*\left(t - \frac{\tau}{2}\right) d\tau \tag{9}$$

and from the Fourier transform $F(\omega)$ of the time signal $f(t)$ [10]:

$$W_F(\omega, t) = \frac{1}{2\pi}\int_{-\infty}^{\infty} e^{-j\Omega t} F\left(\omega + \frac{\Omega}{2}\right) \times F^*\left(\omega - \frac{\Omega}{2}\right) d\Omega . \tag{10}$$

The two distributions have the relation:

$$W_f(t, \omega) = W_F(\omega, t) . \tag{11}$$

The Wigner distribution has the properties P_1–P_9 as discussed in the preceding sections, which makes it possible to interpret it, with some care, as a distribution of the signal energy in time and frequency.

Another remarkable property is that the signal $f(t)$ can be recovered from its Wigner distribution at time $t/2$ by the inverse Fourier transform, up to a constant factor [10]:

$$f(t)f^*(0) = \frac{1}{2\pi}\int_{-\infty}^{\infty} e^{j\omega t} W_f\left(\frac{t}{2}, \omega\right) d\omega . \tag{12}$$

So apart from a constant calibration factor, no information about amplitude or phase is lost in the Wigner distribution. (For complex-valued signals the constant

Table 2. Some known time–frequency distributions with their kernels and corresponding properties.

Name	$C_f(t, \omega; \phi)$	Kernel $\phi(\xi, \tau)$	Properties (Table 1)	References	Remarks
Rihaczek	$f^*(t)F(\omega)e^{j\omega t}$	$e^{j\xi t}$	P_1–P_4, P_6, P_7	[19], [20]	Complex valued
Real part of Rihaczek	$\mathrm{Re}[f^*(t)F(\omega)e^{j\omega t}]$	$\cos\left(\frac{1}{2}\xi\tau\right)$	P_1–P_8	[21]	
Page	$\frac{\partial}{\partial t}\left\|F_t^+(\omega)\right\|^2 = \mathrm{Re}[2f(t)F_t^+(\omega)e^{j\omega t}]$	$e^{-j\xi(\tau+\|\tau\|)/2}$	P_1–P_6	[22]	$F_t^+(\omega)$ is the running spectrum $F_t^+(\omega) = \int_{-\infty}^{t} f(\tau)e^{-j\omega\tau}\,d\tau$
Levin	$-\frac{\partial}{\partial t}\left\|F_t^+(\omega)\right\|^2 = \mathrm{Re}[2f(t)F_t^+(\omega)e^{j\omega t}]$	$e^{-j\xi(\tau-\|\tau\|)/2}$	P_1–P_6	[21]	$F_t^+(\omega)$ is the running spectrum $F_t^+(\omega) = \int_{t}^{\infty} f(\tau)e^{-j\omega\tau}\,d\tau$
Spectrogram	$\|F_t(\omega)\|^2$	$\frac{1}{2\pi}\int_{-\infty}^{\infty}\int_{-\infty}^{\infty} W_w(-t, u)e^{j(\omega u-\xi t)}\,du\,dt$	P_1–P_5, P_{10}	[12], [23]	$W_w(-t, \omega)$ is the Wigner distribution of the window function $w(t)$ $F_t(\omega) = \int_{-\infty}^{\infty} e^{-j\omega\tau}f(\tau)w(\tau - t)\,d\tau$
Cumulative decay spectrum	$\|F_t^+(\omega)\|^2$	$\left(\pi\delta(-\xi) - \frac{1}{j\xi}\right)e^{-j\xi(\tau+\|\tau\|)/2}$	P_2–P_5, P_{10}	[2]	For $F_t^+(\omega)$ see Levin
Cumulative attack spectrum	$\|F_t^-(\omega)\|^2$	$\left(\pi\delta(\xi) + \frac{1}{j\xi}\right)e^{-j\xi(\tau-\|\tau\|)/2}$	P_2–P_5, P_{10}	[2]	For $F_t^-(\omega)$ see Page
Wigner	$\int_{-\infty}^{\infty} e^{-j\omega\tau}f\left(t + \frac{\tau}{2}\right)f^*\left(t - \frac{\tau}{2}\right)d\tau$	1	P_1–P_6	[9]–[13]	

will be complex.)

Before discussing the numerical evaluation of Wigner distributions it is convenient to review the Wigner distribution of a combination of two signals.

The Wigner distribution of the sum of two signals f and g is given by:

$$W_{f+g}(t, \omega) = W_f(t, \omega) + W_g(t, \omega) + 2\,\mathrm{Re}\{W_{f,g}(t, \omega)\} \quad (13)$$

where Re means real part of and $W_{f,g}$ is the cross-Wigner distribution defined by [10]:

$$W_{f,g}(t, \omega) = \int_{-\infty}^{\infty} e^{-j\omega\tau} f\left(t + \frac{\tau}{2}\right) g^*\left(t - \frac{\tau}{2}\right) d\tau \quad (14)$$

The Wigner distribution of a convolution of two signals f and g is given by [10]:

$$W_{f*g}(t, \omega) = \int_{-\infty}^{\infty} W_f(\tau, \omega) W_g(t - \tau, \omega)\, d\tau \quad (15)$$

and is equal to the convolution of the Wigner distributions W_f and W_g in the time variable.

The Wigner distribution of the product of two signals f and g is given by [10]:

$$W_{f \cdot g}(t, \omega) = \frac{1}{2\pi} \int_{-\infty}^{\infty} W_f(t, \Omega) W_g(t, \omega - \Omega)\, d\Omega \quad (16)$$

and is equal to the convolution of the Wigner distributions W_f and W_g in the frequency variable.

As the last subject in this section we will discuss the occurrence of negative values in the Wigner distribution. It has been shown in [24] that the Wigner distribution of a function $f(t)$ can only be nonnegative for the whole (t, ω) plane if the function is a Dirac pulse or a Gabor function (for a reference to Gabor functions see [9, p. 261]), that is, a function of the form:

$$f(t) = e^{\alpha t^2 + \beta t + \gamma}, \qquad \mathrm{Re}\{\alpha\} < 0 \quad (17)$$

where α, β, and γ can be complex-valued.

In Section 1.1 it was explained that the occurrence of negative values in the distribution is consistent with Heisenberg's uncertainty relation which prohibits an arbitrarily sharp frequency discrimination with an arbitrarily sharp time discrimination [12]. Moreover, for the Wigner distribution it can be shown that suitable averages of the distribution, in accordance with Heisenberg's uncertainty relation, always yield positive values [25].

The question arises whether it is such an advantage that the Wigner distribution gives a much sharper picture than the other distributions, as shown in Section 1.2. In our opinion the answer is affirmative because we have to realize that the other distributions always perform a fixed weighting, which depends on the particular transformation.

The Wigner distribution allows one to choose any weighting function afterward. For example, it is even possible to weight with a function whose dimension in the frequency direction is frequency-dependent and whose dimension in the time direction is in conformity with the uncertainty relation. This specific weighting procedure is of importance, for example, when a logarithmic frequency scale is used.

1.4 Computational Aspects of the Numerical Evaluation of the Wigner Distribution: Windowing, Discrete-Time Signal, and Analytic Signal

The practical calculation of the Wigner distribution from a measured impulse response cannot be performed directly:

1) Due to the infinite integration boundaries the Wigner distribution can only be evaluated analytically. To be able to estimate the integral numerically, the signal has to be weighted with a time-limited function, a so-called window function $w(t)$ with the property that $w(t)$ vanishes for $|t| > T$.

2) In the preceding sections we only considered the Wigner distribution for continuous-time signals. To perform a practical measurement, where a digital computer is used, we have to evaluate the Wigner distribution from a discrete-time signal.

Therefore we have to window and to sample the continuous-time signal, the effects of which will be discussed in this section. Also we will discuss the analytic signal, because this signal will be frequently used for the application of the Wigner distribution to loudspeakers.

1.4.1 Windowing

The windowed version of a continuous-time signal $f(t)$ is given by:

$$f_t(\tau) = f(\tau) w(\tau - t) \quad (18)$$

where t gives the position of the window on the time axis.

With Eq. (15) we can evaluate the Wigner distribution of the windowed signal:

$$W_{f_t}(\tau, \omega) = \frac{1}{2\pi} \int_{-\infty}^{\infty} W_f(\tau, \Omega) \times W_w(\tau - t, \omega - \Omega)\, d\Omega \quad (19)$$

For each window position we get another Wigner distribution. Now consider only the cross sections where $\tau = t$. In this case the window is symmetrically located around τ, and we obtain:

$$W_{f_t}(\tau, \omega)|_{\tau=t} = \frac{1}{2\pi} \int_{-\infty}^{\infty} W_f(t, \Omega) \times W_w(0, \omega - \Omega)\, d\Omega \quad (20)$$

The new function of t and ω is the so-called pseudo-Wigner distribution proposed by Claasen and Meck-

lenbräuker [10], [12]:

$$\mathrm{PWD}(t, \omega) = W_h(\tau, \omega)|_{\tau=t} \quad (21)$$

This pseudo-Wigner distribution closely resembles the original Wigner distribution when it is evaluated with a properly chosen window function. Compared with the Wigner distribution, the pseudo-Wigner distribution lacks the properties P_2, P_7, and P_8. From Eq. (19) we see that such a distribution is a spread version (leakage) in the frequency direction of the Wigner distribution. This spreading is equal to a convolution in the frequency direction of the Wigner distribution of the nonwindowed signal with the Wigner distribution of the window function. Therefore it will be clear that we do not have the finite support property P_2 in the frequency direction. It can be shown [12] that windowing by means of w amounts to smoothing the Wigner distribution in the frequency direction. An important point is that the pseudo-Wigner distribution does not give a spread in the time direction as, for example, the spectrogram does, which will be discussed in Section 1.5.

When considering the influence of a window on the impulse response $h(t)$ of a causal system with $h(t) \approx 0$ for $t > t_1$, we see that the pseudo-Wigner distribution, evaluated with a window length $T > t_1$, will closely resemble the Wigner distribution. In that case the pseudo-Wigner distribution almost has the properties P_2, P_7, and P_8, and this will improve further, without decreasing the time resolution, when we lengthen the window. The impulse response of a loudspeaker always satisfies the condition ($h(t) \approx 0$ for $t > t_1$ where the window length $T > t_1$) on its impulse response and therefore we will refer to the Wigner distribution in Section 2, although we actually mean a pseudo-Wigner distribution.

1.4.2 Discrete-Time Signals

The transition from a Wigner distribution of a continuous-time signal to that of a discrete-time signal is not trivial, and several definitions for the Wigner distribution for discrete-time signals are possible [11], [26], [27]. We will use the definition given in [11]. In [10] it is shown that for a band-limited signal [$F(\omega) = 0$ for $|\omega| > \omega_c$] the distribution is completely determined by the samples:

$$W_f(nT, \omega) = 2T \sum_{k=-\infty}^{\infty} e^{-j2\omega kT} f[(n + k)T] f^*[(n - k)T] \quad (22)$$

where the sample time T satisfies $T \leq \pi/2\omega_c$, that is, $f_s \geq 4f_c$, where f_s is the sample frequency: $f_s = 1/T$. Eq. (22) is the basis for the Wigner distribution of discrete-time signals. When $T = 1$ we obtain the Wigner distribution for a discrete-time signal $f(n)$ with a unit sample period [11]:

$$W_f(n, \theta) = 2 \sum_{k=-\infty}^{\infty} e^{-j2\theta k} f(n + k) f^*(n - k) \quad (23)$$

For the case of a time-limited signal it can be shown that $W_f(n, \theta)$ is completely determined by its samples in the frequency domain [11]. When the window w of the pseudo-Wigner distribution has a length $M \geq 2L - 1$, $w(k) = 0$ for $|k| \geq L$, then the pseudo-Wigner distribution is completely determined by its samples:

$$\mathrm{PWD}\left(n, m \frac{\pi}{M}\right) = 2 \sum_{k=-L+1}^{L-1} e^{-j\pi m 2k/M} p(k) g(n, k), \quad m = 0, \cdots, M - 1 \quad (24)$$

where

$$p(k) = w(k) w^*(-k)$$

and

$$g(n, k) = f(n + k) f^*(n - k).$$

To evaluate the pseudo-Wigner distribution for a time n we can interpret Eq. (24) for $M = 2L - 1$ as a discrete Fourier transform (DFT) with respect to the variable k of the function $p(k)g(n, k)$, which can be calculated efficiently using a fast Fourier transform (FFT) procedure. However, such an FFT requires an even number of points. This can be solved easily by adding a zero to the series, so that $M = 2L$.

The window p can be a known window like a Hamming or a Kaiser window [28], or a rectangular window for a short impulse response.

A detail is the fact that an FFT is mostly evaluated with the boundaries 0 and $M - 1$. This is no problem if we realize that:

$$e^{-j\pi m 2k/M} = e^{-j\pi(m+M)2k/M} \quad (25)$$

If we rearrange the terms $p(k)g(n, k)$ in Eq. (24) with respect to the k variable from $-M/2 + 1, \ldots, 0, \ldots, M/2$ into $0, \ldots, M/2, -M/2 + 1, \ldots, -1$, we can perform the FFT, which results in a frequency sequence from 0 to $M - 1$ (Fig. 1).

A more important point is the aliasing behavior of the Wigner distribution. The periodicity in the frequency variable of the Wigner distribution is π, whereas that of the Fourier transform is 2π. This difference is caused by the factor 2 in the exponent of Eq. (23). The restriction $f_s \geq 4f_c$ in Eq. (22) indicates that we have to use a sampling frequency which is twice as high as that used for a Fourier transform.

For an analytic signal we can use the usual sampling frequency according to the Nyquist criterion, because the frequency spectrum of the analytic signal vanishes for negative frequencies. It can be shown [11] that the Wigner distribution has no aliasing contributions for any signal whose spectrum is nonzero on an interval smaller than or equal to π (Figs. 2 and 3).

In Section 1.3 it was stated that the Wigner distribution can be evaluated both from the time signal $f(t)$ and from its Fourier transform $F(\omega)$. Without going into details, we note that the requirements for evaluating a distribution from $F(\omega)$ are similar to those described above for the evaluation from the time signal $f(t)$. First

we have to start with a time-limited signal $f(t)$, where $f(t) = 0$ for $|t| > t_0$. If $t_0 \leq 4/d_t$, then the frequency behavior of the distribution is completely defined by samples at distance d_t in the frequency domain.

After this a band-limited signal is assumed, and it can be shown that the time behavior of the distribution is completely defined by samples in the time domain, which are of the form $W_f(m\pi/M, n)$. If the requirement $t_0 \leq 4/d_t$ cannot be fulfilled, aliasing contributions in the time direction will result. However, this requirement is practically always fulfilled when considering an impulse response of a filter or a loudspeaker.

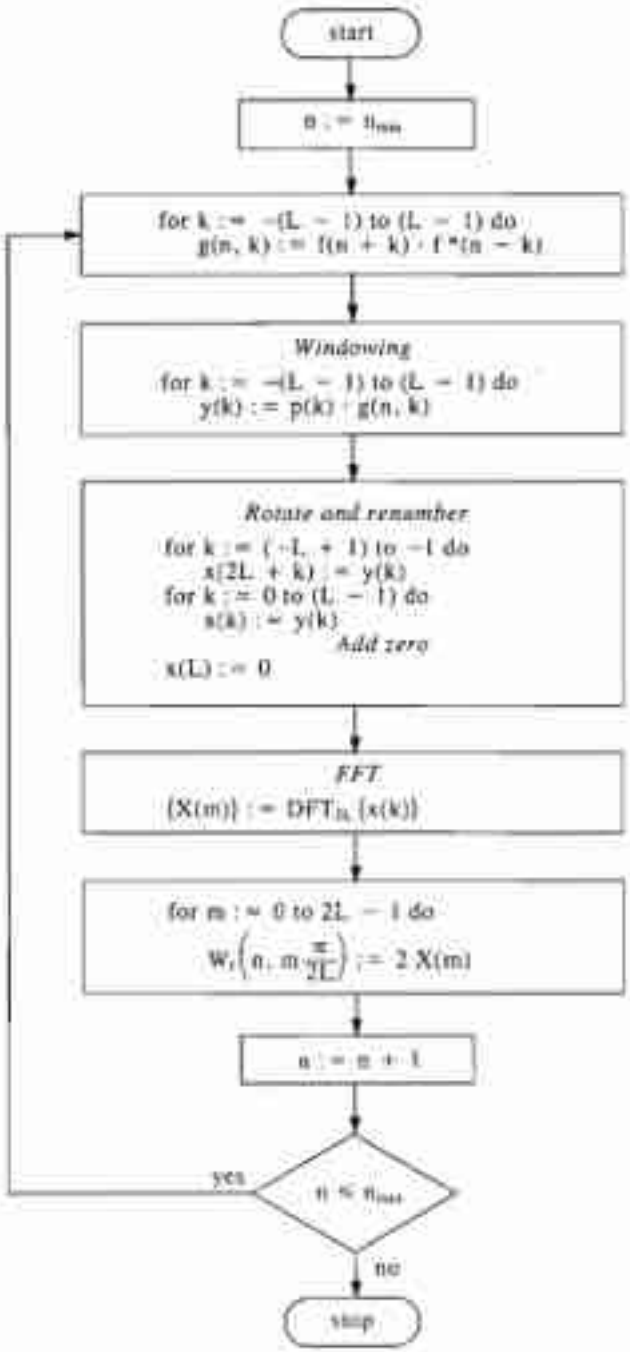

Fig. 1. Flow diagram of the calculation of the Wigner distribution.

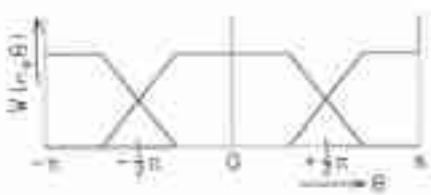

Fig. 2. Wigner distribution aliasing of a real-valued time signal.

The evaluation of the Wigner distribution in the frequency domain is sometimes more convenient for an analytically known system, in particular when its representation in the frequency domain is simpler than that in the time domain. This is the case, for example, with filter systems.

A practical measurement usually starts more conveniently from the time domain impulse response. Then the analytic signal is determined in the frequency domain. Again we have to be aware of aliasing in the time direction.

1.4.3 Analytic Signal

In Section 1.4.1 it was shown that the pseudo-Wigner distribution gives a spread in the frequency direction. A spread in the time direction is obtained by using the analytic signal associated with a real-valued $f(t)$. This is a complex-valued time signal $f_a(t)$ in which the real part equals $f(t)$ and the imaginary part is the Hilbert transform of $f(t)$. The relation between the spectrum $F(\omega)$ of the original signal $f(t)$ and the spectrum $F_a(\omega)$ is given by:

$$F_a(\omega) = \begin{cases} 2F(\omega), & \omega > 0 \\ F(\omega), & \omega = 0 \\ 0, & \omega < 0 \end{cases} . \qquad (26)$$

In [10] it is shown that the relation between the Wigner distributions of $f(t)$ and $f_a(t)$ is given by:

$$W_{f_a}(t, \omega) = \begin{cases} \frac{4}{\pi} \int_{-\infty}^{\infty} W_f(t - \tau, \omega) \frac{\sin(2\omega\tau)}{\tau} d\tau, & \omega > 0 \\ 0, & \omega < 0 \end{cases} \qquad (27)$$

This relation can be interpreted as follows [10]. The Wigner distribution of the analytic signal at a fixed positive frequency can be obtained by filtering the cross section at frequency ω, which is in fact a function of time, with an ideal low-pass filter with cut-off frequency 2ω.

To give an example we consider the Wigner distributions of the sine wave $f(t) = \cos(\omega_0 t)$ and the associated analytic signal $f_a(t) = e^{j\omega_0 t}$. The Wigner distributions are

$$W_f(t, \omega) = \frac{\pi}{2}[\delta(\omega - \omega_0) + \delta(\omega + \omega_0) + 2\delta(\omega)\cos(2\omega_0 t)]$$

$$W_{f_a}(t, \omega) = 2\pi\delta(\omega - \omega_0) . \qquad (28)$$

In the first case we obtain a stationary contribution

at $\omega = \pm\omega_0$ and a varying contribution at $\omega = 0$, which is caused by the variations of the instantaneous power. In the second case we only obtain a contribution at $\omega = \omega_0$.

The varying contribution in the first part can be interpreted as the interference between the positive and negative frequencies. This is a more general property of the Wigner distribution. When the Wigner distribution has two contributions in the (t, ω) plane, then there will be an alternating contribution due to interference in between. This will occur for two contributions in any direction of the (t, ω) plane [18].

By evaluating the Wigner distribution from the analytic signal rather than the signal itself, we avoid the interference between positive and negative frequencies. This is important for the application of the Wigner distribution to loudspeakers, since the contributions due to interferences give no additional information and are disturbing when formulating optimization criteria. This is the reason why we frequently use the analytic signal in the application of the Wigner distribution to loudspeakers. However, we have to realize that the finite support property in the time direction no longer holds because of the spreading-out effects in the time direction according to Eq. (27).

1.5 Relations between Wigner Distribution, Spectrogram, and Cumulative Spectra

The spectrogram is used in the field of speech analysis [12], [23], while the cumulative spectra are used in the designing of loudspeakers [2]. They can be considered as members of the Cohen class, as was shown in Table 2. The spectrogram can be calculated from the short-time Fourier transform (SFT). The SFT is the Fourier transform of the original signal $f(t)$ windowed with a window function $w(t)$:

$$F_t(\omega) = \int_{-\infty}^{\infty} e^{-j\omega\tau} f(\tau) w(\tau - t)\, d\tau \qquad (29)$$

where t indicates the position of the window on the time axis.

The spectrogram S_t is obtained by:

$$S_t(t, \omega) = |F_t(\omega)|^2 \qquad (30)$$

and the relation to the Wigner distribution is given by [12]:

$$S_t(t, \omega) = \frac{1}{2\pi}\int_{-\infty}^{\infty}\int_{-\infty}^{\infty} W_f(\tau, \Omega) \times W_w(\tau - t, \omega - \Omega)\, d\tau\, d\Omega \qquad (31)$$

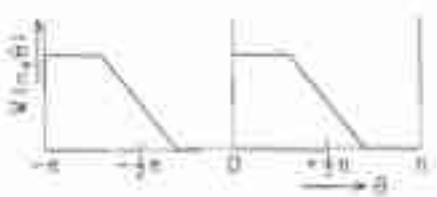

Fig. 3. As Fig. 2, but with an analytic signal (without aliasing)

From Table 2 it follows that the spectrogram has the properties P_5, P_6, P_7, and P_{10}, that is, the shift properties and the positivity of the distribution. It can also be shown [12] that the relations which give the group delay and the instantaneous frequency for the Wigner distribution now give an average group delay and an average instantaneous frequency over the length of the window. This means that the spectrogram can provide useful information for signals that are almost stationary over the window length. Since the impulse response of a loudspeaker is not stationary at all during the window length, it is generally better to use the pseudo-Wigner distribution instead of a spectrogram in the field of loudspeaker design (see also Section 1.4.1).

Comparing the pseudo-Wigner distribution with the spectrogram we see that the first distribution does not have the positivity property, but it has the properties P_1 and P_8. From Eqs. (19) and (31) it is clear that the spectrogram does not have the finite support property in the time direction while the pseudo-Wigner distribution does have this property. Both the pseudo-Wigner distribution and the spectrogram are spreaded versions of the Wigner distribution, but with the pseudo-Wigner distribution the spreading is only in the frequency direction. When the frequency resolution is increased (by increasing the window length), the time resolution decreases in the spectrogram. This is not the case for the pseudo-Wigner distribution, where we are free to increase the frequency resolution without affecting the time resolution.

The cumulative spectra [2] can be divided into a decay and an attack spectrum. These are in fact special cases of the spectrogram, and the points in the cumulative spectrum have values which are equal to an integral over a cross section of the Wigner distributions of the windowed signals. The difference is the fact that the window is a step function $U(t)$:

$$U(t) = \begin{cases} 1, & T \geq 0 \\ 0, & t < 0 \end{cases} \qquad (32)$$

The kernels and properties of the cumulative spectra can be found from Table 2, and it is clear that the derivative of the decay spectrum (with respect to the variable t which indicates the position of the window on the time axis) is equal to the distribution of Levin, while the derivative of the attack spectrum is equal to the distribution of Page. The set of properties of these distributions is limited.

When evaluating the cumulative spectra numerically it is not possible to extend the integration boundary to infinity. Therefore the impulse response is not weighted with a step function but with a finite window. In that case the spectrogram, the cumulative decay, and the cumulative attack spectra only differ in the time definition. In Eq. (31) the relation between the spectrogram and the Wigner distribution is given, where the time t indicates the center of the window. With the cumulative spectra the time definition is shifted over half the window length. The relation between the Wigner distri-

bution and the cumulative decay spectrum is:

$$S_d(t, \omega) = |F_t^+(\omega)|^2$$

$$= \frac{1}{2\pi}\int_{-\infty}^{\infty}\int_{-\infty}^{\infty} W_t(\tau, \Omega) W_w\left(\tau - t + \tfrac{1}{2}T, \omega - \Omega\right) d\tau\, d\Omega \qquad (33)$$

where T indicates the window length. For the attack spectrum this relation is:

$$S_a(t, \omega) = |F_t^-(\omega)|^2$$

$$= \frac{1}{2\pi}\int_{-\infty}^{\infty}\int_{-\infty}^{\infty} W_t(\tau, \Omega) W_w\left(\tau - t - \tfrac{1}{2}T, \omega - \Omega\right) d\tau\, d\Omega \,. \qquad (34)$$

In a practical case the length of a window used with a spectrogram is relatively short, while the window length for a cumulative spectrum is relatively long.

Since the cumulative spectrum is used frequently for the evaluation of loudspeakers, we will discuss another aspect of the cumulative spectrum. In [2] it is shown that the cumulative spectrum can be interpreted as the square magnitude of the system response to a starting or a stopping sine wave. If we have an input signal of a linear time-invariant system of the form $e^{j\omega t}U(t)$, where $U(t)$ is the step function, then the response of the system is given by:

$$g_\omega(t) = \int_{-\infty}^{\infty} e^{j\omega(t-\tau)} U(t - \tau) g(\tau)\, d\tau$$

$$= e^{j\omega t}\int_{-\infty}^{\infty} e^{-j\omega\tau} U(t - \tau) g(\tau)\, d\tau \qquad (35)$$

where $g(t)$ is the impulse response of the system.

From Table 2 and Eq. (35) it is clear that:

$$|F_t^-(\omega)|^2 = |g_\omega(t)|^2 \,. \qquad (36)$$

Thus at any frequency ω_0, the attack spectrum is the square magnitude of the response of a starting sinusoidal oscillation with frequency ω_0. However, we have to realize that when the sinusoidal oscillation starts, this is associated with a transient phenomenon which has appreciable contributions at frequencies other than ω_0. The Wigner distribution of the input signal is given by:

$$W_t(t, \omega) = \begin{cases} \dfrac{2}{\omega - \omega_0}\sin[2(\omega - \omega_0)t], & t \geq 0 \\ 0, & t < 0 \,. \end{cases} \qquad (37)$$

For small values of t, W_t has a large spread in the frequency direction. This means that for small t the cumulative spectrum will have appreciable contributions located in the stopband of the system.

A similar discussion can be given for the decay spectrum. We note that these spreads are in conformity with those of the distributions of Page and Levin, which are not band-limited either. The above aspects will be clearly visible when we evaluate the cumulative spectrum of a band-pass filter (Section 1.6) or a loudspeaker (Section 2.3).

From the above discussion it will be clear that we prefer the Wigner distribution over the cumulative spectrum in the field of loudspeaker engineering.

1.6 The Wigner Distributions of Some Filters

In this section, which is in fact an introduction to the application of the Wigner distribution to loudspeakers (Section 2), Wigner distributions of some filters will be discussed. All calculated distributions are pseudo-Wigner distributions, but we will nevertheless call them Wigner distributions in this section, since the Wigner distribution and the pseudo-Wigner distribution are almost indistinguishable for the signals used (see Section 1.4).

In Fig. 4 the Wigner distribution of the impulse response of a Butterworth low-pass filter of order 3 is shown. The cut-off frequency (−3 dB) is 1 kHz. Fig. 5 gives the corresponding contour plot. The group delay, the frequency characteristic, that is, the magnitude of the transfer function, and the impulse response of this filter are shown in Figs. 6–8.

It can be seen that the Wigner distribution has a mountain ridge parallel to the frequency axis and, at

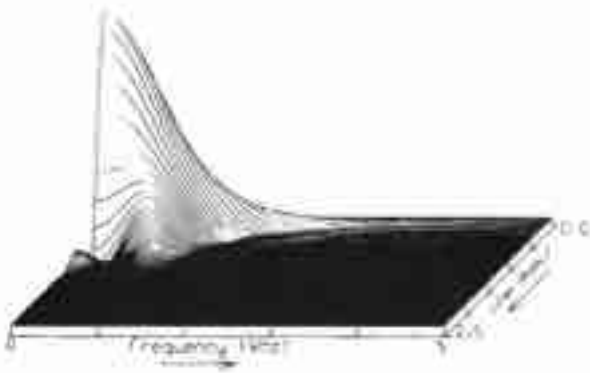

Fig. 4. Wigner distribution of a low-pass Butterworth filter.

Fig. 5. Contour plot of Fig. 4.

the cut-off frequency, a ridge parallel to the time axis. This latter ridge will be called "ear" in the remaining part of the paper. The distribution is only given for positive frequencies since it is symmetric with respect to the time axis for real-valued signals. The mountain ridge is delayed with respect to the time of excitation, and this delay is in conformity with the Bode relations [38]. Bode showed that this delay is inversely proportional to the cut-off frequency and proportional to the slope of the filter. The latter is clearly visible in Figs. 9 and 10, where the Wigner distribution is shown of a corresponding filter of order 6 with the same cut-off frequency.

We observe also that the length of the ear increases, which agrees with the fact that the group delay of the filter at the cut-off frequency increases when the steepness of the filter slope increases. The group delay, the freqeency characteristic, and the impulse response of this filter are shown in Figs. 11–13.

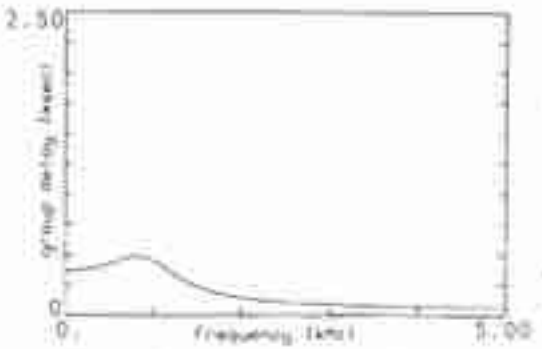

Fig. 6. Group delay of filter of Fig. 4.

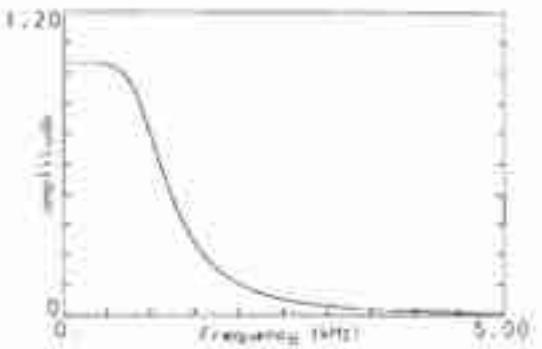

Fig. 7. Magnitude of the transfer function of filter of Fig. 4.

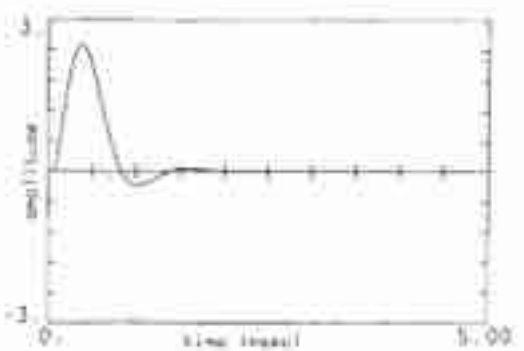

Fig. 8. Impulse response of filter of Fig. 4.

The alternating contributions in Figs. 4 and 9 are interferences between the ears at positive and negative frequencies, as discussed in Section 1.4.3.

From the previous discussion it is clear that we have to take care when determining the delay of, for example,

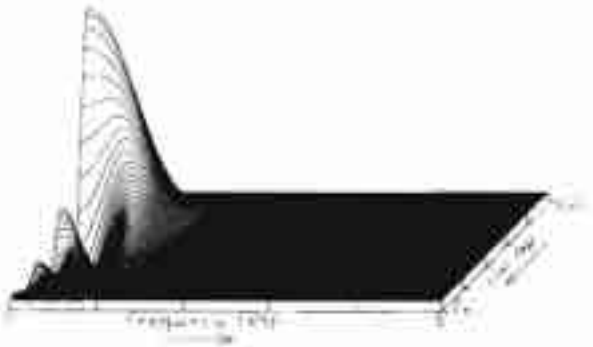

Fig. 9. Wigner distribution of filter of Fig. 4 with a steeper slope.

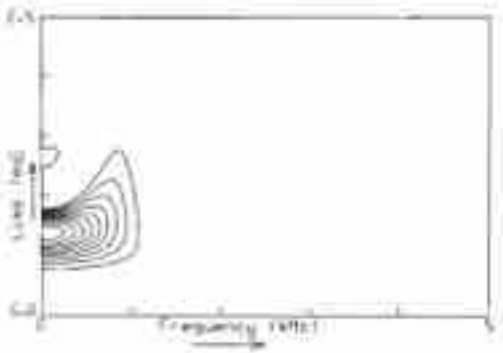

Fig. 10. Contour plot of Fig. 9.

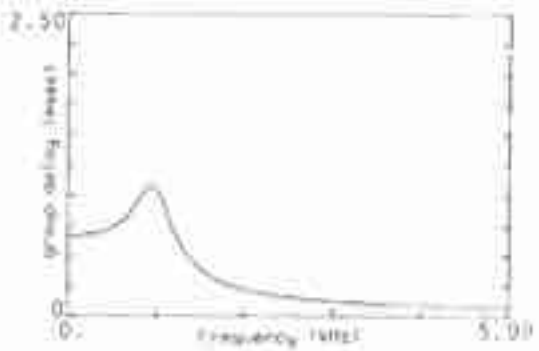

Fig. 11. Group delay of filter of Fig. 9.

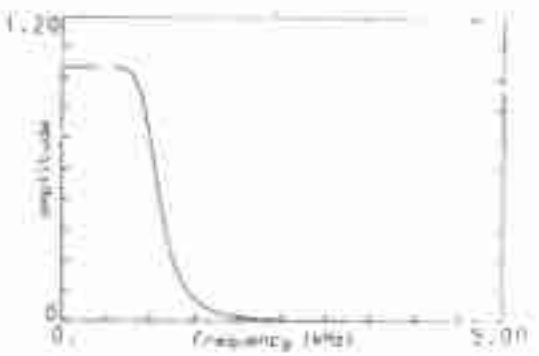

Fig. 12. Magnitude of the transfer function of filter of Fig. 9.

a woofer or tweeter loudspeaker with different anti-aliasing filters. These antialiasing filters introduce an additional delay, which can disturb a proper interpretation of the delays.

In Figs. 14–17 the Wigner distribution, the group delay, the frequency characteristic, and the impulse response for a Butterworth band-pass filter are shown. This band-pass filter is a series combination of a low-pass filter of order 10 with a cut-off frequency of 4000 Hz and a high-pass filter of order 2 with a cut-off frequency of 1000 Hz. The ear at the high frequency cut-off is comparable with that of the low-pass filter shown in Fig. 4. However, the large number of interferences make it difficult to interpret the distribution.

Figs. 18 and 19 show the Wigner distribution of the analytic signal of the same band-pass filter ($F_a(f) = 0$ for $f < 0$).

It is clear that the interferences between positive and negative frequencies, which impede an interpretation of the distribution, have disappeared.

The length of the ears is proportional to the filter shape on a linear frequency scale. For audio purposes filters are generally used which have a certain decay per octave. For filters with the same decay per octave the length of the ears will increase with decreasing cut-off frequency.

The magnitude of the analytic signal can be interpreted as the envelope of the original signal [29], and it can be shown [1] that the envelope of the response of a symmetric band-pass filter equals the impulse response of a low-pass filter with a cut-off frequency equal to the bandwidth of the band-pass filter. The distribution in Figs. 18 and 19 indeed resembles the distribution of a low-pass filter shifted in the frequency direction. The distributions are not exactly the same because we did not use a symmetric band-pass filter.

In Section 1.4.3 it was shown that for each ω the

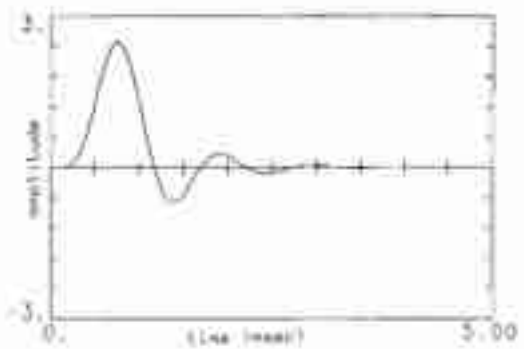

Fig. 13. Impulse response of filter of Fig. 9.

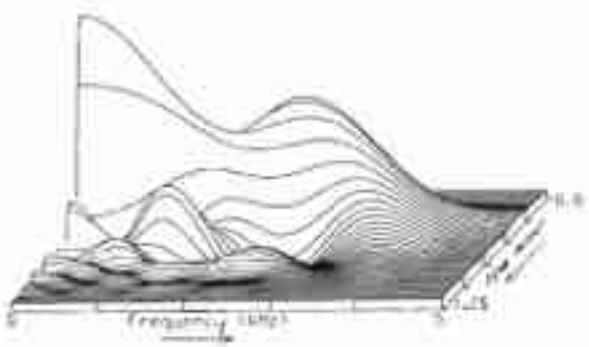

Fig. 14. Wigner distribution of a Butterworth band-pass filter.

Fig. 15. Group delay of filter of Fig. 14.

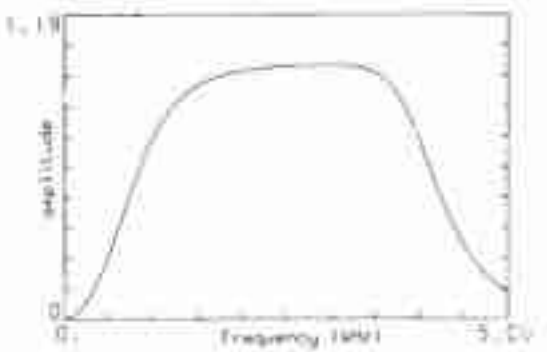

Fig. 16. Magnitude of the transfer function of filter of Fig. 14.

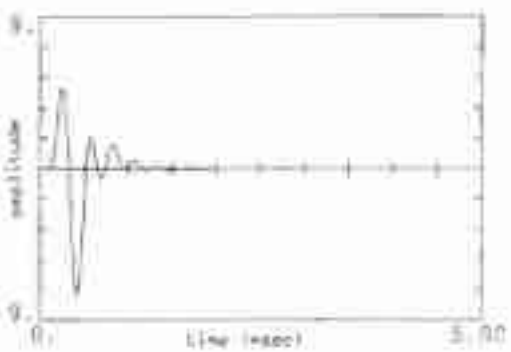

Fig. 17. Impulse response of filter of Fig. 14.

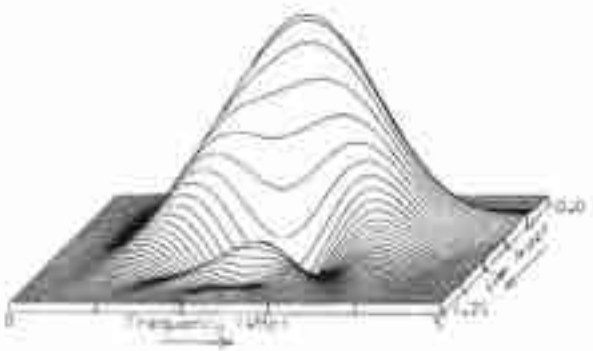

Fig. 18. Wigner distribution of filter of Fig. 14 evaluated with the analytic signal.

Wigner distribution of the analytic signal is related to the Wigner distribution of the original signal by a convolution in the frequency variable of the Wigner distribution with an ideal low-pass filter with cut-off frequency 2ω. This means that we get spreading-out effects, especially at low frequencies. This becomes very clear in the contour plot of the Wigner distribution of the analytic signal of a low-pass filter (Fig. 20). Even at times $t < 0$ the distribution gives nonzero contributions, which are such that the group delay is constant in the passband of the filter. (Contributions for $t < 0$ can occur since the Hilbert transform used to determine the imaginary part of the signal is a noncausal transform.)

The filter used in Figs. 18 and 19 is a minimum-phase band-pass filter. It is important to note that a linear-phase filter, which has a constant group delay, also has ears in the time direction, as can be seen in Figs. 21 and 22. The group delay, the frequency characteristic, and the impulse response of this filter are shown in Figs. 23–25.

The next example in this section is the combination of two Butterworth band-pass filters with a slope of order $n = 3$ in the crossover frequency region as described by Linkwitz [30]. This combination has a passband from 500 to 4000 Hz, with a crossover at 2500 Hz. The low-frequency band-pass filter is a series combination of a band-pass filter of order $n = 2$ at 500 Hz and a high-frequency rolloff of order $n = 10$ at 4000 Hz followed by a third-order Butterworth 2500-Hz low-pass filter. The high-frequency band-pass filter

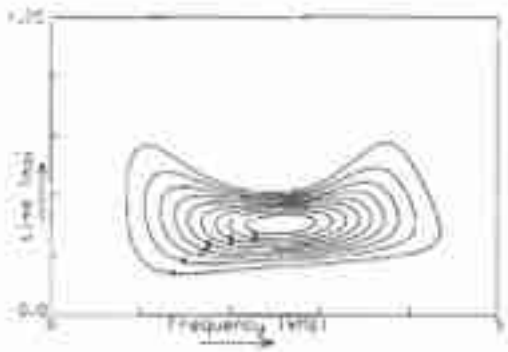

Fig. 19. Contour plot of Fig. 18.

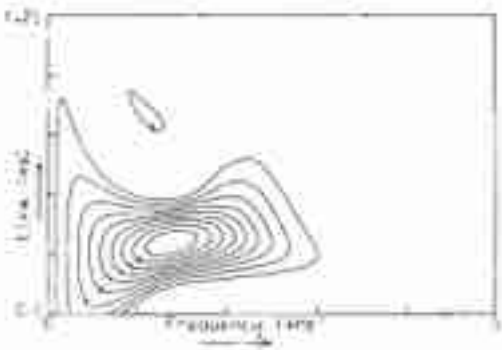

Fig. 20. Contour plot of Wigner distribution of a low-pass filter of order $n = 6$ evaluated with the analytic signal. Cut-off frequency 2500 Hz.

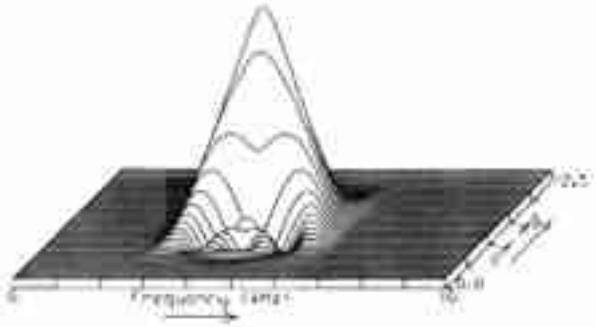

Fig. 21. Wigner distribution of a linear-phase finite impulse response (F.I.R.) filter with a length of 51 samples.

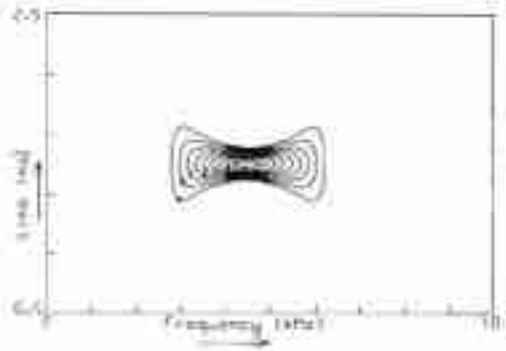

Fig. 22. Contour plot of Fig. 21.

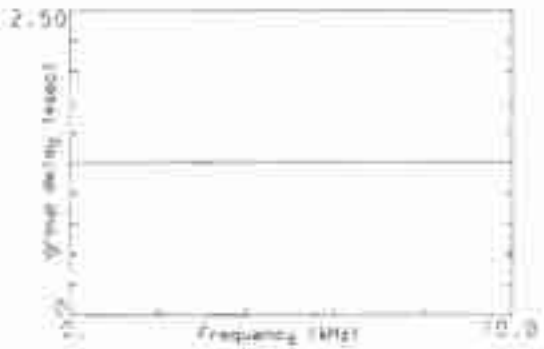

Fig. 23. Group delay of filter of Fig. 21.

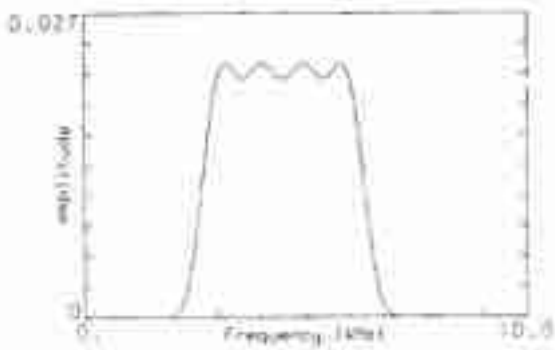

Fig. 24. Magnitude of the transfer function of filter of Fig. 21.

is a similar combination of the same 500–4000-Hz band-pass and a third-order Butterworth 2500-Hz high-pass filter. If we connect one of the two filters in antiphase, then the group delay is smaller in the passband than if we connect both filters in phase, as shown by Linkwitz [30]. The differences are not very large. However, the impulse responses are quite different, but these differences cannot be interpreted easily. What happens can be seen more clearly in the Wigner distribution of the two combinations, because now we can study the attack of the response in more detail. Connecting the two filters in phase gives an additional delay of the distribution around the crossover frequency (Figs. 26–34).

The group delay is often misused. In [1] it was shown that the group delay has a proper interpretation as the delay of a narrow-band modulated signal. The Wigner distribution indicates when the group delay provides useful information for a broadband system. For the band-pass this is the case at the mountain ridge, and it is questionable at the ears because the group delay does not give information on the spreading-out effects. An example is the linear-phase filter with a constant group delay in the passband. The constant group delay tells us nothing about the concentration of the energy around this time. It is clear that in the regions of the roll-off frequencies the energy is more spread (in the

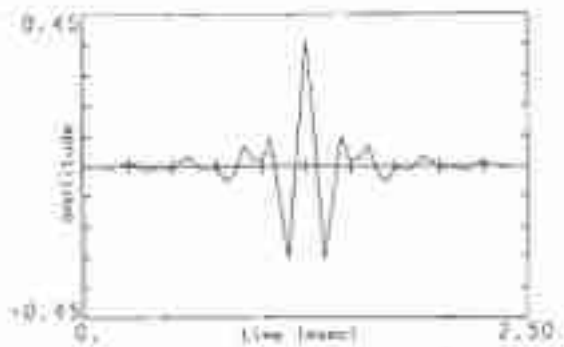

Fig. 25. Impulse response of filter of Fig. 21.

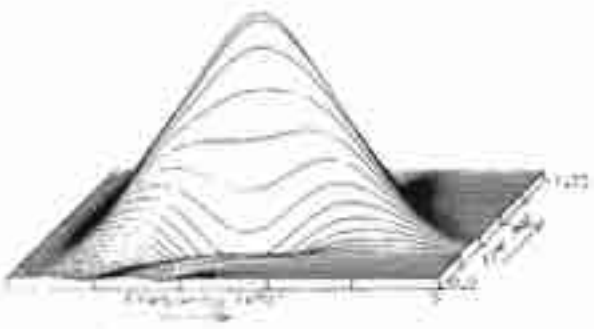

Fig. 26. Wigner distribution of a third-order crossover. The two band-pass filters are connected in phase.

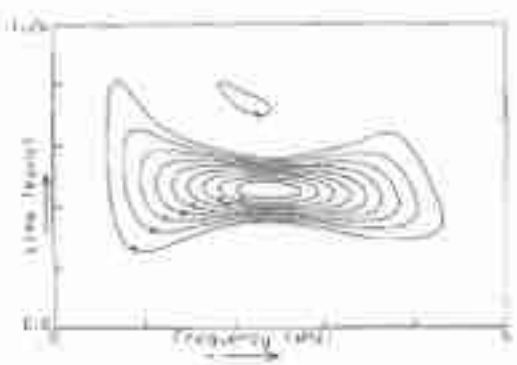

Fig. 27. Contour plot of Fig. 26.

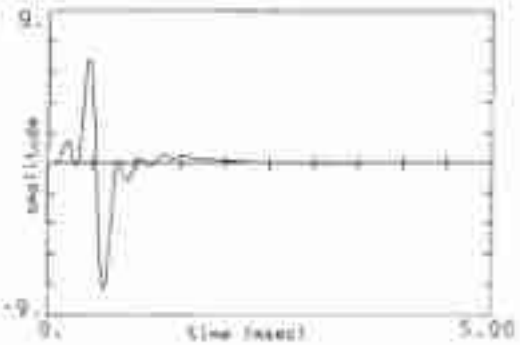

Fig. 28. Impulse response of filter of Fig. 26.

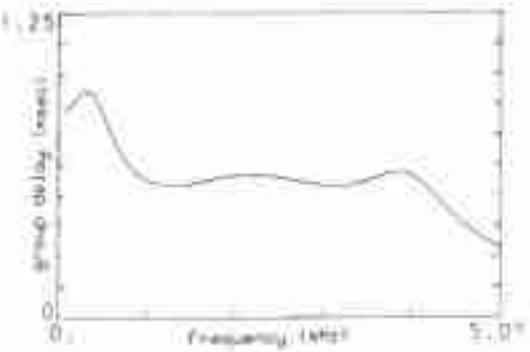

Fig. 29. Group delay of filter of Fig. 26.

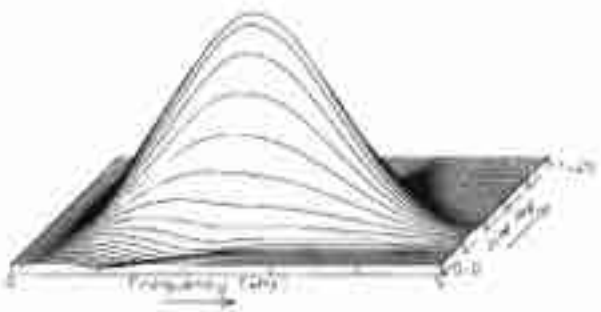

Fig. 30. Wigner distribution of the third-order crossover of Fig. 26 where the band-pass filters are connected in antiphase.

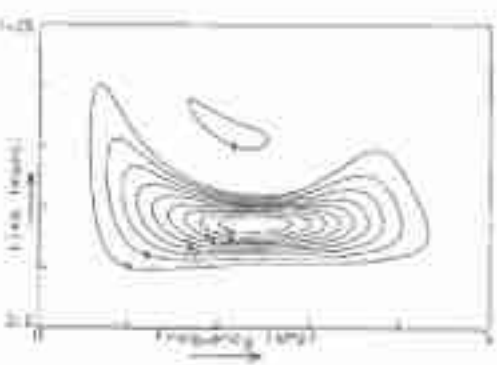

Fig. 31. Contour plot of Fig. 30.

time direction) than in the passband region. The group delay has a constant value only because the energy is spread symmetrically around the delay time. The interpretation of group delay as a delay of the signal energy is certainly wrong in the stopband, because there even causal systems can possess a negative group delay [10], [31]–[33].

Another example of the group delay providing wrong information is the case where we have two spaced time responses, for example, a reflection. The center of gravity in the time direction of the Wigner distribution, which equals (Table 1) the group delay of the total signal, lies between the two ridges when the size of the ridges is of the same order. Thus the value of the group delay gives no information about the delay of the separate contributions.

In our opinion, the Wigner distribution gives more and better information about the time delays of a system than the group delay.

To conclude we give a comparison of several time–frequency plots of other distributions of the impulse response of one and the same Butterworth 500–4000-Hz band-pass filter with a low-frequency rolloff of order 3 and a high-frequency rolloff of order 10 (Figs. 35–37). The corresponding Wigner distribution is given in Fig. 43.

We note the fact that the cumulative decay spectrum also has appreciable contributions in the stopband, which agrees with the discussion in Section 1.5.

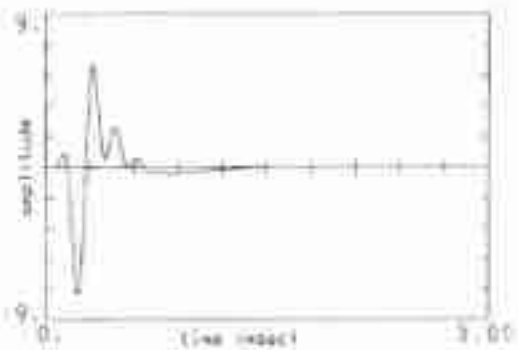

Fig. 32. Impulse response of filter of Fig. 30.

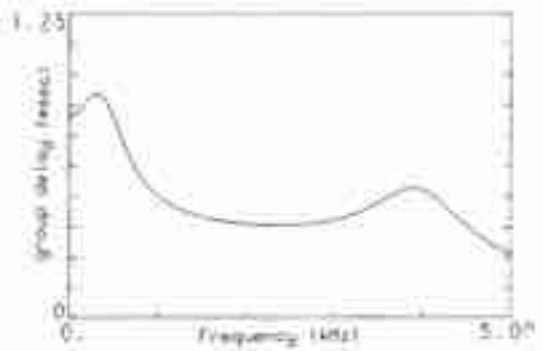

Fig. 33. Group delay of filter of Fig. 30.

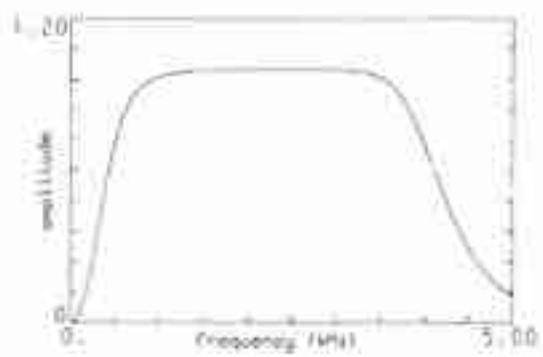

Fig. 34. Magnitude of transfer function of filters of Figs. 26 and 30.

2 APPLICATION OF THE WIGNER DISTRIBUTION TO LOUDSPEAKERS

In Section 1 some fundamental issues of the Wigner distribution were discussed. It was shown that this distribution can be interpreted, with some care, as a distribution of the signal energy in time and frequency. The Wigner distribution can be considered as a basic time–frequency distribution. Since the Wigner distribution compared with other distributions is optimum, it can more easily be interpreted than other distributions. Also, the properties of other distributions can be studied conveniently using the Wigner distribution. The negative values that occur in the Wigner distribution were shown to be in accordance with Heisenberg's uncertainty relation. Averages of the Wigner distribution, taken with a weighting function whose dimensions are in accordance with Heisenberg's uncertainty relation, al-

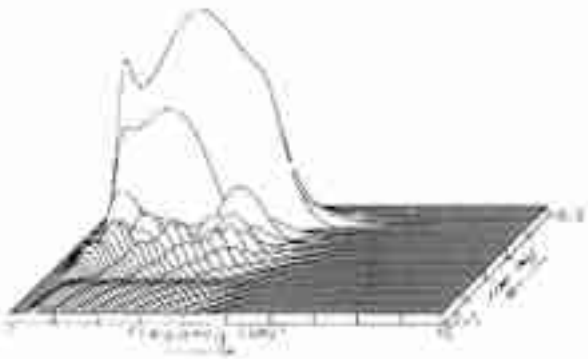

Fig. 35. Real part of Rihaczek distribution of a Butterworth band-pass filter.

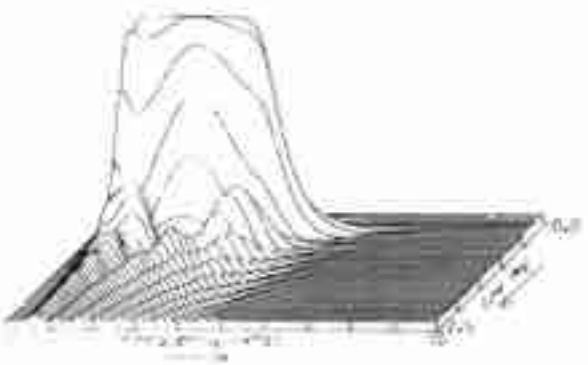

Fig. 36. Real part of Rihaczek distribution of a Butterworth band-pass filter evaluated with the analytic signal.

ways yield a positive value [25]. It was shown that a transform that has positive values at all time and frequency points in its distribution lacks some very important properties.

In order to evaluate the Wigner distribution numerically it was necessary to introduce the pseudo-Wigner distribution [10], [12]. Because this distribution uses a weighted version of the impulse response, it is possible to restrict the integration to an interval with finite boundaries.

The pseudo-Wignor distribution was found to be a frequency-spread version of the Wigner distribution. However, the pseudo-Wigner distribution closely resembles the Wigner distribution when the system under study has a rapidly decaying impulse response and when a suitable (sufficiently long) window is used. This is nearly always the case for the impulse responses of practical filters or loudspeakers. For that reason, we need not bother to refer to the Wigner distribution in this part of the paper, when we actually mean the pseudo-Wigner distribution.

In this section we discuss the application of the Wigner distribution to loudspeakers. It will be shown that the Wigner distribution enables us to formulate optimization criteria for the time–frequency (transient) response of a transducer or a combination of transducers.

In Section 2.1 the application of the Wigner distribution to the evaluation of a single transducer is discussed, and in Section 2.2 a similar discussion about combinations of transducers is given. In Section 2.2 we will also devote some attention to the role of the geometrical mounting of the single transducers in the loudspeaker box and to the influence of the crossover on the time–frequency behavior of a single transducer and a combination of transducers.

In Section 2.3 we discuss some points concerning the practical use of the Wigner distribution and in Section 2.4 we compare the Wigner distribution and the cumulative spectra that are commonly used in the field of loudspeaker engineering. Finally Section 2.5 contains a concluding discussion of the results obtained, and of perspectives for future research.

2.1 Application of the Wigner Distribution to the Evaluation of a Single Transducer

A definition of an ideal transducer could be: A transducer is an ideal transdocer if its impulse response is a Dirac pulse. This means that its frequency characteristic has a constant value for all frequencies and the acoustic response will be a (delayed) copy of the electric signal.

However, this definition is not very realistic, since a transducer with an infinitely extended frequency characteristic or with a response at direct current cannot be physically realized. Therefore, a more practical definition is the following: An "ideal" transducer is one of which the time–frequency behavior resembles that of a smooth band-pass filter.

The type of filter that we take for the prototype is somewhat arbitrary, but the smoothness condition hints toward Butterworth or Bessel filters. (The Wigner distributions of these two types of filters are similar for low-order filters.) The location of the rolloffs of the filter and their shapes can be defined in detail, and the filter has a flat response in the passband.

The comparison with such an "ideal" band-pass filter gives us a manageable criterion for the time–frequency behavior of a transducer and allows an easy visual inspection.

In view of the preference for the Wigner distribution discussed in Section 1, this means that—in the ideal situation—the Wigner distributions of this filter and transducer should be very similar.

The Wigner distribution of the impulse response of a Butterworth band-pass filter is shown in Fig. 38. This filter has a low-frequency cutoff at 500 Hz with a slope of order 2 and a high-frequency cutoff at 4000 Hz with a slope of order 10. Figs. 39–42 give the contour plot of Fig. 38 and the group delay, the frequency characteristic, and the impulse response of the same filter.

The Wigner distribution was evaluated for the analytic signal (see Section 1.4). The time–frequency picture of the band-pass filter contains a mountain ridge parallel to the frequency axis and two ears (ridges) parallel to the time axis located at the cut-off frequencies. This means that the signal energy located around the transition bands of the filter is spread in the time direction. The alternating (positive and negative) contributions are the interferences between the ears as discussed in Section 1.4.3. The integration over all times at a fixed

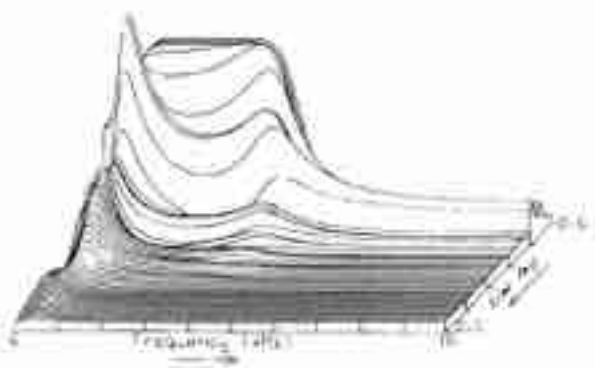

Fig. 37. Cumulative decay spectrum of a Butterworth band-pass filter.

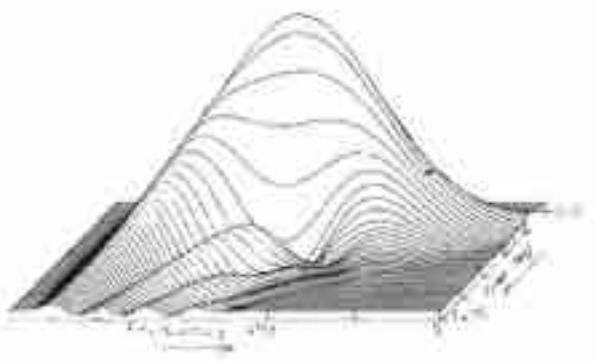

Fig. 38. Wigner distribution of an "ideal" band-pass filter evaluated with the analytic signal.

frequency is equal to the energy spectral density $|F(\omega)|^2$. The center of gravity in the time direction is the group delay $t_g(\omega)$ (Table 1). The plots of the Wigner distribution show that the group delay at the transition bands is larger than in the pass-band, which is a well-known fact. The length of the ears increases if the steepness of the roll-off slopes increases, as can be seen in Fig. 43, which is a filter with the same cut-off frequencies as that of Fig. 38, but with a low-frequency slope of order 3. The group delay, the frequency characteristic, and the impulse response of the same filter are shown in Figs. 44–46.

The length of the ears is proportional to the steepness of the filter slope on a linear frequency scale. The filters that are used in the field of audio engineering have a steepness defined as a number of decibels per octave, that is, on a logarithmic frequency scale. The length of the ears decreases as the corresponding roll-off frequency of a filter increases.

For the comparison of the time-frequency behavior of a transducer with that of an "ideal" band-pass filter

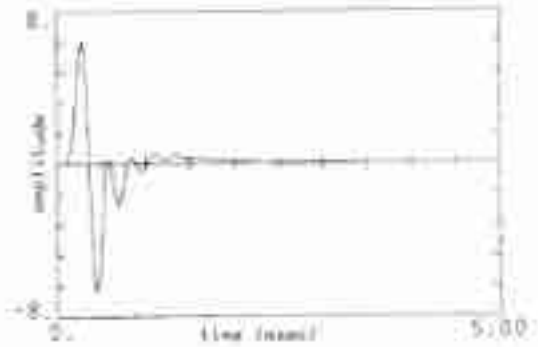

Fig. 42. Impulse response of filter of Fig. 38.

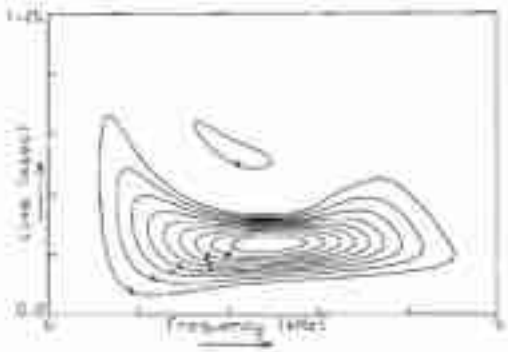

Fig. 39. Contour plot of Fig. 38.

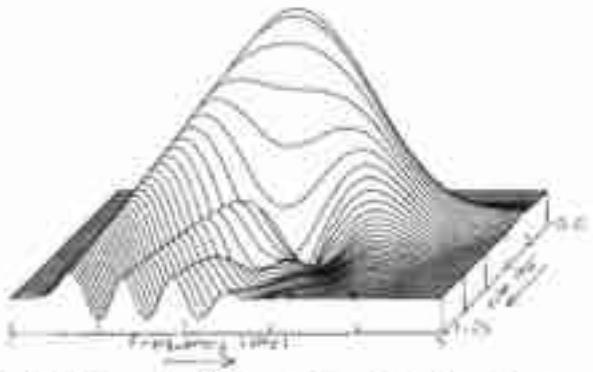

Fig. 43. Wigner distribution of filter of Fig. 38 with a steeper slope.

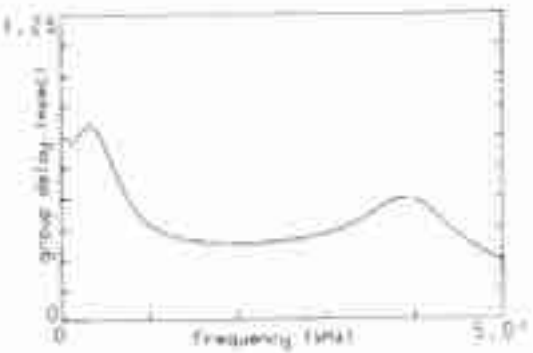

Fig. 40. Group delay of filter of Fig. 38.

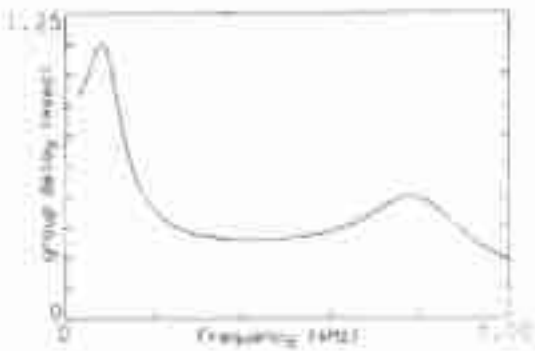

Fig. 44. Group delay of filter of Fig. 43.

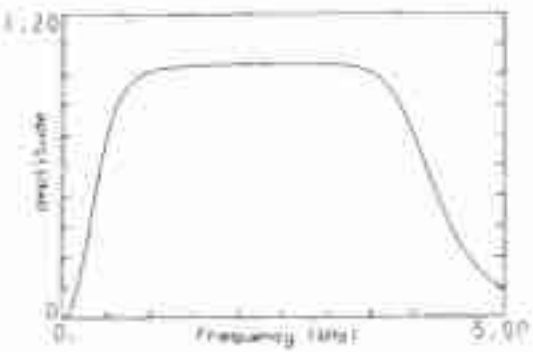

Fig. 41. Magnitude of the transfer function of filter of Fig. 38.

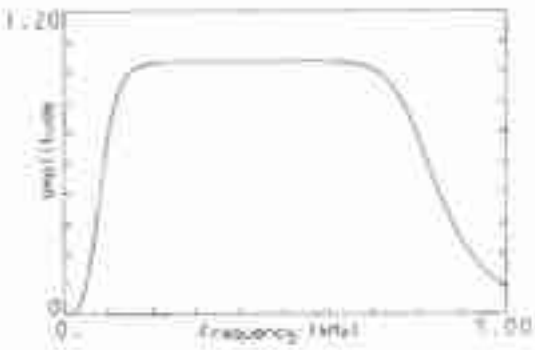

Fig. 45. Magnitude of the transfer function of filter of Fig. 43.

it is helpful to distinguish some typical deviations from the ideal time–frequency behavior observed in actual transducers:

1) The occurrence of additional ears that are not located at the cut-off frequencies.

2) The mountain ridge not being parallel to the frequency axis, which means that the acoustic center of the transducer shifts with frequency.

3) The occurrence of reflections in the time direction, for instance, reflections inside the cabinet or diffraction effects at the edges of the transducer or the cabinet.

Let us consider some practical examples of these typical deviations and, for comparison, an example of an almost ideal time–frequency behavior of a tweeter loudspeaker.

1) *Additional Ears.* Fig. 47 shows the Wigner distribution of a woofer cone loudspeaker. The additional ears are clearly visible. These ears are the ringing contributions, in the time direction, of the bending resonances in the break-up region of the loudspeaker. These are typical of cone loudspeakers [34].

Figs. 48 and 50 give the Wigner distributions of two almost identical woofer loudspeakers. The woofers are made of a different cone material with a different material damping. The log magnitude of their transfer functions are shown in Figs. 49 and 51.

The influence of the damping on the bending resonances is clear. Although the differences of the resonance in the two loudspeakers also manifest themselves in a different transfer function, we maintain that the

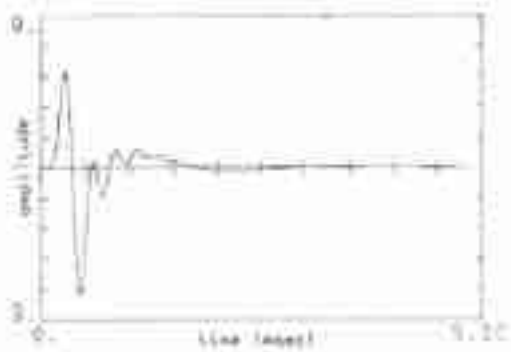

Fig. 46. Impulse response of filter of Fig. 43.

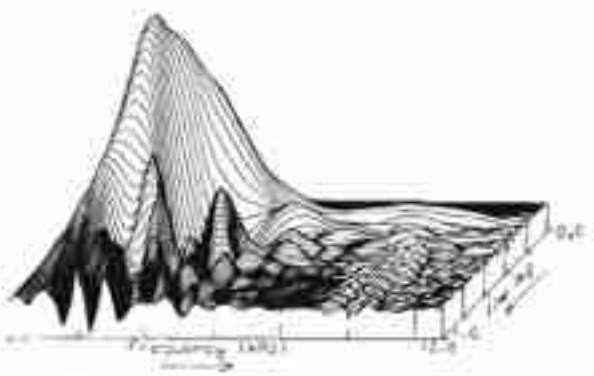

Fig. 47. Wigner distribution of a woofer cone loudspeaker evaluated with the analytic signal.

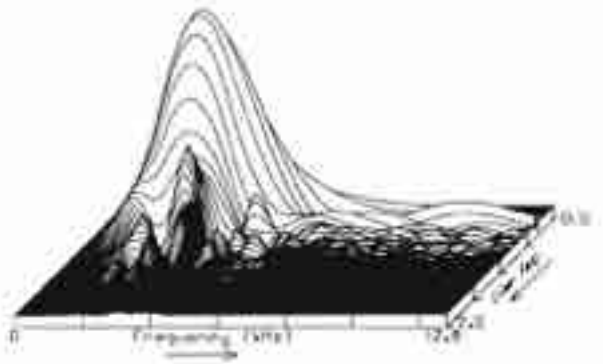

Fig. 48. Wigner distribution of a woofer cone loudspeaker.

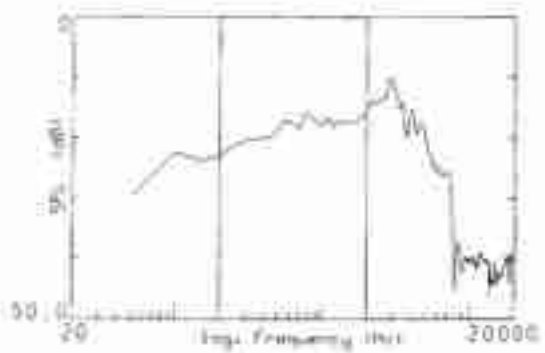

Fig. 49. Log. magnitude of the transfer function of the woofer of Fig. 48.

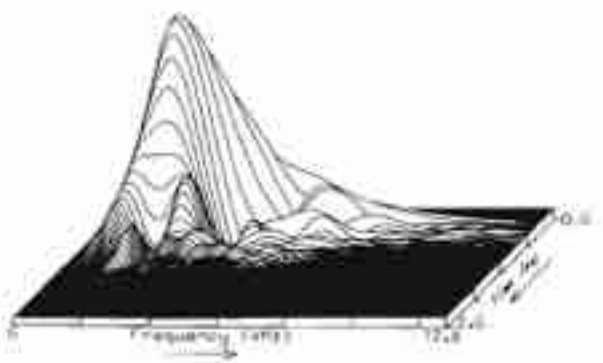

Fig. 50. Wigner distribution of a woofer cone loudspeaker. The damping coefficient of the cone material is higher than that of the cone material of the woofer shown in Fig. 48.

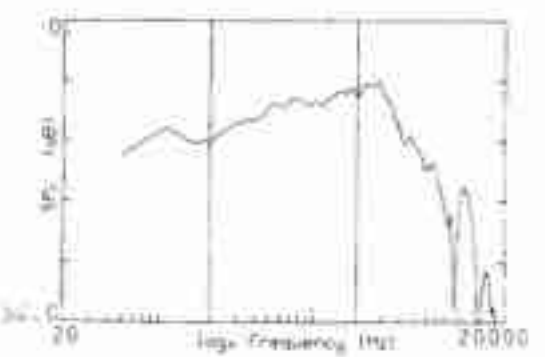

Fig. 51. Log. magnitude of the transfer function of the woofer of Fig. 50.

effect is much more clearly visible in the Wigner distribution. The woofer with the higher material damping has a ringing contribution (ears) that decays more rapidly, as can be expected.

A further example of the occurrence of additional ears is the time–frequency behavior of a dome tweeter. Its Wigner distribution is shown in Fig. 52. The ear at high frequencies is not a normal roll-off ear; its size is too large at these frequencies. It is caused by the ringing of the first membrane resonance of the dome [34] and is typical of dome loudspeakers. Dome tweeters with a soft dome material (rubber-impregnated textile material) have a more rapidly decaying ear at this frequency than dome tweeters with a hard (polymer) dome material. The larger material damping of the soft dome is the reason for the faster decay.

2) *Frequency-Dependent Acoustic Center.* Fig. 53, showing the contour plot of the Wigner distribution of a squawker loudspeaker, is an example of a frequency-dependent acoustic center. The acoustic center of this transducer shifts at the high-frequency end of its passband. This means that the crossover frequency between squawker and tweeter has to be shifted to lower frequencies in order to get an optimum combination. This has indeed been done in the practical applications of this squawker, presumably as a result of listening tests. However, this effect restricts our freedom in the design of a loudspeaker combination.

3) *Reflections in the Time Direction.* The next example is a tweeter loudspeaker which is incorrectly mounted in a baffle. The front side of the tweeter protrudes from the baffle, which causes a (diffraction) reflection from the edge. This reflection can be seen in the contour plot of Fig. 54.

4) *Loudspeaker with an Almost Ideal Time–Frequency Behavior.* The last example in this section is the Wigner distribution of the impulse response of a newly developed tweeter loudspeaker, which is shown in Fig. 55. Fig. 56 gives the contour plot of this Wigner distribution, and the group delay, the frequency characteristic, and impulse response of this tweeter are shown in Figs. 57–59. The time–frequency behavior is almost equal to that of an "ideal" band-pass filter, which can be found in Fig. 38. The result of this nearly ideal situation is considerable freedom in choosing the crossover frequency and the filter. It also may be concluded that further development of this tweeter can hardly improve its transient behavior.

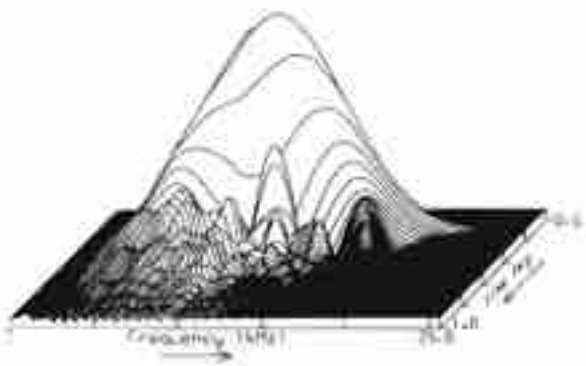

Fig. 52. Wigner distribution of a dome tweeter calculated with the analytic signal.

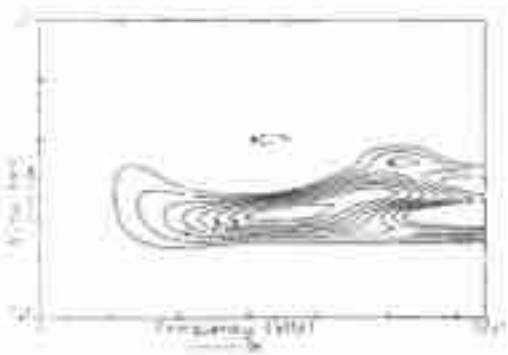

Fig. 53. Contour plot of the Wigner distribution of a squawker loudspeaker with a frequency-dependent acoustic center.

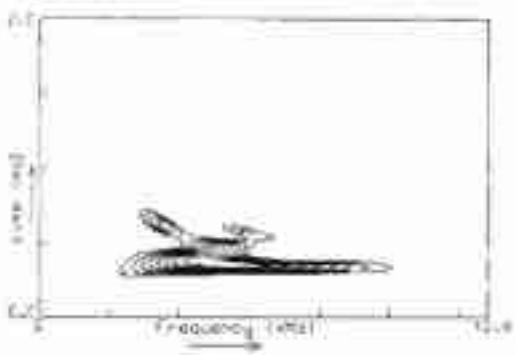

Fig. 54. Contour plot of the Wigner distribution of a tweeter loudspeaker with an improper (protruded) mounting.

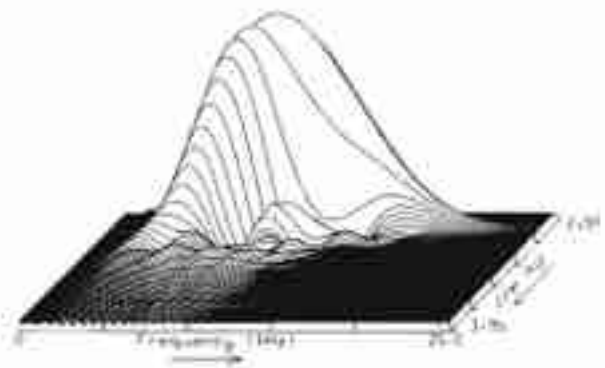

Fig. 55. Wigner distribution of a newly developed tweeter loudspeaker.

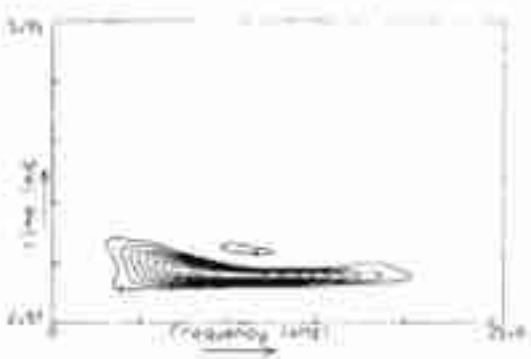

Fig. 56. Contour plot of Fig. 55.

From these examples it can be concluded that the Wigner distribution is a powerful tool for the evaluation and optimization of the time–frequency behavior of a single transducer. The Wigner distribution enables us therefore to formulate optimization criteria for the transient behavior of the transducer. Deviations from this ideal behavior, caused, for example, by diaphragm resonances or by unwanted reflections, can easily be identified and examined. Furthermore, the Wigner distribution gives important information on the position, as a function of frequency, of the acoustic center of the transducer.

2.2 Application of the Wigner Distribution to the Evaluation of a Combination of Transducers

The combination of different transducers in one system introduces two new problem areas where the Wigner distribution can be of help: the geometrical separation

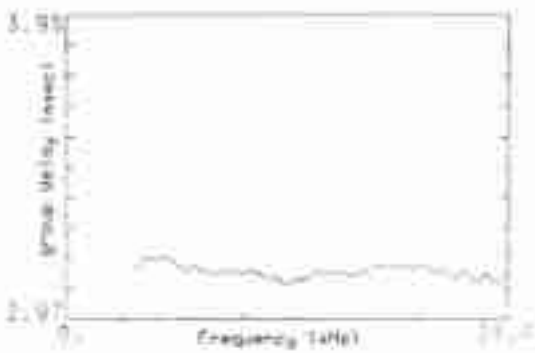

Fig. 57. Group delay of tweeter of Fig. 55.

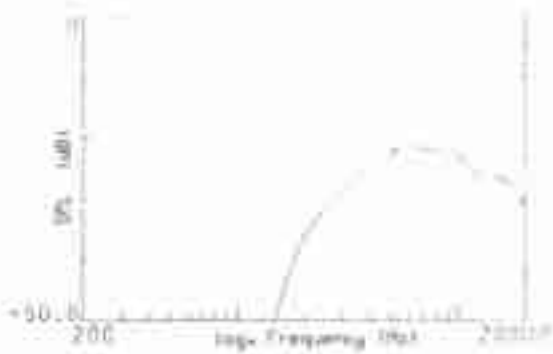

Fig. 58. Log. magnitude of the transfer function of tweeter of Fig. 55.

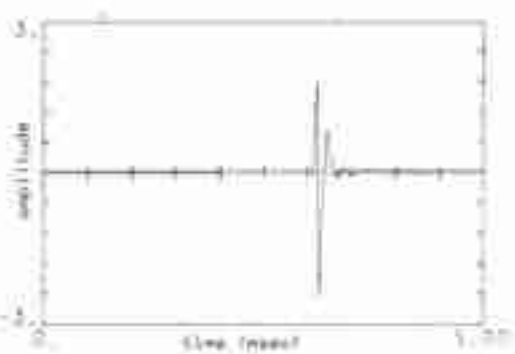

Fig. 59. Impulse response of tweeter of Fig. 55.

of the transducers and the excitation of the transducers via an electric crossover network. Starting from a single ideal transducer it is clear that the optimization criterion for a combination of transducers is a time–frequency behavior (Wigner distribution) that equals that of a single "ideal" (smooth) band-pass filter. This means that the mountain ridges of the different transducers in the Wigner distribution have to be aligned in the time direction. Also, the ears of the various transducers in the crossover frequency region have to cancel each other. In principle this can be achieved, since the Wigner distribution of the sum of two transducers equals the sum of the Wigner distributions of the separate transducers plus an additional contribution, the cross-Wigner distribution of the two transducers [Eq. (14)]. With a first-order crossover it is indeed possible to obtain a complete cancellation of the ears. To optimize the time–frequency behavior of a combination of transducers we have the following degrees of freedom:

1) The crossover frequencies can be shifted.

2) The roll-off slopes in the crossover frequency regions can be adjusted.

3) The amplitude levels of the signals of the different transducers can be adjusted.

4) A time delay between different transducers can be obtained, for example, by choosing another geometrical mounting.

The range over which quantities can be varied depends, among other things, on the regions at which the separate transducers can be considered to be an adequate approximation of a band-pass filter.

Some typical deviations from the "ideal" bandpass behavior of the combination of transducers are as follows (other deviations are of course the deviations of the separate transducers):

1) The transducers are not aligned in the time direction.

2) The crossover network shifts the acoustic centers of the individual transducers.

3) The amplitude levels of the signals of the different transducers are not equal to each other.

Let us consider now some examples of these typical deviations, and also have a look at the Wigner distribution of a system whose behavior is approximately linear-phase.

1) *Improper Alignment.* An example of an improper alignment is given in Figs. 60 and 61, where the Wigner distributions of a woofer and a squawker loudspeaker are shown.

This improper alignment can easily be corrected by shifting a transducer in the time direction, for example, shifting mechanically in the direction parallel to the axis of the transducer. It is clear that especially the contour plot of the Wigner distribution is a powerful tool for investigating the influence of time-delay distortion, also commonly known as phase distortion. (A discussion of phase distortion can be found in [33], [35], and [36].)

It is worth remarking that the time delays are not necessarily caused by differences of path length or by

an incorrect mechanical alignment of the different transducers. Bode has shown [38] that any high-frequency attenuation gives a time delay of the low-frequency components. This time delay increases when we decrease the cut-off frequency or increase the steepness of the attenuation curve. It means that a woofer always has a relative delay when we compare its time–frequency behavior to that of a squawker or a tweeter loudspeaker.

It is important to pay attention to the influence of a crossover filter, which causes an additional delay. The choice of a crossover filter also has consequences for the mounting of a transducer.

Another filter which causes an additional delay is the antialiasing filter that was used when we measured the impulse response of the transducer. This complicates the determination of the relative time delay of two transducers whose impulse responses were measured using different antialiasing filters.

2) *Influence of Crossover Filter*. An example of another deviation from the ideal time–frequency behavior which is caused by a crossover filter is shown in Figs. 62 and 63. The Wigner distribution of the single squawker loudspeaker resembles that of an "ideal" band-pass filter, but the combination with a crossover filter causes large deviations at the low-frequency side of the time–frequency response. The response in the time direction of these frequencies consists of three separate contributions.

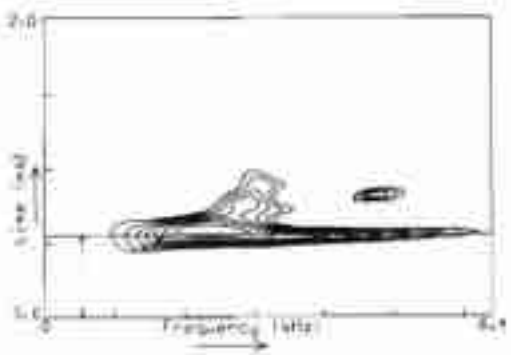

Fig. 60. Contour plot of the Wigner distribution of a woofer loudspeaker. The woofer is mounted in the same baffle as the squawker in Fig. 61.

Fig. 61. Contour plot of the Wigner distribution of a squawker loudspeaker. The squawker is mounted in the same baffle as the woofer in Fig. 60.

3) *Transducers with Different Levels*. Although the Wigner distribution of the combination contains the information concerning the levels (the integral of the Wigner distribution over all times at a fixed frequency equals $|F(\omega)|^2$), it is not always easy to retrieve this information from the distribution. The easiest way to check the levels is to determine $|F(\omega)|$ directly from the impulse response.

4) *Linear-Phase System*. The previous examples of single transducers or combinations of transducers were all minimum-phase systems. However, it is also possible to design a combination of transducers as an approximation of a linear-phase system. Fig. 64 shows the Wigner distribution of a combination designed as a linear-phase system (note the reversed time direction). The corresponding contour plot is shown in Fig. 65. The ears start at earlier times than those of a minimum-phase system as was expected, but they are not parallel

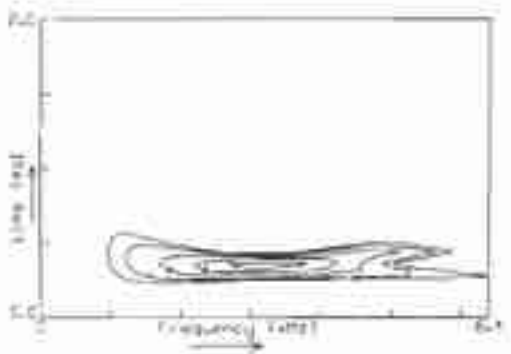

Fig. 62. Contour plot of the Wigner distribution of a squawker.

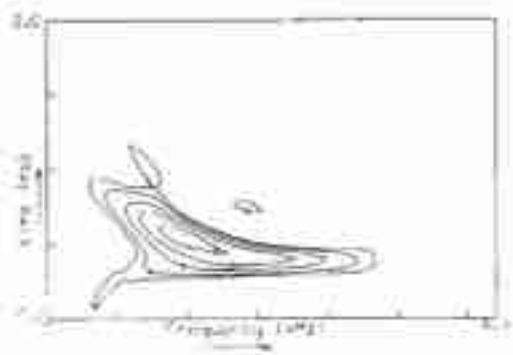

Fig. 63. Contour plot of the Wigner distribution of the same squawker in combination with a crossover filter.

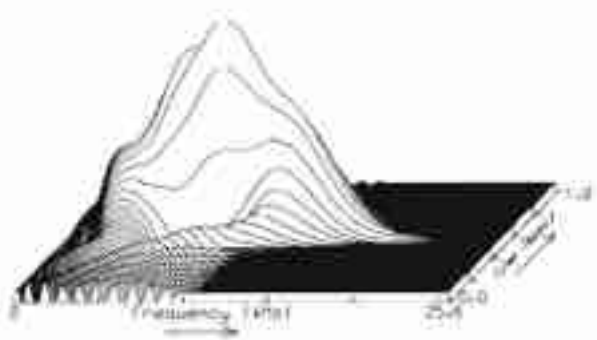

Fig. 64. Wigner distribution of a linear-phase loudspeaker design.

to the time axis. In Section 2.5 we will discuss the usefulness of a loudspeaker system designed as a linear-phase system.

Again, these examples indicate that the Wigner distribution can also be a powerful tool for optimizing the time–frequency behavior of a combination of transducers or a loudspeaker box. The Wigner distribution gives important information on the time alignment of the individual transducers and on the influence of the crossover network on the transient response.

2.3 Some Remarks Concerning the Practical Use of the Wigner Distribution

In this section we will make some remarks concerning the practical use of the Wigner distribution which would not have been relevant in the previous sections.

The first remark concerns the measurement of an impulse response, which is necessary for the evaluation of the Wigner distribution. Unfortunately a Dirac pulse cannot be physically realized. Instead we excite the system with a pulse having a finite width. The response of the system to this pulse has a close resemblance to the true impulse response of the system for those frequencies where the Fourier transform of the pulse has (almost) a constant magnitude. The extent of this frequency region to higher frequencies is inversely proportional to the width of the time pulse. However, the signal-to-noise ratio increases as the pulse is made wider. A good compromise between a broad frequency region and a reasonable signal-to-noise ratio is a pulse width of approximately 10 μs [2]. In that case the useful frequency range is about 20 kHz. To improve the signal-to-noise ratio further we have to apply signal averaging [37]. If the measurement is carried out in an anechoic room, the number of averages can be reduced because of the low background level. Also, the repetition rate can be increased due to the low reverberation time, saving time for the total measuring procedure. A disadvantage of this direct method is that the response includes the characteristics of the power amplifier. This must, therefore, be of a very high quality.

This requirement can be avoided if we determine the transfer function between the electrical input of the loudspeaker and the pressure of the measuring microphone. (The Wigner distribution can also be evaluated from frequency domain data.) In that case it is possible to use white noise or pseudo-random noise, which provides the excitation signal with a larger energy content.

But even then signal averaging has to be applied. A disadvantage is the need for a larger amount of computational power which may increase the measuring time. A hardware two-channel analyzer might be advantageous in this case. Another possibility for determining the transfer function, with a good signal-to-noise ratio and a small number of averages, is the application of a chirp signal [3]. However, we must realize that the sweeping filter necessary for this method effectively causes an averaging of the time–frequency response.

Another remark concerns the aliasing that might occur when evaluating the Wigner distribution. In Section 1.4.2 it was shown that the evaluation of the Wigner distribution from the time domain data requires a sampling rate four times greater than the largest frequency component of the signal. This can be obtained by adjusting the cut-off frequency of the antialiasing filter. Also, the antialiasing filter affects the measured value of the acoustic center of the system as discussed in Section 2.2. This cannot be neglected since antialiasing filters have a large roll-off rate. A similar problem arises when the Wigner distribution is evaluated from frequency domain data. In that case an aliasing in the time direction might occur.

Another point that requires attention is the representation of a Wigner distribution of a system with a broad frequency range. At lower frequencies the energy of the system is spread over a longer time period than at higher frequencies, resulting in a lower level of the distribution at lower frequencies when the magnitude of the frequency response of the system has a constant or an almost constant value. The reason is that the integral over all times at a fixed frequency equals the energy spectral density $|F(\omega)|^2$. This might cause some difficulties when we interpret such a distribution, since variations at the lower frequencies are not always visible due to their low level.

Several methods can be used to improve the display of such a distribution, but some of them introduce additional difficulties.

1) When the frequency region of interest is not very large, the best method is to display a constant time interval with a linearly varying ω and t. The plots in this paper were made with this method.

2) When the frequency range of interest is large, it makes sense to split the frequency axis into several parts which can be displayed with an appropriate time and frequency interval.

3) The time scale can be converted into a fixed number of periods. Instead of a linear time scale we get a period scale. The time compression must be accompanied by a (corresponding) scale of the amplitude according to the amount of time compression, so that the integral over all periods at a fixed time equals the energy spectral density. A disadvantage of this representation is that time delays are difficult to interpret.

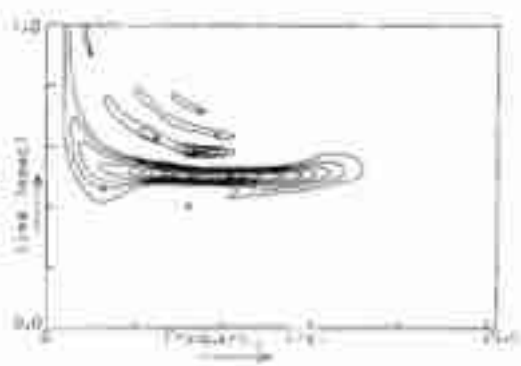

Fig. 65. Contour plot of Fig. 64.

4) It is possible to plot the values of the distribution on a logarithmic scale, so that a small value is more easily visible. However, the interpretation of the alternating interferences is more difficult. Positive and negative parts cancel when averaging over an area with appropriate dimensions, which is difficult to see on a logarithmic scale.

The purpose of studying different methods of display is to find a representation which is able to emphasize those aspects of the distribution in which we are interested. An example of this is the level of a transducer, which can be determined more easily from the magnitude of its frequency response than from the Wigner distribution, although this distribution contains all the information required. It is important to realize that, although all representations or averages of the Wigner distribution are allowed, the problems with the interpretation have to be solved with the original Wigner distribution.

An example is the attack of the time–frequency response of a loudspeaker. The Wigner distribution of a loudspeaker is mostly determined from the analytic signal. However, the analytic signal gives a spreading in the time direction, especially at low frequencies. In most cases this results in a small disturbance in the attack of the time–frequency response of the loudspeaker. If we wish to observe the effect of the attack in more detail, we have to return to the Wigner distribution of the original real-valued signal.

2.4 Cumulative Spectra

Cumulative spectra have frequently been used in recent years for the evaluation of loudspeakers [2]. In Section 1.5 it was shown that the cumulative spectrum is in fact a special type of spectrogram. It is a special type because the window function is a step function. It was shown that the spectrogram for any point (t, ω) of the time–frequency plane is the value of an integral in the time direction of the Wigner distribution of the weighted signal. This means that the derivative of the cumulative spectrum with respect to time has a closer resemblance to the Wigner distribution than the cumulative spectrum itself. An important point is the difference in physical interpretation of the Wigner distribution and the cumulative spectrum. The Wigner distribution shows a distribution of the signal energy into time and frequency, while the cumulative spectrum shows, at any ω, the square magnitude of the system time response to a sudden started or stopped sine wave. In Section 1.5 it was shown that the suddenly starting or stopping of the signal yields a broadening of the frequency spectrum. Thus we are dealing in fact with the response of the system to a combination of a sine wave and a broadband signal, which hampers the interpretation. This is the reason why appreciable contributions always are found in the stopband of the system. If we compare the Wigner distribution and the cumulative spectrum of a loudspeaker (shown in Figs. 66 and 67 for a dome tweeter) this is clearly visible.

It is our opinion that because the Wigner distribution is a distribution of the signal energy in time and frequency, it gives us greater insight into the physical processes which take place in a loudspeaker than the cumulative spectrum, which shows the response of the system to a suddenly started or stopped sine wave, with the above-mentioned disadvantages. More or less similar remarks hold for other representations.

2.5 Discussion

In Section 2 we have discussed the application of the Wigner distribution to loudspeakers. It is known that the impulse response function of a loudspeaker is a rapidly decaying function of time, and this has the great advantage that the practically evaluated pseudo-Wigner distribution resembles the theoretical Wigner distribution very much. Furthermore the impulse response is intrinsically a nonstationary signal, and therefore we cannot use the spectrogram which was shown to give useful information only if the signal is stationary during the window time. The pseudo-Wigner distribution is capable of coping with such nonstationary signals, and it was shown to be a powerful tool for evaluating the (transient) time–frequency response of a loudspeaker.

The Wigner distribution allows the introduction of objective optimization criteria for both a single transducer and a combination of transducers. Deviations from the ideal behavior can be located. For example, the decaying ringing contributions of the bending and membrane resonances of cone and dome loudspeakers, as well as time delays and reflections, can be recognized from the occurrence of spurious contributions.

To simplify the interpretation of the distribution or to emphasize particular effects, it may be convenient to use an adapted representation. Examples are the use of the analytic signal to suppress disturbing interference contributions and the contour plot, in which time delays are easily recognized. In order to suppress disturbing or irrelevant contributions, one could also average the distribution with a suitable window. It is important to note that although such processing may make sense, we always have to return to the Wigner distribution of the original signal if we have any problem with the interpretation of a particular representation. It may be

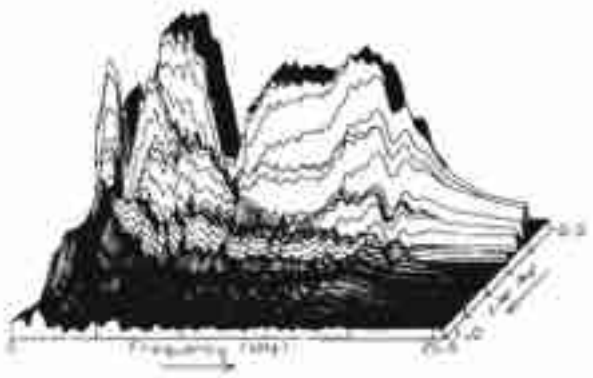

Fig. 66. Cumulative decay spectrum of a dome tweeter.

advantageous to carry out a conversion of the axes, such as a logarithmic frequency or amplitude scaling. This might be important when the deviations of the time–freqaency behavior from the ideal behavior are to be emphasized. This is closely related to the audibility of phenomena, which is not discussed in this paper. It is clear that for a proper evaluation of the significance of deviations from ideal time–frequency responses it is important to know something about the audibility of these deviations. However, the audibility of many transient phenomena is not yet known.

If a satisfactory theory could be found for this important domain of acoustical perception, it might be possible to average the Wigner distribution with an appropriate function, which would result in a representation showing only the audible contributions of the distribution. Given the state of the art of knowledge about the perception of acoustical transient phenomena and the ability to formulate mathematical or physical models of this hearing mechanism, this requires much additional research.

The Wigner distribution can, in our opinion, be very useful in this study, since it gives a proper distribution of the energy of the stimulus signal, which allows an accountable application of weighting, averaging, and transformation.

Another point that requires much attention is the influence of the directivitity of a loudspeaker. An impulse response on the axis is not a complete description of a transducer. Any point in space will give a different impulse response and Wigner distribution. Many impulse responses and many Wigner distributions can be determined, but it is difficult to assign priorities to these Wigner distributions.

A possible solution is to place the transducer in a normal listening room and to measure the impulse response of the transducer at the listening position. This impulse response contains relevant information about the system performance, the directivity, and the room parameters. The interpretation of the Wigner distribution of this impulse response, however, requires more additional research.

As a last point we shall consider the usefulness of a linear-phase loudspeaker design (not to be confused with time alignment of separate transducers). Such an approximated linear-phase behavior is often claimed to affect the transient response of a loudspeaker favorably. From the Wigner distributions of the minimum-phase and linear-phase filter systems (Figs. 18 and 21) it is clear that the only differences are the position of the ears relative to the mountain ridge and the delay of this mountain ridge.

The ears of a practical loudspeaker system are located in frequency regions that are assumed to have almost no influence on perceptional phenomena. If these frequency regions are not considered to be important, then there is no difference between the minimum-phase and the linear-phase systems. Also it is known that the stereo image is determined mainly by the "attacks" in the music [39]. If the lowest and highest frequency regions would be important for the stereo imaging, then the ears of a linear-phase system would influence strongly the attacks of the music. In our opinion this indicates that the need to design a loudspeaker system with an approximated linear-phase behavior is questionable.

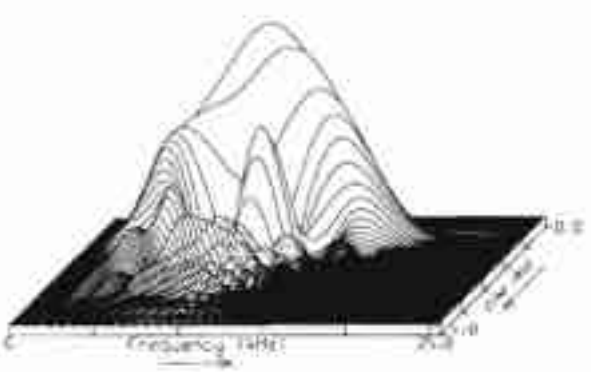

Fig. 67. Wigner distribution of the dome tweeter of Fig. 66.

3 ACKNOWLEDGMENT

The authors would like to express their gratitude to Dr. T. A. C. M. Claasen and Dr. A. J. E. M. Janssen of Philips Research Laboratories and to Prof. Dr. W. F. G. Mecklenbräuker of the Technical University of Vienna for many valuable discussions. Furthermore the authors wish to thank Dr. J. M. van Nieuwland of the Philips Research Laboratories and Prof. Dr. W. F. G. Mecklenbräuker for encouragement in this research.

4 REFERENCES

[1] A. Papoulis, *The Fourier Integral and Its Application* (McGraw-Hill, New York, 1962).

[2] J. M. Berman and L. R. Fincham, "The Application of Digital Techniques to the Measurement of Loudspeakers," *J. Audio Eng. Soc.*, vol. 25, pp. 370–384 (1977 June).

[3] H. Biering and O. Z. Pedersen, "Free Field Techniques," Brüel and Kjaer, Naerum, Denmark, 1981.

[4] R. B. Randall, "Application of BK Equipment to Frequency Analysis," Brüel and Kjaer, Naerum, Denmark, 1977.

[5] R. C. Heyser, "Acoustical Measurements by Time Delay Spectrometry," *J. Audio Eng. Soc.*, vol. 15, p. 370 (1967).

[6] D. C. Hamill, "Transient Response of Audio Filters," *Wireless World* (1981 Aug.).

[7] E. Wigner, "On the Quantum Correction for Thermodynamic Equilibrium," *Phys. Rev.*, vol. 40, pp. 749–759 (1932).

[8] J. Ville, "Théorie et Applications de la Notion de Signal Analytique," *Cables et Transmissions*, vol. 20A, pp. 61–74 (1948).

[9] N. G. de Bruijn, "A Theory of Generalized Functions, with Applications to Wigner Distribution and Weyl Correspondence," *Nieuw Arch. Wiskunde*, vol. 21, pp. 205–280 (1973).

[10] T. A. C. M. Claasen and W. F. G. Mecklen-

bräuker, "The Wigner Distribution—A Tool for Time-Frequency Analysis; Part I: Continuous-Time Signals," *Philips J. Res.*, vol. 35, pp. 217–250 (1980).

[11] T. A. C. M. Claasen and W. F. G. Mecklenbräuker, "The Wigner Distribution—A Tool for Time-Frequency Analysis; Part II: Discrete-Time Signals," *Philips J. Res.*, vol. 35, pp. 276–300 (1980).

[12] T. A. C. M. Claasen and W. F. G. Mecklenbräuker, "The Wigner Distribution—A Tool for Time-Frequency Analysis; Part III: Relations with Other Time-Frequency Signal Transformations," *Philips J. Res.*, vol. 35, pp. 372–389 (1980).

[13] T. A. C. M. Claasen and W. F. G. Mecklenbräuker, "Time-Frequency Signal Analysis by Means of the Wigner Distribution," *Proc. 1981 ICASSP*, pp. 69–72.

[14] M. A. Gerzon and R. C. Heyser, "Comments on 'The Delay Plane, Objective Analysis of Subjective Properties: Part I,'" *J. Audio Eng. Soc. (Forum)*, vol. 22, pp. 104–106 (1974 Mar.).

[15] L. Cohen, "Generalized Phase-Space Distribution Functions," *J. Math. Phys.*, vol. 7, pp. 781–786 (1966).

[16] H. Margeneau and L. Cohen, "Probabilities in Quantum Mechanics," in *Quantum Theory and Reality*, M. Bunge, Ed. (Springer, Berlin, 1967), chap. 4, pp. 71–89.

[17] B. Bouachache *et al.*, "Sur une Condition Nécessaire et Suffisante de Positivité de la Représentation Conjointe en Temps et Fréquence des Signaux d'Énergie Finie," *C. R. Acad. Sci. Paris*, vol. 288, pp. 307–309 (1979 Jan.).

[18] A. J. E. M. Janssen, "On the Locus and Spread of Time-Frequency Pseudo-Density Functions," *Philips J. Res.*, vol. 37, pp. 79–110 (1982).

[19] A. W. Rihaczek, "Signal Energy Distributions in Time and Frequency," *IEEE Trans. Inform. Theory*, vol. IT-14, pp. 369–374 (1968).

[20] P. Johannesma *et al.*, "The Phonochrome: A Coherent Spectro-Temporal Representation of Sound," *Hearing Res.*, vol. 5, pp. 123–145 (1981).

[21] M. J. Levin, "Instantaneous Spectra and Ambiguity Functions," *IEEE Trans. Inform. Theory*, vol. IT-10, pp. 95–97 (1964).

[22] C. H. Page, "Instantaneous Power Spectra," *J. Appl. Phys.*, vol. 23, pp. 103–106 (1952).

[23] L. R. Rabiner and R. W. Schafer, *Digital Processing of Speech Signals* (Prentice-Hall, Englewood Cliffs, NJ, 1978).

[24] A. J. E. M. Janssen, "A Note on Hudson's Theorem about Functions with Non-Negative Wigner Distributions," *SIAM J. Math. Anal.* (to be published).

[25] N. G. de Bruijn, "Uncertainty Principles in Fourier Analysis," in *Inequalities*, O. Shisha, Ed. (Academic Press, New York, 1967), pp. 57–71.

[26] T. A. C. M. Claasen and W. F. G. Mecklenbräuker, "A Note on Aliasing in Discrete-Time Wigner Distributions," *IEEE Trans. Acoust., Speech, Signal Proc.* (to be published).

[27] D. S. K. Chan, "A Nonaliased Discrete-Time Wigner Distribution for Time-Frequency Signal Analysis," *Proc. 1982 ICASSP*, Paris.

[28] L. R. Rabiner and B. Gold, *Theory and Application of Digital Signal Processing* (Prentice-Hall, Englewood Cliffs, NJ, 1975).

[29] J. Dugundji, "Envelopes and Pre-Envelopes of Real Waveforms," *IRE Trans. Inform. Theory*, p. 53 (1958 Mar.).

[30] S. H. Linkwitz, "Active Crossover Networks for Noncoincident Drivers," *J. Audio Eng. Soc.*, vol. 24, pp. 2–8 (1976 Jan./Feb.).

[31] G. Kraus, "Eine Interpretation der Gruppenlaufzeit," *Frequenz*, vol. 36, no. 7–8, pp. 203–205 (1982).

[32] W. F. G. Mecklenbräuker, "Gruppenlaufzeit und Laufzeit der Signalenergie in Kausalen Linearen Systemen," *Arch. Elektronik übertragungstech.* (to be published).

[33] R. C. Heyser, "Loudspeaker Phase Characteristics and Time Delay Distortion, Parts I and II," *J. Audio Eng. Soc.*, vol. 17, p. 30 (1969 Jan.); p. 130 (1969 Apr.).

[34] A. J. M. Kaizer, "Theory and Numerical Calculations of the Vibration and Sound Radiation of Non-Rigid Loudspeaker Cones," presented at the 10th International Congress on Acoustics, Sydney, 1980.

[35] D. Preis, "Phase Distortion and Phase Equalization in Audio Signal Processing—A Tutorial Review," *J. Audio Eng. Soc.*, vol. 30, pp. 774–794 (1982 Nov.).

[36] R. C. Heyser, "Determination of Loudspeaker Signal Arrival Times, Parts I–III," *J. Audio Eng. Soc.*, vol. 19, pp. 734–743 (1971 O...); pp. 829–834 (1971 Nov.); pp. 902–905 (1971 De...).

[37] J. S. Bendat and A. G. Piersol, *Random Data: Analysis and Measurement Procedures* (Wiley, New York, 1971).

[38] H. W. Bode, *Network Analysis and Amplifier Feedback Design* (van Nostrand, Princeton, NJ, 1946).

[39] N. V. Franssen, "Some Considerations on the Mechanism of Directional Hearing," Thesis, Technische Hogeschool Delft, The Netherlands, 1960.

4. Numerical calculation of the vibration and sound radiation of nonrigid loudspeaker cones[1]

In Section 2 the lumped parameter model of the electrodynamic loudspeaker was discussed. This model assumes that the sound radiation of a loudspeaker resembles closely that of a plane, rigid piston in an infinite baffle. Because of this assumption it predicts the sound radiation of an actual loudspeaker with an acceptable accuracy only at low frequencies. At higher frequencies the vibrational behavior of the diaphragm itself comes into play as well. In fact, the radiated sound power above the transition frequency is much larger than that predicted by the lumped parameter model. This is illustrated in Fig. 4.1 for a cone-type diaphragm.

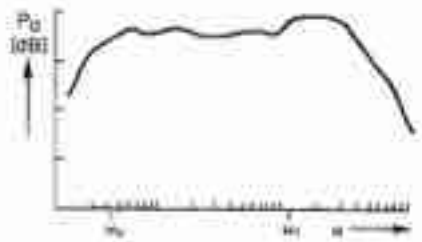

Fig. 4.1. Measured radiated power P_a of a cone-type loudspeaker as a function of the frequency (cf. Fig. 2.5).

Cone-type loudspeakers (cf. Fig. 4.13) are the most common in use, and we will therefore concentrate on this type of diaphragm geometry in our discussion. The dynamic behavior of a nonrigid loudspeaker cone can be calculated using thin shell theory [9-12], as proposed by Frankort [13]. The cone is a thin curved plate or shell, which is excited at one side. The differential equations that describe the dynamic behavior of a cone or dome are then derived using thin shell theory.

Throughout the remainder of this section we will restrict ourselves to shells of revolution with an axisymmetric excitation. Furthermore, all the geometrical parameters refer to the middle surface of the (thin) shell.

A cone-type shell of revolution is shown in Fig. 4.2.a and its geometrical parameters are defined according to Figs. 4.2.b and c. The parameter R_φ is the radius of curvature[2] in the meridional direction, ξ is the meridional coordinate, i.e. the distance measured from an arbitrary origin along the meridian, φ is the angle between the normal on the shell surface and the axis of symmetry, r is the distance of a shell element from the axis of symmetry and $R = r/\sin(\varphi)$. The parameter R_φ is related to the meridional coordinate ξ by $d\varphi = 1/R_\varphi \cdot d\xi$. In the case of a straight conical shell (Fig. 4.13b) R_φ is infinite and its inverse vanishes: $1/R_\varphi = 0$. For a plane plate both $1/R_\varphi$ and φ equal zero.

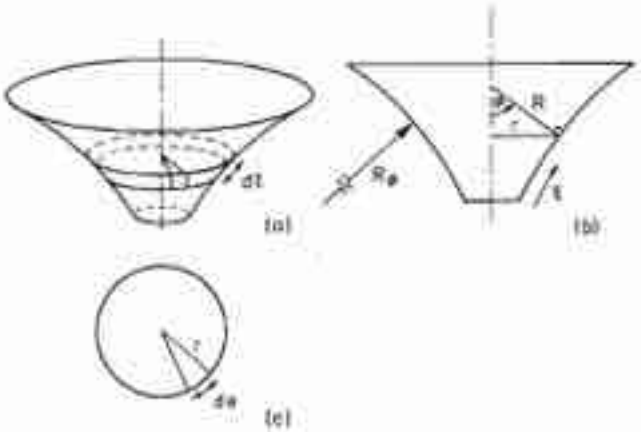

Fig. 4.2. A cone-type shell of revolution (a) and cross-sections of this shell parallel to a meridian (b) and perpendicular to the axis of symmetry (c).

The stresses acting on a shell element are depicted in Fig. 4.3a, where σ_ξ, σ_ϑ and σ_z are normal stresses and the other are shearing stresses. The azimuthal coordinate is denoted by ϑ and the transverse coordinate by z. ($-h/2 \leq z \leq h/2$, where h denotes the shell thickness.)

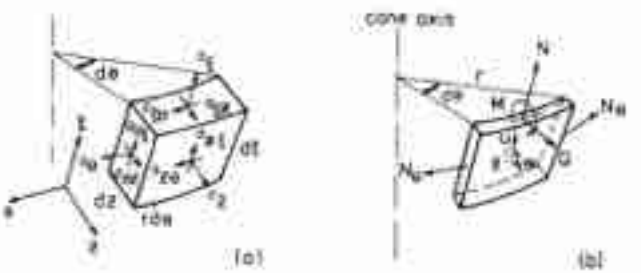

Fig. 4.3. An element of the shell of revolution of Fig. 4.2.

In the analysis we use a set of differential equations, derived by Reissner [12,19], that describe the vibrational behavior of a thin shell. This author started from four basic assumptions, which were proposed by Love [14]:

1. The shell is thin, i.e. the thickness of the shell is small compared with its radii of curvature.
2. The displacements of the shell are small. The equilibrium conditions for deformed elements are the same as if the elements were not deformed. This causes the differential equations to be linear.

[1] In this section the bars above the symbols for the indication of a complex-valued variable will be omitted.

[2] This radius of curvature can assume a negative value as is the case with a convex cone shown in Fig. 4.2b.

3. The transverse normal stress σ_z is small compared with the other normal stress components and may be neglected.
4. The normals of the undeformed surface are deformed into the normals of the deformed surface, which means that transverse shear deflections can be neglected. However, the integrated effect of the transverse shear stress, which is given by Eq. 4.3, is not neglected[3].

In the differential equations the stresses in the shell are replaced by their resultants, which are assumed to act on the middle surface of a shell element. The nonvanishing resultant forces N, N_θ, Q and the moment M [9], are given below.
The symbol N denotes the resultant force in the meridional direction per unit length, defined by:

$$N = \int_{-h/2}^{h/2} \sigma_\xi \, dz , \qquad 4.1$$

where h is the shell thickness.
Similarly we find

$$N_\theta = \int_{-h/2}^{h/2} \sigma_\theta \, dz , \qquad 4.2$$

$$\text{and } Q = \int_{-h/2}^{h/2} \sigma_{\xi z} \, dz , \qquad 4.3$$

The bending moment per unit length is given by

$$M = \int_{-h/2}^{h/2} \sigma_\xi z \, dz . \qquad 4.4$$

The displacements and rotation of and the resultant forces and moment acting on a shell element are depicted in Fig. 4.3b. The symbols U and W denote the displacements in the meridional and transverse directions, respectively, and β is the rotation of the shell element in the U,W plane.
The following analysis makes use of some additional assumptions:

- The influence of the sound radiation on the mechanical vibration is accounted for in a simplified way. The radiation impedance of a plane rigid piston with the same maximum radial dimension is assumed to be equally distributed over the diaphragm surface. This radiation impedance consists of a radiation resistance and an imaginary part. The first is combined with the diaphragm material damping and the latter leads to a radiation load mass, which can be combined with the piston mass. The radiation load mass of a rigid piston with radius a, for frequencies below the transition frequency, equals (cf. 2.2):

$$m_l = \frac{8\,\rho_0 a^3}{3} , \qquad 4.5$$

On the other hand the mass of a piston with thickness h and density ρ_c equals

$$m_p = \pi a^2 h \rho_c . \qquad 4.6$$

For a typical piston with $a = 80$ mm, $h = 0.5$ mm and $\rho_c = 600$ kg/m^3, the ratio m_l/m_p equals 0.26.
- The material is isotropic in the plane of the diaphragm, i.e. the Young's modulus is the same in all directions. If there is no preferred direction in the manufacturing of the material, this assumption is reasonable.
- The Young's modulus and the loss factor of the diaphragm material are assumed to be constant in the frequency range of interest. The effects of internal material damping and of the radiation resistance have been incorporated into the Young's modulus, which can be written in the complex form (assuming harmonic vibrations) [15,17]:

$$E(\omega) = E'(\omega) + j\,E''(\omega) = E'(\omega)\,(1 + j\delta(\omega)), \qquad 4.7$$

where $\delta(\omega)$ is the loss factor.
For many materials the loss factor δ is constant in a broad frequency range [18][4].
- The effects of rotatory inertia are neglected in the thin shell differential equations. Thin shells are characterized by the condition $h/R_1 \ll 1$, where h is the shell thickness and R_1 is the smallest radius of curvature of a shell element [9,10]. For an actual loudspeaker cone the factor h/R_1 is typically smaller than 0.01.

With these assumptions we can formulate the differential equations that describe the vibrational behavior of a shell.

4.1 The differential equations that describe the cone vibrational behavior.

The axisymmetric transverse vibration of a rotationally symmetric plane shell or plate (zero curvature) can be described by a fourth-order differential equation [16]. This transverse or "bending" vibration (for which the middle plate surface does not stretch: inextensional vibration), is responsible for the sound radiation of a plate. On the other hand the in-plane

[3] It should be noted that the vanishing transverse shear strain (no transverse shear deflection) is inconsistent with the presence of transverse shearing stresses, but these Love assumptions are nevertheless almost universally accepted by others in the field of thin shell theories [9-12].

[4] In general the real and the imaginary part of the Young's modulus as a function of frequency cannot be chosen independently, but have to satisfy the Kramers-Kronig relations: the real and imaginary parts of the Young's modulus are Hilbert transform pairs [29].

or "membrane" vibration for which there is no transverse component (the stretching of the middle surface of the plate is dominating: extensional vibration) does not contribute to the sound radiation. Bending and membrane vibrations are independent in thin plate theory.

In contrast to a plane plate, the membrane vibration in a curved plate or shell has a transverse component in the displacement. Therefore, the membrane vibration contributes to the sound radiation of the curved shell and cannot be neglected, as will be seen in Section 4.4.

An element of a shell of revolution possesses three degrees of freedom for axisymmetric vibrations: the displacements U and W in the meridional and the transverse direction, respectively, and the rotation β of the shell element. The axisymmetric vibration is then described by a single sixth-order differential equation or, equivalently, by a set of six coupled first-order differential equations [19].

The six first order differential equations can be written as two coupled vector equations:

$$\frac{d\underline{G}}{d\xi} = A_{11}\underline{X} + A_{12}\underline{G}$$

$$\frac{d\underline{X}}{d\xi} = -A_{21}\underline{X} + A_{22}\underline{G}, \qquad 4.8$$

with the property that

$$A_{12} = (A_{21})^T,$$

where T denotes a transposed matrix.

The matrices A_{11}, A_{12} and A_{22} depend upon frequency and material and geometrical parameters of the shell, as can be found in Appendix A.

The vector $\underline{G}$ is formed by the two forces and the moment acting on a shell element, $\underline{X}$ is a vector whose elements are the displacements in the meridional and transverse directions and the rotation of a shell element and ξ is the meridional coordinate, as shown in Fig. 4.2.

$$\underline{G} = \begin{bmatrix} 2\pi rQ \\ 2\pi rN \\ 2\pi rM/h \end{bmatrix}$$

$$\underline{X} = \begin{bmatrix} W \\ U \\ \beta h \end{bmatrix}, \qquad 4.9$$

where h denotes the thickness of the shell.

If we put $1/R_\varphi = 0$ and $\varphi = 0$ in Eqs. 4.8, the differential equation describe the axisymmetric transverse vibration of a circular plate, which can be written in the form:

$$\nabla^4 W = \frac{1}{r}\frac{d}{dr}\left\{r\frac{d}{dr}\left[\frac{1}{r}\frac{d}{dr}\left(r\frac{dW}{dr}\right)\right]\right\} = \frac{\omega^2 \rho h}{D_b} W, \qquad 4.10$$

where D_b is the bending stiffness as defined by Eq. 4.12. Eq. 4.10 is the well-known equation for harmonic motion of the plate [8,9].

4.1.1 Membrane (extensional) differential equations.

The set of six coupled first-order differential equations that describe the vibrational behavior of the shell of revolution has six linearly independent solutions.

From the asymptotic analysis put forward by Ross [20,21] for the set of differential equations (4.8), it appears that these solutions (if properly chosen) can be classified into two classes, except in the "transition area", i.e. in the vicinity of a ring on the shell for which the equation

$$\omega R \sqrt{\rho/E} = 1, \qquad 4.11$$

holds.

The first class consists of four solutions for which bending is the dominating mechanism. These bending solutions show a rapid spatial variation and are strongly dependent upon the shell thickness. The second class has two solutions for which the effect of bending is quite negligible. These membrane solutions are rather slowly varying functions of position and have only a weak dependence on the cone thickness.

Ross also showed [20] that the membrane solutions are well approximated by means of the membrane model[5], which is the model in which the bending stiffness D_b, given by

$$D_b = \frac{E h^3}{12(1-\nu^2)}, \qquad 4.12$$

where ν is Poisson's ratio, is assumed to vanish.

Setting $D_b = 0$ implies that the moment M and the shear force Q vanish [9] and the number of differential equations reduces to two. The differential equations for the membrane model are found by substituting $Q = 0$ and $M = 0$ in Eq. 4.8:

$$\frac{dS}{d\xi} = B_{11} U - B_{12} S$$

[5] When speaking about membrane theory, membrane stress or membrane force we do not mean that the forces are necessarily tensile forces, they can also be compressive forces.

$$\frac{dU}{d\xi} = B_{21}\, U + B_{22}\, S, \qquad 4.13a$$

where $B_{12} = B_{21}$ and $S = 2\pi r N/h$. The transverse displacement W is given by:

$$W = C_1\, U + C_2\, S \qquad 4.13b$$

The coefficients B_{11}, B_{12}, B_{22}, C_1 and C_2 are listed in Appendix A.

If the bending stiffness vanishes, the resultant set of differential Eqs. 4.13 exhibits a singularity at a ring on the cone whose position is frequency dependent. The location of this singularity on the shell, which is called the "transition point", is given by Eq. 4.11. There is a lowest and a highest frequency where this ring coincides with the shell outer and inner circle, respectively. With a nonzero bending stiffness we get a "transition area" in the vicinity of the "transition point", in which bending and stretching effects are coupled to each other.

Van der Pauw has reported [32] that in the lossless membrane model an accumulation and trapping of vibrational energy at the "transition point" occurs. This results in a dissipative driving-point admittance at the apex of a truncated conical membrane, even in the complete absence of mechanical damping in the membrane material. This phenomenon of "energy trapping" may be viewed as a conversion of power from membrane solutions to bending solutions in the "transition area".

4.2 Boundary conditions

The set of differential equations can be integrated after prescribing a number of boundary conditions that is equal to the number of first order differential equations. For the axisymmetric case, including membrane and bending (extensional and inextensional) effects, this results in six boundary conditions, three at each edge. In the boundary conditions we can prescribe the values of the variables directly or by a linear combination or a ratio of these variables.

Outer edge. If the outer edge of the cone is connected with a rim (suspension) then the outer part of this rim is a clamped edge: $W = 0$, $U = 0$ and $\beta = 0$, i.e. there is no motion at the edge.

If the influence of the rim is to be ignored, then we put a free edge at the outer boundary of the cone which means that the forces and the moment at the edge vanish: $Q = 0$, $N = 0$ and $M = 0$.

Also it is feasible to define a boundary condition as an impedance in the meridional or transverse direction or as a rotational impedance. Then we prescribe a value for the ratios N/U, Q/W, or M/β.

Inner edge. If the inner edge is attached to a voice coil former (Fig. 4.4) the axial force F_a acting on the former is provided by the Lorentz force (the voice coil is a current-carrying wire in a static magnetic field), which gives a boundary condition:

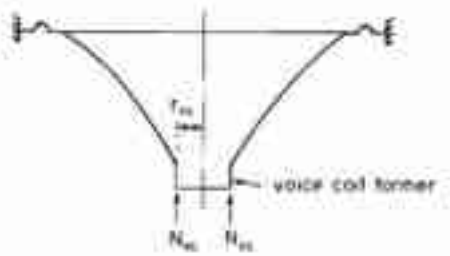

Fig. 4.4. Cone loudspeaker geometry

$$N_{ic} = \frac{F_a}{2\pi r_{ic}}, \qquad 4.14$$

The inner edge is basically a free edge and the other two boundary conditions at the voice coil former are

$$M_{ic} = 0 \text{ and } Q_{ic} = 0, \qquad 4.15$$

The relation between the axial force F_a and the Lorentz force F can be found from the analogous circuit shown in Fig. 4.5. This figure is similar to that of Fig. 2.2, except that the vibratory part, at the right-hand side of the dashed line, does not show the behavior of a simple mass-spring system, but is described by the differential equations of 4.8.

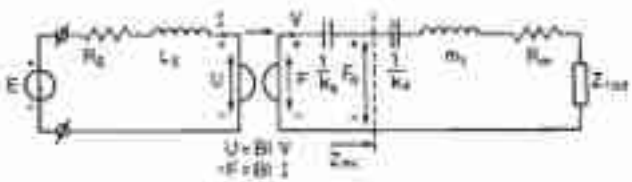

Fig. 4.5. Impedance-type analogous circuit for an electrodynamic loudspeaker

The total spring constant k_s is split into that of the combined contributions of the spider and the box air volume k_b and that of the outer edge suspension k_e. The mechanical input impedance of the nonrigid cone is

$$Z_{mc} = \frac{F_a}{V}, \qquad 4.16$$

where F_a is the axial force that acts on the voice coil and V is its axial velocity.

The effects of the spider, of the box air volume and of the electrical parameters are described by the transfer function F_a/E, which is found from Fig. 4.5.

$$\frac{F_a}{E} = \frac{Z_{mc}}{\left(Z_{mc}+\frac{k_s}{j\omega}\right)} \frac{-Bl}{\left(R_E+j\omega L_E+\frac{(Bl)^2}{(Z_{mc}+k_s/j\omega)}\right)}. \quad 4.17$$

The transfer function between the velocity of any cone point and the axial force acting on the voice coil former and also the mechanical input impedance (cf. eq. 4.16) are found from the numerical analysis.

4.3 Solving the set of differential equations

In general the set of differential equations cannot be solved analytically, and we therefore have to turn to numerical techniques. Within the framework of this thesis a brief discussion of some methods seems to be sufficient.

The method of finite differences [22].
The differential equations can be written in a scheme of finite differences and the resulting equations can be solved. This method has the disadvantage that it does not permit an automatic selection of an optimum step size of integration at each step in accordance with the desired accuracy. Therefore this method was not used in our analysis.

The method of direct integration, i.e. a Runge-Kutta [23,46] or predictor corrector [24,46] method. It can be applied conveniently to a large set of first-order differential equations with known boundary conditions at one side of the integration interval and it permits an automatic step size selection in accordance with the desired accuracy of the solution. It is not directly suitable for a problem where the boundary conditions are prescribed at either side of the integration interval. Such a problem has to be solved by constructing n independent solutions (n is the number of first-order differential equations) and by combining these solutions with appropriate constant factors to match the known $n/2$ boundary conditions at either edge. The loss of accuracy which might result from this numerical method was obviated by adopting a multisegment method of integration as proposed by Kalnins [13,19,26].
A third method exists with a completely different approach to the problem, the *finite element method* [27]. This is an attractive method, because several software packages for the analysis of mechanical vibrations that are based on this method are available.
In our numerical analysis the direct integration method was chosen because it provided a great flexibility in the experiments, which could not be obtained from a standard (finite element) software package.

4.4 Some results of the numerical analysis

The sound radiation of a loudspeaker was evaluated in two steps:
In the first step the mechanical vibration of the loudspeaker diaphragm in vacuum was evaluated numerically. The influence of the sound radiation on the mechanical vibration was accounted for by increasing both the mass of the diaphragm and the dissipative part of the Young's modulus of the diaphragm material.
In the second step the sound radiation due to the mechanical vibration, as found in the previous step, was calculated. The method used evaluates the "Helmholtz equation" (Eq. 5.1) in free space, which is discussed in next chapter.
The loudspeaker cone shown in Fig. 4.4 was evaluated using Eqs. 4.8. The boundary conditions are Eqs. 4.14 and 4.15 for the inner edge and a fixed outer edge. The measured and calculated sound pressure levels on the axis are shown in Fig. 4.6. (The material and geometrical parameters of the loudspeaker cones that have been used in the calculations discussed in this chapter can be found in Appendix B.)

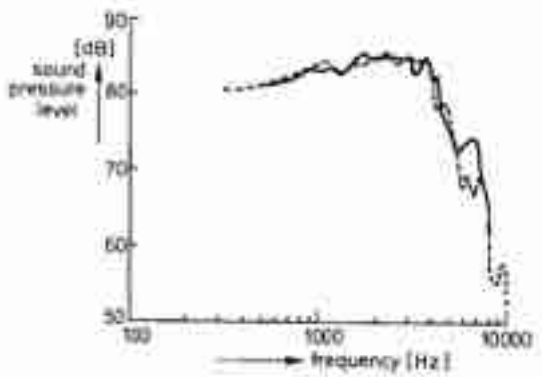

Fig. 4.6. Measured (drawn line) and calculated (dashed line) sound pressure of a cone loudspeaker.

There is a reasonable qualitative correspondence between calculated and measured results. The quantitative correspondence is not optimum which is due to the difficulty in estimating the material parameters and boundary conditions of cone parts. For example, the modeling of the glued joints in terms of Young's modulus and damping as a function of the frequency is problematic. The influence of a change of the Young's modulus of the diaphragm material is a shift of the location of peaks on the frequency axis while a change of the damping will influence the height of these peaks.
However, the analysis can be very useful in predicting

the qualitative effects of, for example, cone geometry variation, and in the remaining part of this section we will focus the attention upon the qualitative effects. The sound radiation will be approximately evaluated with the Rayleigh integral:

$$p_\omega(\underline{r}) = -j\omega\rho_0 \int\int_{S_0} \frac{e^{-jk|\underline{r}-\underline{r}_0|}}{2\pi|\underline{r}-\underline{r}_0|} V(\underline{r}_0)\, dS_0 , \quad 4.18$$

where p_ω is the sound pressure at the field point $\underline{r}$, ω is the angular frequency, ρ_0 is the density of air, $V(\underline{r}_0)$ is the velocity normal to the surface at the point $\underline{r}_0$ on the cone, k equals the ratio of the circular frequency and the velocity of a free space sound wave, $|\underline{r}-\underline{r}_0|$ is the distance between the cone point and the field point and S_0 is the cone surface. If we have a plane radiator in a plane, rigid and infinite baffle, its sound radiation can be evaluated using Eq. 4.18 [8,45].

4.4.1 Sound radiation calculation with and without bending effects.

The solutions of the differential equations can be divided into a set of bending solutions and a set of membrane solutions. This means that the sound radiation can be split into a part that results from the bending solutions and a part that results from the membrane solutions. The bending solutions have a relatively short wavelength compared with that of a free-space sound wave at the same frequency. This is illustrated in Fig. 4.7, which shows the magnitude of the calculated vibration pattern at 5 kHz of a cone with an outer diameter of 160 mm and a free outer edge.

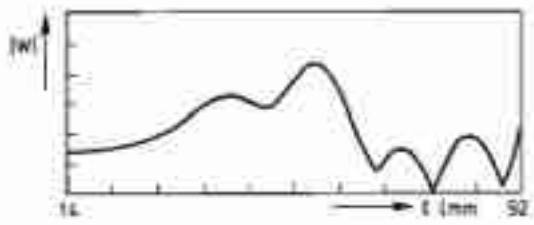

Fig. 4.7. Magnitude of the calculated transverse vibration W at 5 kHz of a cone with an outer diameter of 160 mm as a function of the meridional coordinate ξ.

The bending wavelength is of the order of 20 mm whereas the wavelength of a free space sound wave at 5 kHz is about 70 mm. Therefore, due to destructive interference, the sound radiation associated with the bending solutions, which show a rapid variation with the meridional coordinate, is relatively small [30].
The membrane solutions are well-approximated by the membrane model [20]. Fig. 4.8 shows the sound pressure of a loudspeaker, one calculated with the membrane model (Eq. 4.13) and the other with the model including bending effects (Eq. 4.8).

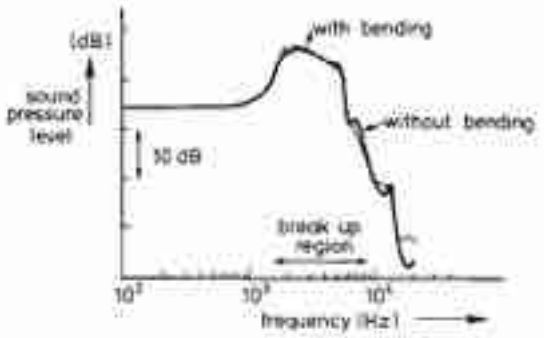

Fig. 4.8. Calculated sound pressures on the axis of a cone with an outer diameter of 166 mm.

In the calculation a free outer edge was assumed. The voice coil mass is 0.24 times the cone mass. At low frequencies there are no differences in the calculated sound pressures. In the break-up frequency range the sound radiation increases. Also a fine structure due to bending resonances appears in the diagram. The same occurs for the radiated power and the mechanical input impedance, which are not shown here. It should be emphasized that the calculations according to the membrane model require a much shorter computer time than those with the model including bending effects. The number of differential equations is reduced and the step size in the integration algorithm can be considerably increased. A small step size in the model including bending effects is necessary because of the highly oscillatory behavior of the bending solutions. Some typical vibration patterns calculated with the membrane and with the model including bending effects can be found in Ref. [31]. The much shorter computing time, at least by a factor of ten, implies an improvement in the practical usability of the theoretical model.

4.4.2 The influence of material damping and voice coil mass

In this section we investigate the influences of the material damping and of the voice coil mass. The cone vibrations were calculated using the membrane model and a free outer edge was assumed.
It is instructive to study first the sound radiation of a straight cone (Fig. 4.13b) without material damping and with vanishing voice coil mass. The differential equations that constitute the membrane model then exhibit a singularity on a ring of the cone in a limited frequency range: the break-up region. The position of the singularity on the cone meridian moves from the outer to the inner edge with increasing frequency according to Eq. 4.11. The singularity is an obstacle to numerical integration, but can be obviated by adopting a complex path of integration as proposed by van der Pauw [32].
In the following analysis the angular frequency ω and

the meridional coordinate ξ are considered as complex quantities. The integration is then carried out along an alternative path in the complex ξ-plane. The question arises whether the path of integration should be chosen above or underneath the transition point ξ_t, which is given by the equation:

$$\xi_t = (\omega\sqrt{\rho/E}\,\mathrm{cotan}\,(\varphi))^{-1}. \qquad 4.19$$

This can be solved [32] by giving ω a negative imaginary part (for an excitation of the form $\exp(+j\omega t)$), which shifts ξ_t away from the real axis into the upperhalf ξ-plane. In the limiting case $\mathrm{Im}(\omega) \to -0$, the transition point ξ_t will shift from the upperhalf ξ-plane back to the real axis and consequently the correct path of integration is underneath the transition point ξ_t.
In the numerical procedure it is convenient to introduce a new complex variable z according to

$$\coth(z) = \xi/\xi_t, \qquad 4.20$$

where the real part of ξ is the meridional coordinate on the cone. With this transformation and assuming $1/R_\varphi$ to vanish, the set of differential Eqs. 4.13a can be written in the form

$$\frac{dS}{dz} = H_{11}V - H_{12}S$$

$$\frac{dV}{dz} = H_{21}V + H_{22}S, \qquad 4.21$$

where $H_{12} = H_{21}$ and $V = U.E.$
H_{11}, H_{12} and H_{22} can be found in Appendix A.
The end points of the integration path along the real axis are the outer edge meridional coordinates ξ_a and ξ_b. The corresponding points z_a and z_b in the complex z-plane can be found from the equation:

$$z = \tfrac{1}{2}\ln\left(\frac{\xi/\xi_t + 1}{\xi/\xi_t - 1}\right). \qquad 4.22$$

For ξ_a we find $(\xi_a/\xi_t < 1)$:

$$z_a = \tfrac{1}{2}\ln\left|\frac{\xi_a/\xi_t + 1}{\xi_a/\xi_t - 1}\right| + j\frac{\pi}{2}, \qquad 4.23$$

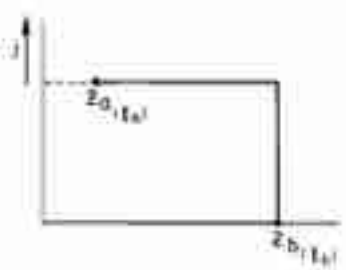

Fig. 4.9. Integration path in the complex z-plane.

and for ξ_b $(\xi_b/\xi_t > 1)$:

$$z_b = \tfrac{1}{2}\ln\left|\frac{\xi_b/\xi_t + 1}{\xi_b/\xi_t - 1}\right|. \qquad 4.24$$

The integration can be performed numerically if we choose the integration path parallel to the real and imaginary axes.
The sound radiation of the lossless cone, calculated with the membrane model, is shown in Fig. 4.10. (The Rayleigh integral was evaluated directly using the same complex integration path, obviating the need for calculating the transverse displacements of the cone explicitely).

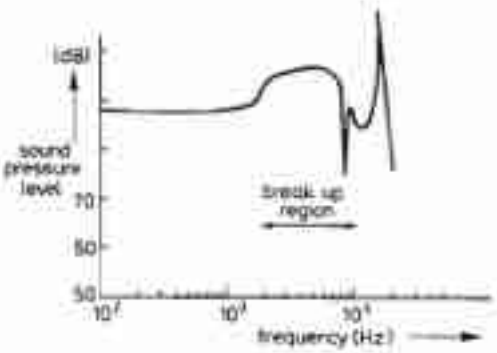

Fig. 4.10. The sound pressure of a cone with an outer diameter of 160 mm and with vanishing voice coil mass and vanishing material damping.

The break-up frequency region is the frequency range where the singularity occurs on the cone:

$$\frac{\sqrt{E/\rho}\tan(\varphi)}{\xi_b} < \omega < \frac{\sqrt{E/\rho}\tan(\varphi)}{\xi_a}, \qquad 4.25$$

and in this frequency range we find a rise in the sound radiation. The peak at 17 kHz is a membrane resonance.
Assuming the cone material to possess some damping with a loss factor δ equal to 0.1, we get the sound radiation as shown in Fig. 4.11.

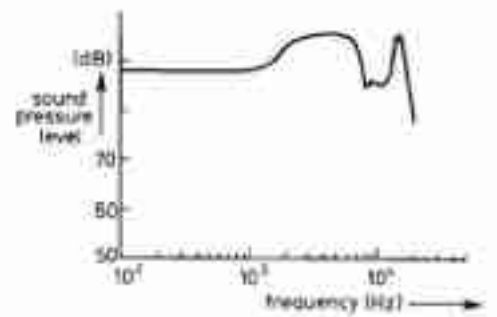

Fig. 4.11. The same as Fig. 4.10 but now with a material damping.

The next point of interest is the influence of the voice coil mass. Such an additional mass increases the total moving mass, which yields a decreased overall sound

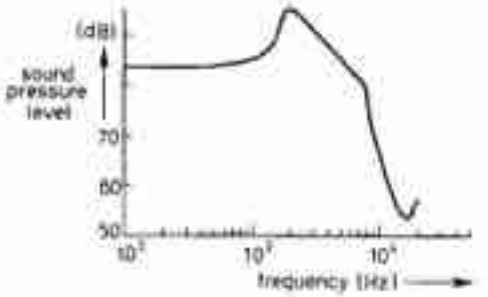

Fig. 4.12. The same as Fig. 4.11, but with a voice coil mass of 3 grams. The cone mass equals 4.8 grams.

radiation. Fig. 4.12 shows that such a voice coil mass yields an additional drop of the sound radiation in the break-up frequency region.

4.4.3 The influence of cone shape and outer edge suspension

In the preceding sections we discussed the sound radiation of a nonrigid cone with an infinite radius of curvature R_φ (conical shell). In this section we show the influence of a bent cone shape, for example a convex or concave cone shape. To this end we calculated the sound radiation of a cone-shaped radiator and those of a convex and a concave cone, both with a radius of 0.1 meters. The geometries are shown in Fig. 4.13.
In the calculations we assumed a voice coil mass of 1.5 grams and the vibrational behavior was calculated with the membrane model. Fig. 4.14 shows the sound radiation of the cone with a conical shape.
The sound pressure response resembles that of Fig. 4.12, but the roll-off slope in the break-up frequency range is smaller, due to the smaller voice coil mass.

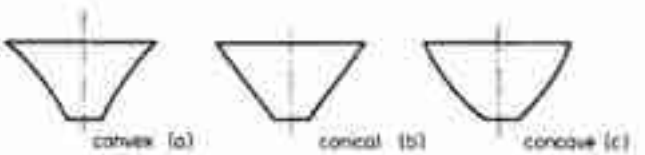

Fig. 4.13. The geometries of a convex (a), conical (b) and concave-shaped (c) cone.

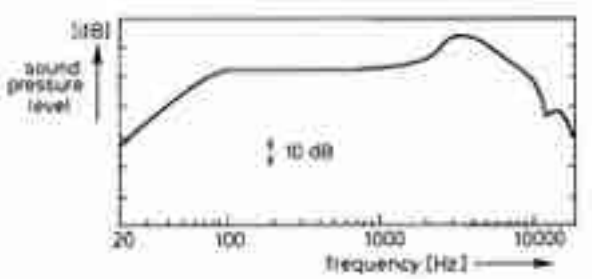

Fig. 4.14. The sound pressure response of a cone (conical shape) with an outer diameter of 160 mm and with a voice coil mass of 1.5 grams. The cone mass equals 3.5 grams.

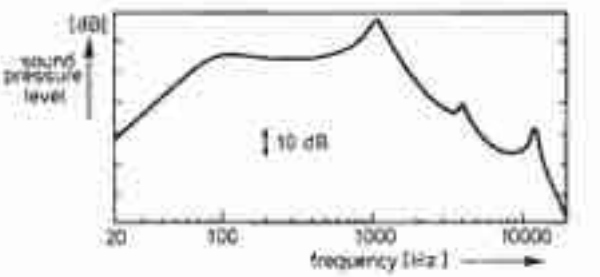

Fig. 4.15. The sound pressure response of a concave cone with a voice coil mass of 1.5 grams (outer diameter is 160 mm). The cone mass equals 3.8 grams.

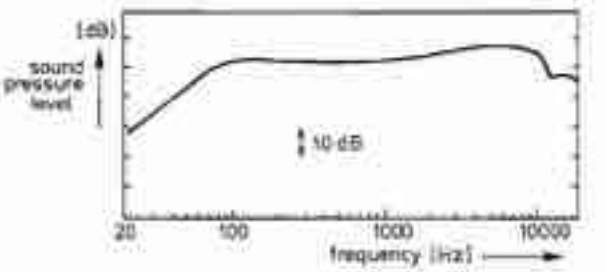

Fig. 4.16. The sound pressure response of a convex cone with a voice coil mass of 1.5 grams (outer diameter is 160 mm). The cone mass equals 3.4 grams.

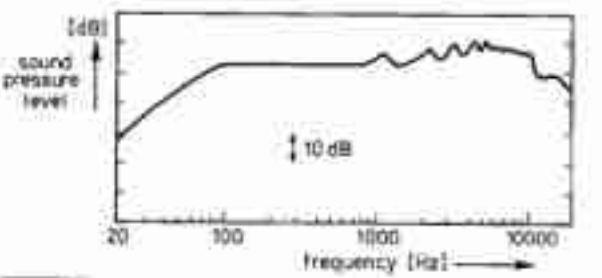

Fig. 4.17. The sound pressure response of the convex cone of Fig. 4.16, but now including bending effects.

The sound pressure response of the concave cone is shown in Fig. 4.15.
Compared with the previous cone the break-up frequency region has moved towards lower frequencies and the break-up peak is sharpened.
The third cone shape is the convex cone and its sound pressure response is shown in Fig. 4.16.
The break-up peak has disappeared and only a small gradual rise in the sound radiation response remains. Also the response shows a roll-off at much higher frequencies. However, with the convex cone, we are not allowed to ignore bending effects any more, because the shape of the outer cone part approximates that of a plane plate. In Section 4.4.1 we showed that the bending effects have a small influence on the sound radiation of a cone with a conical shape. These effects are even smaller for a concave cone shape, but for a convex cone shape the amplitude of the bending resonances increases. The sound radiation response of the convex cone, calculated with the model including bending effects, is shown in Fig. 4.17.

This response has a moving average that was correctly predicted by the membrane model calculation, but it also shows peaks and dips caused by bending resonances that can no longer be ignored. The amplitudes of these peaks and dips were found to depend strongly on the material damping.
We conclude this section with a study of the influence of the outer edge suspension or rim. The sound radiation responses of a conical-shaped cone with and without an outer edge suspension are shown in Fig. 4.18.

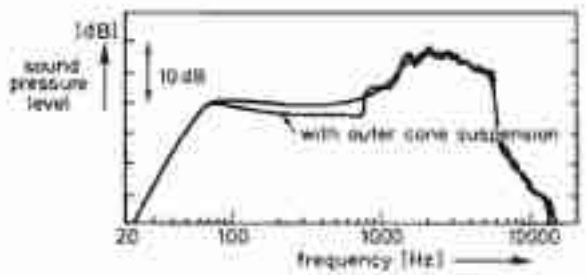

Fig. 4.18. The sound pressure responses of a conical-shaped cone with and without an outer edge suspension. The voice coil mass is 1.5 grams.

The outer edge suspension causes a dip and peak in the response below the break-up frequency region. The amplitude of the dip and peak were found to depend strongly on the outer edge suspension material damping. The rim also increases the amplitude of the peak of the second bending resonance in the break-up frequency region, as reported elsewhere [33].

4.5 Discussion

The sound radiation from a nonrigid cone shows a rise in the break-up frequency region. The average rise is correctly predicted by the membrane model, i.e. the model in which the bending stiffness vanishes. In the break-up frequency region the idealized (lossless) membrane model differential equations show a singularity on the cone, the position of which moves from the outer to the inner edge with increasing frequency according to Eq. 4.11. A trapping of energy at the singularity on the cone in the lossless membrane model was reported by van der Pauw [32], which effect results in a large transverse amplitude of the vibration at this point. This large transverse amplitude of the membrane vibration generates a bending vibration at the site of the singularity. However, bending waves cannot propagate at the inner cone part (between the inner edge and the singularity point), as shown in Ref. [25], and will decrease exponentially with displacement. At the outer cone part (between the singularity point and the outer edge), bending waves do propagate and standing (bending) waves occur. In effect, at the singularity we find a conversion from membrane energy into bending energy [32]. The influence of the material damping on the membrane vibration in the break-up frequency region is small, because the conversion of energy to bending waves can be interpreted as a damping mechaniam. On the other hand the bending waves are strongly influenced by the material damping.
The sound radiation of the nonrigid cone can be split into the contributions of the independent solutions of the differential equations that describe its vibration. In contrast to a plane plate, the membrane vibrations in the cone have a transverse component in the displacement and thus a sound radiation. In the break-up frequency region the amplitude of the transverse membrane vibration is relatively large, which results in a rise of the sound radiation in the break-up frequency region. At frequencies below the break-up frequency region bending waves cannot propagate and a generated bending wave will decay exponentially. Therefore, the sound radiation below break-up is mainly determined by the membrane solutions.
In the break-up frequency region the sound radiation due to the membrane solutions of the conical-shaped and concave cone show a considerable rise. The contributions of the bending solutions to the sound radiation of a cone with a conical shape are small compared with those of the membrane solutions and cause a fine structure on the sound pressure curve. The contributions of the bending solutions to the sound radiation of a concave cone shape are even smaller and can be neglected.
The convex cone shows only a small rise in the sound radiation of the membrane solutions. The contributions of the bending solutions to the sound radiation are much higher and can no longer be neglected. The bending solutions yield a number of bending resonance peaks and dips in the break-up frequency region.
The moving average of the sound radiation in the break-up frequency region, which is correctly predicted by the membrane model, is strongly influenced by the voice coil mass. Such a mass yields an additional roll-off of the sound radiation in this frequency region. Therefore, the sound radiation of a concave cone with voice coil mass shows a peak which originate from the membrane solutions. These membrane solutions are not very sensitive to a material damping in the break-up frequency region and the peak amplitude is hardly affected by such a damping.
The sound radiation from a convex cone with a voice coil mass shows a number of peaks and dips that originate from the bending solutions, but the moving

average does not show a rise in the break-up frequency region. The amplitudes of these peaks and dips can be decreased by increasing the material damping.

The choice of a cone shape depends on the material properties. For example, metal has a large specific mass and the thickness of a metal cone should be small in order to limit the total moving mass, which yields a small bending stiffness. The ratio E/ρ is relatively large compared with that of a commonly used cone material such as paper, so that the break-up frequency region starts at relatively high frequencies. Furthermore the material damping of a metal is small. Therefore the concave cone shape is optimum for a metal cone: the influence of the bending resonances is minimal and the break-up peak is located at relatively high frequencies.
A commonly used cone material, for example paper or plastic (e.g. polypropylene) material, has a much smaller ratio of E/ρ and a much larger material damping, which is able to damp the bending resonances effectively. Therefore the convex cone shape is optimum for such a cone material: the sound pressure response shows a smooth curve (provided that the bending resonances are damped sufficiently) which extends towards relatively high frequencies.

5. The Wigner Distribution: A Valuable Tool for Investigating Transient Distortion*

Chapter 5 contains a reprint of the article:
C.P. Janse and A.J.M. Kaizer, The Wigner Distribution:
A Valuable Tool for Investigating Transient Distortion,
JAES, vol. 32, no. 11, November 1984.

CORNELIS P. JANSE AND ARIE J. M. KAIZER

Philips Research Laboratories, 5600 JA, Eindhoven, The Netherlands

It was shown earlier that the Wigner distribution is a valuable tool for analyzing transient distortion of filters, loudspeakers, and loudspeaker combinations. Some further applications of the Wigner distribution to the evaluation of loudspeaker transient behavior are reported. The first topic is the influence of the geometry of a radiator on its transient response. The geometries discussed are the plane, cone-shaped, and dome-shaped radiators. Also dealt with is the influence of some known crossover filters on the on-axis and directional transient behavior of a combination of coincident and nonconincident drivers.

0 INTRODUCTION

In the past many representations have been used to describe the behavior of a loudspeaker system. Among them are the transfer function, which contains the amplitude and phase characteristics as a function of frequency, the impulse response, and the tone-burst response. These representations or measurements can be divided into two groups, and each represents an aspect of loudspeaker evaluation: steady-state and transient behavior. The steady-state response on axis and the steady-state directional behavior involve relatively stable conditions, and the methods developed to evaluate them are widely regarded as satisfactory.

This leaves transient behavior. Here there is little agreement on the precise effects and how to measure them. Techniques developed in the past include impulse response, group delay, tone-burst response, and cumulative spectra. All of these are well known, but none of these previously developed techniques, in fact, presents a really clear picture of the actual physical behavior under transient conditions. However, impulse response measurements are the natural approach for investigating transient behavior, and the measurements do indeed contain all the information needed, but the problem has always been how to derive insight into the physical behavior from the representation. Therefore in a previous paper [1] we proposed the Wigner distribution because of its ability to display the information contained in impulse response measurements conveniently. The Wigner distribution of a signal can be interpreted, with some care [1], as the distribution of the energy contained in the signal in both time and frequency. In the technique developed it is portrayed in a readily understood graphic form.

In principle, Wigner distribution analysis can be used for various applications. It is capable of giving a clear insight into the transient behavior of all kinds of transducers, as well as the mechanics of speech and other transient phenomena. But the major application so far developed is the analysis of loudspeaker performance [1]. The Wigner distribution can be used to evaluate, and to optimize, the transient response of individual loudspeakers or multiway combinations.

In this paper we report on some further applications of the Wigner distribution technique to the evaluation of loudspeaker transient behavior. It is assumed that the reader is familiar with the terminology used in [1].

An important application of the Wigner distribution, namely, the study of shifts and of the spreading-out effects of an impulse response in the time direction of filters and loudspeakers, is discussed. Often used for this purpose is the group delay, which gives only an indication of the location of the acoustic center. However, the group delay can be misleading in practice [1], and its accuracy can be affected seriously by reflections [2].

* Presented at the 73rd Convention of the Audio Engineering Society, Eindhoven, The Netherlands, 1983 March 15–18; revised 1984 February 15.

In Section 1 the influence of the geometry on the transient behavior of plane, cone-shaped, and dome-shaped loudspeakers is discussed. Section 2 describes the transient behavior of several well-known crossover filters, while Section 3 discusses the directional transient behavior of these filters. Finally, Section 4 contains a concluding discussion of the results obtained.

1 TRANSIENT BEHAVIOR OF CONE AND DOME LOUDSPEAKERS OF VARIOUS SHAPES

In a simplified theory the radiation impedance of a loudspeaker is often approximated by that of a rigid plane piston in an infinite baffle or at the end of a long tube [3]. However, the radiations from a plane piston and from a nonplane radiator are quite different [4]–[6]. These differences still exist for rigid radiators, and the effect is called the cavity effect. To calculate the exact sound radiation from a radiating surface with an arbitrary shape we have to solve the Helmholtz equation [7], [8]. Assuming harmonic vibrations, the integral form of this equation, provided that there are no sources in space, is given by

$$P_\omega(r) = \int_{S_0}\int \left\{ G_\omega(r|r_0) \frac{\partial}{\partial n_0} P_\omega(r_0) - P_\omega(r_0) \frac{\partial}{\partial n_0} G_\omega(r|r_0) \right\} dS_0 \,. \quad (1)$$

where $P_\omega(r)$ is the pressure in the field point r (within and on the surface area enclosed by the boundaries), r_0 is a point on the surface S_0, n_0 is the unit vector normal to the surface, and G_ω is the Green's function.

This equation can only be solved analytically for some simple shapes such as a piston in an infinite baffle or a pulsating sphere. For a plane radiator in an infinite baffle, assuming harmonic vibrations, the Helmholtz equation reduces to the Rayleigh integral [8], [9]:

$$P_\omega(r) = -j\omega\rho_0 \int_{S_0}\int \frac{e^{-jk|r - r_0|}}{2\pi|r - r_0|} V(r_0)\, dS_0 \,. \quad (2)$$

where ω is the angular frequency, ρ_0 is the density of air, k is the wave number, and $V(r_0)$ is the normal component of the velocity at point r_0 on the radiator surface S_0.

For more complicated shapes, such as cone or dome loudspeakers, the Helmholtz equation has to be solved numerically. This can be done directly using a set of integral equations [10] or with the aid of the finite-element method [11]. A detailed discussion of these numerical calculation techniques is beyond the scope of this paper.

In this section we discuss the influence of the geometry on the transient behavior of cone and dome-shaped radiators mounted in an infinite baffle. The sound radiation of these radiators is calculated using the finite-element method. The actual calculated physical quantity is the complex sound pressure at a point in space, when the radiator surface has an acceleration level independent of position and frequency in the direction of the radiator axis. The influence of the geometry on the transient behavior of the radiated sound is an extension of the steady-state radiation of a nonplane radiator, which is discussed elsewhere [4]–[6]. The Wigner distribution of such a radiator can be calculated from the complex-valued sound pressure level. This is in fact a transfer function because it was calculated with a frequency-independent acceleration level of the radiator surface.

1.1 Plane Radiator

The first example is the sound radiation of a plane, circular, and rigid piston in an infinite baffle. The complex far-field sound pressure at a field point r for harmonic excitation equals [7]

$$P_\omega(r) = \frac{\rho_0 U_{acc} S_0}{2\pi d} \frac{2J_1(ka \sin\varphi)}{ka \sin\varphi} e^{-jkd} \quad (3)$$

where d is the distance of the field point r to the center of the piston, a is the piston radius, U_{acc} is the acceleration level of the piston, φ is the angle between the axis of symmetry and the direction of the field point, and J_1 is the Bessel function.

The magnitude of the on-axis far-field sound pressure is independent of frequency:

$$|P_{ax}(r)| = \frac{\rho_0 U_{acc} S_0}{2\pi d} \,. \quad (4)$$

The contour plot of the Wigner distribution of the complex on-axis far-field sound pressure is shown in Fig. 1(a). It will be clear that according to [1], the transient behavior of this plane radiator is almost ideal.

In the following examples we will frequently use the so-called analytic signal. The reason for this is that the negative and positive frequencies in a spectrum yield disturbing interferences in the Wigner distribution. However, the negative frequencies do not give any additional information and can be ignored in the analysis. Removing the negative frequencies from the spectrum yields the analytic signal, which was discussed for this application in a previous publication [1]. Removing the negative frequencies has the consequence that the representation of the impulse response in the time domain has complex values, while the original spectrum has a real-valued impulse response. Another consequence is that the complex-valued impulse response is noncausal. The magnitude of this noncausal complex-valued impulse response, which is a function of time, is also referred to as the energy–time curve [12]. Fig. 1(b) shows the contour plot of the Wigner distribution of the analytic signal associated with the far-field sound pressure. (A contour line with index $i = 1$–9 has a height of $(1 - i/10)$ and with index

$t = 10$ a height of 0.05 times the maximum height of the Wigner distribution.) Compared with Fig. 1(a) one can see in Fig. 1(b) the noncausality of this impulse response. At lower frequencies the response is spread symmetrically in the time direction. The ear (see [1]) at the high-frequency end is due to the anti-aliasing filter which is located at 12 kHz. Fig. 1 can be used as a reference for the Wigner distributions of cone and dome-shaped radiators, which are discussed below.

1.2 Cone-Shaped Radiator

Unlike the plane piston radiator, whose on-axis sound pressure amplitude is frequency independent [Eq. (4)], a cone-shaped radiator shows a frequency-dependent on-axis sound pressure amplitude. This can already be concluded from the calculation of the sound pressure from a cone-shaped radiator using the Rayleigh integral [4], [13] (also commonly known as geometrical acoustic approximation). However, this is only a rough approximation of the exact sound radiation, since the Rayleigh integral is only valid for a plane radiator. If we calculate the sound radiation using the Helmholtz equation, the sound radiation is also frequency dependent, but the amplitude differs from that obtained from the Rayleigh integral. The calculated sound pressure shows large peaks and dips in its amplitude characteristic, an effect called the cavity effect [4]–[6]. The sound pressure calculated with the Rayleigh integral has a much smoother amplitude characteristic. The reason for this is that the Rayleigh integral takes into account only the influence of the different distances of the cone points to the field point. The Helmholtz equation, on the contrary, also takes into account standing waves or resonances in the cone cavity, which give the large peaks and dips in the amplitude characteristic.

The examples in this paper were calculated with the Helmholtz equation, which was solved numerically using the finite-element method [11]. The geometry was assumed to possess rotational symmetry. The mesh pattern that was used for the cone-shaped radiator is shown in Fig. 2. Only the sound field within and on the boundaries has to be calculated with the finite-element method. The boundaries are the vibrating cone-shaped radiator, the nonvibrating outer edge and flat apex, a part of the infinite rigid baffle, and a hemisphere, which links the inner region to the outer region. The sound pressure at any point outside the mesh region can be calculated analytically by using the sound pressure distribution on the hemispherical boundary [7].

A typical on-axis sound pressure response is shown in Fig. 3. This amplitude response has a first peak at $ka \approx \pi/2$, where k is the wave number and a is the radius of the radiator. Regarding the influence of the cone geometry, the location of this peak on the frequency axis depends on the radius a, whereas the amplitude of this peak is dependent on the cone shape. For constant a we have observed that the peak amplitude increases with increasing cone cavity volume. The transient response of the same radiator is shown in Fig. 4, which gives contour plots of the Wigner distribution of the complex on-axis sound pressure response. If Figs. 1 and 4 are compared, it will be clear that the latter has a more spread out transient response in the time direction

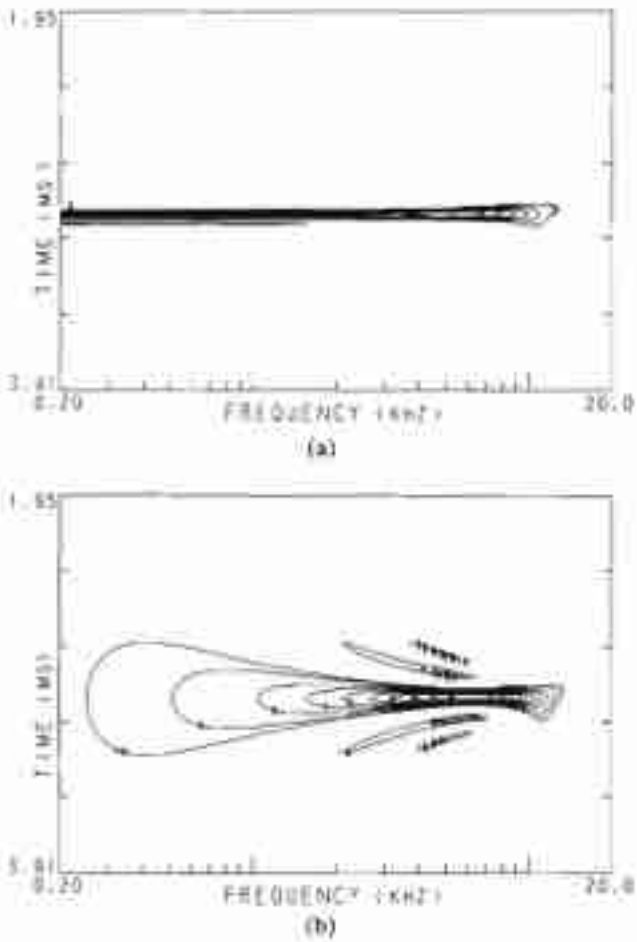

Fig. 1. (a) Wigner distribution of on-axis far-field sound pressure of rigid piston with radius $a = 97$ mm. Acceleration level of piston is constant. (b) Wigner distribution calculated with analytic signal.

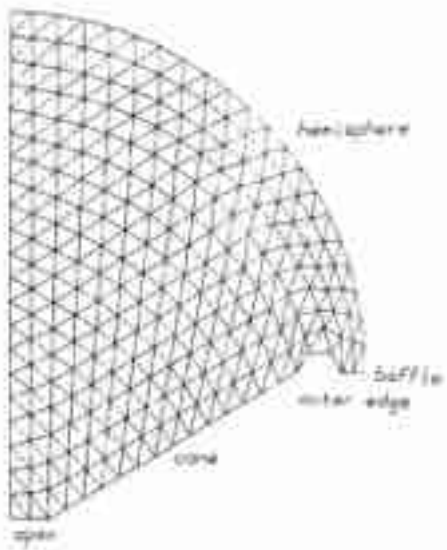

Fig. 2. Calculation mesh of cone-shaped radiator. Equivalent piston radius—97 mm; radius of outer edge has cross section—7.5 mm; radius of flat apex part—13 mm; apex angle—120°; radius of hemisphere—120 mm.

at middle and low frequencies. The first peak in the amplitude characteristic can be seen in the Wigner distribution as a spreading-out effect in the time direction. This is to be expected since the peak can be considered as a resonance; this resonance is damped by the acoustic radiation resistance of the radiator. This transient behavior is typical of all cone-shaped radiators.

It has been reported that the amplitude of the cavity dip (following the resonance peak) can be reduced by a dust cap [14]. In this case the transient response will also be improved. Figs. 5–7 show, respectively, the calculation mesh pattern, the on-axis sound pressure response, and its Wigner distributions for the loudspeakers of Figs. 2–4, but now with a vibrating dust cap. If we compare the respective figures, it will be clear that the on-axis sound pressure amplitude characteristic has been smoothed (especially the first peak and dip) and that the spreading of the transient response in the time direction has been reduced. These effects become even more pronounced if we reduce the cone cavity volume by mounting a larger dust cap.

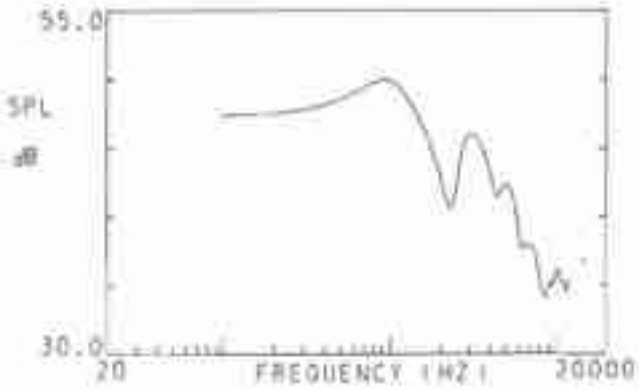

Fig. 3. Far-field sound pressure level of cone-shaped radiator with dimensions of Fig. 2.

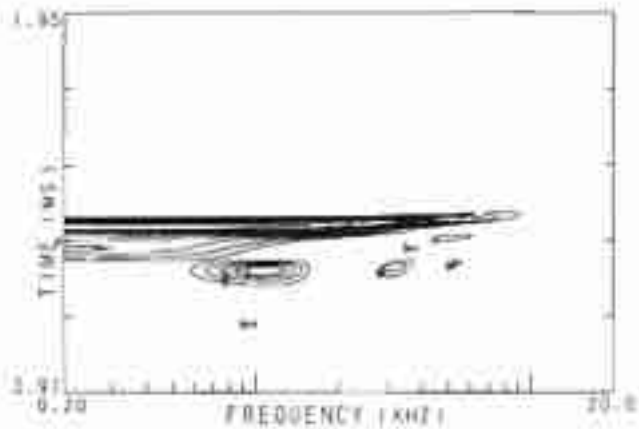

Fig. 4. (a) Wigner distribution of on-axis far-field sound radiation of Fig. 3. (b) Wigner distribution calculated with analytic signal.

In the foregoing it was shown that a cone-shaped radiator has a certain amount of transient distortion. This distortion is actually a widening of the transient response at certain frequencies and is due to cone geometry. It was also shown that this widening can be reduced by mounting a dust cap in the cone. These examples, however, were analyzed using a conical cone shape. The question arises as to what influence a bent cone shape will have, such as a convex or a concave cone. To answer this question the conical cone must be replaced by a convex and a concave cone with the same dimensions, namely, cone radius and cone depth. The mesh used in the calculation of a convex cone shape is shown in Fig. 8. The on-axis amplitude response can be found in Fig. 9, and the transient response is shown in Fig. 10. The same data for the concave cone are shown in Figs. 11–13. From these figures it will be clear that the convex cone is slightly better than the conical cone, but these differences are only marginal and mainly located at higher frequencies. Also the conical cone is slightly better than the convex cone, but again the differences are very small.

It can be concluded that the conical geometry of a radiator has a large influence on its transient sound radiation, which is widened in the time direction at middle and lower frequencies. It was further shown that an additional bending of the cone shape toward a convex or concave cone has only a small influence on the transient sound radiation behavior. Furthermore it was demonstrated that the mounting of a dust cap reduces the widening of the transient response in the time direction, an effect that becomes more pronounced with a larger dust cap, thus reducing the cone cavity volume.

1.3 Dome-Shaped Radiator

In the previous section it was shown that the amplitude of the on-axis sound pressure, radiated by a cone-shaped radiator, is frequency dependent. This contrasts with the amplitude characteristic of a plane radiator or piston, the amplitude of which is independent of frequency. For a dome-shaped radiator the amplitude characteristic is also frequency dependent. As mentioned in Section 1.2 for a cone-shaped radiator, this may already be concluded from the Rayleigh integral calculation [15] of the sound pressure for a dome-shaped radiator as well. If we calculate the sound radiation using the

Helmholtz equation, the sound radiation is again frequency dependent, but its amplitude differs from that obtained from the Rayleigh integral. The main difference is the dip in the amplitude characteristic, which shifts to much lower frequencies where the Helmholtz equation instead of the Rayleigh integral is used in the calculations.

The calculation mesh pattern used for the finite-element calculation of the Helmholtz equation can be found in Fig. 14, and the amplitude characteristic of the on-axis sound radiation from a dome-shaped radiator is shown in Fig. 15. If we compare the amplitude characteristic of Fig. 15 with that of a cone-shaped radiator, it will be clear that the former only has dips in its characteristic. The lack of peaks in the amplitude characteristic is typical of a dome-shaped radiator. Fig. 16 shows the contour plots of the Wigner distribution of the on-axis sound radiation. The transient behavior of the sound radiation from this radiator, as shown in this figure, is almost that of the plane piston of Fig. 1. Thus such a dome-shaped geometry does not cause large distortions in the transient response. The dips in the response become more pronounced if the dome height is increased, as shown in Fig. 17. The dome used here is a hemisphere, so that the dome radius of the curvature is equal to the equivalent piston radius, the latter being equal to that of Fig. 15. The first dip occurs at $ka = \pi/2$, which is much lower than that obtained with the

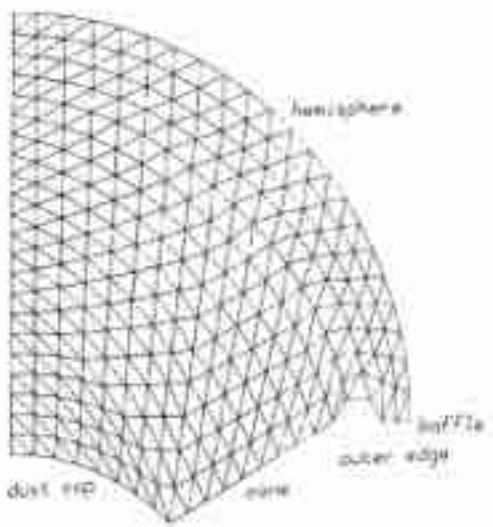

Fig. 5. Calculation mesh of cone-shaped radiator with dust cap. Radius of dust cap—66 mm; its equivalent piston radius—48 mm; other dimensions same as those in Fig. 2.

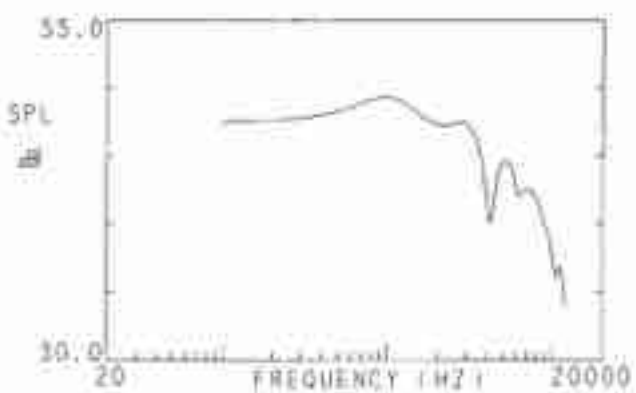

Fig. 6. Far-field sound pressure level of cone-shaped radiator with dimensions of Fig. 5.

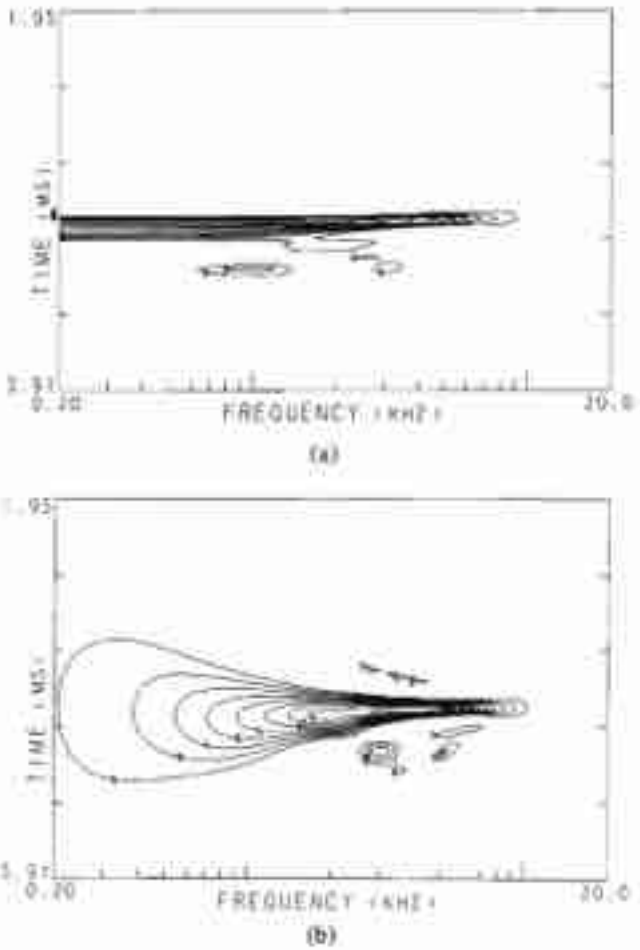

Fig. 7. (a) Wigner distribution of on-axis far-field sound radiation of Fig. 6. (b) Wigner distribution calculated with analytic signal.

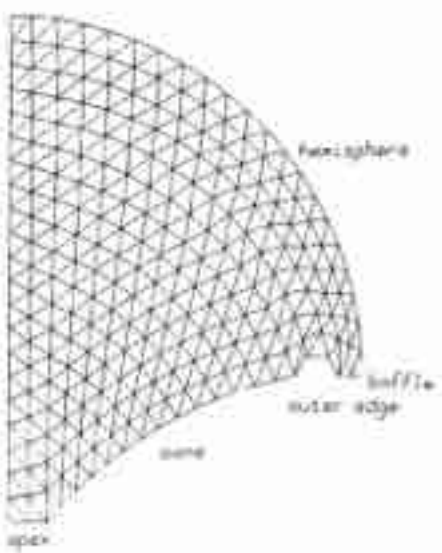

Fig. 8. Calculation mesh convex cone-shaped radiator. Radius of convex curvature—150 mm; other dimensions same as those in Fig. 2.

Rayleigh integral [5], [15]. The influence on the transient behavior, which can be seen from Fig. 18, is small.

Finally it can be concluded that the influence of a dome-shaped geometry on the transient behavior of the sound radiation is rather small. This is especially true if the ratio of the dome height to the equivalent piston radius is much smaller than unity.

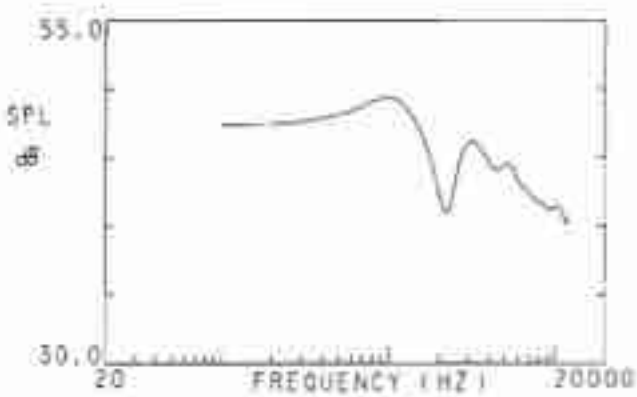

Fig. 9. Far-field sound pressure level of convex cone-shaped radiator with dimensions of Fig. 8.

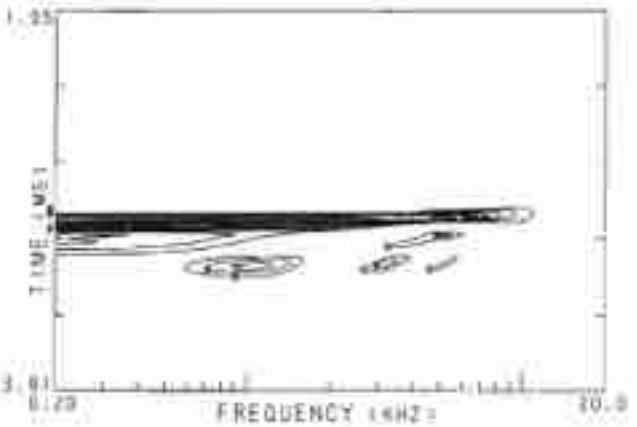

(a)

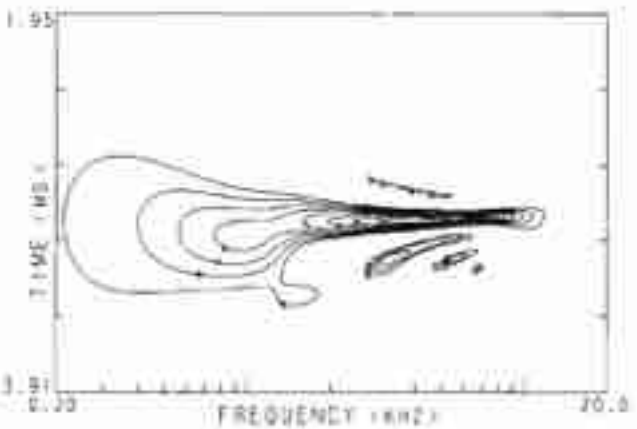

(b)

Fig. 10. (a) Wigner distribution of on-axis sound radiation of far-field sound radiation of Fig. 9. (b) Wigner distribution, calculated with analytic signal.

2 TRANSIENT BEHAVIOR OF CROSSOVER FILTERS FOR COINCIDENT DRIVERS

In a previous publication [1, sec. 1.6] the application of the Wigner distribution technique to the evaluation of the transient behavior of a crossover filter was briefly discussed. The filter considered there was a third-order Butterworth crossover filter as described by Linkwitz [16]. With this filter phase reversal of the individual drivers makes no difference in the amplitude of the combined frequency response. However, phase reversal yields quite different impulse responses and transient behaviors, but these differences cannot be interpreted easily. What happens can be seen more clearly in the Wigner distributions of the two impulse responses, as shown in [1].

The use of the Wigner distribution technique for the optimization of the loudspeaker crossover is schematically illustrated in Fig. 19. Fig. 19(a) shows the contour plots of the Wigner distribution of a low-frequency and a high-frequency driver mounted in the same baffle. The different positions of the acoustic centers are in-

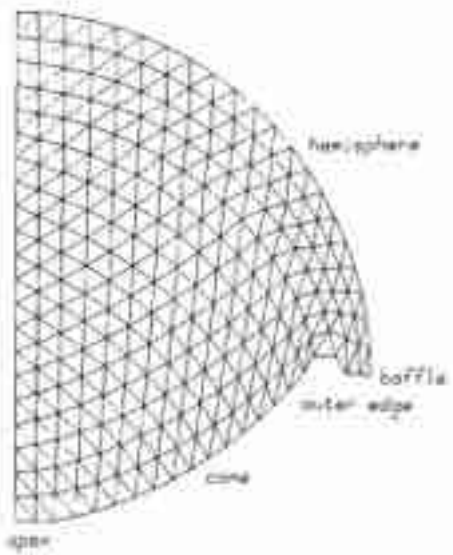

Fig. 11. Calculation mesh of concave cone-shaped radiator. Radius of concave curvature —150 mm; other dimensions same as those in Fig. 2.

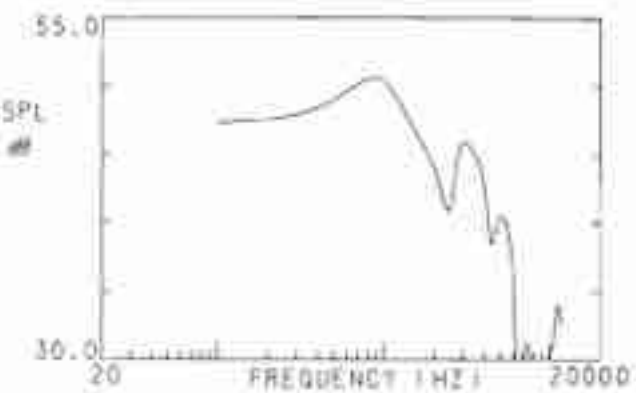

Fig. 12. Far-field sound pressure level of concave cone-shaped radiator with dimensions of Fig. 11.

dicated by dashed lines. This difference is not a defect in a loudspeaker, since the acoustic center of the loudspeaker depends on the location of both the rolloff frequencies and the rolloff slopes [1]. The optimization criterion of the combination of two loudspeakers is that its Wigner distribution should have the shape of the Wigner distribution of a band-pass filter, as shown in Fig. 19(c). The rolloffs are the low-frequency rolloff of the low-frequency driver and the high-frequency rolloff of the high-frequency driver. In this case the transducers have to be aligned with respect to time so that the mountain ridges in their individual Wigner distributions are in line. This is illustrated in Fig. 19(b). Also the crossovers have to be adjusted so that the ears of the individual transducers cancel each other in the

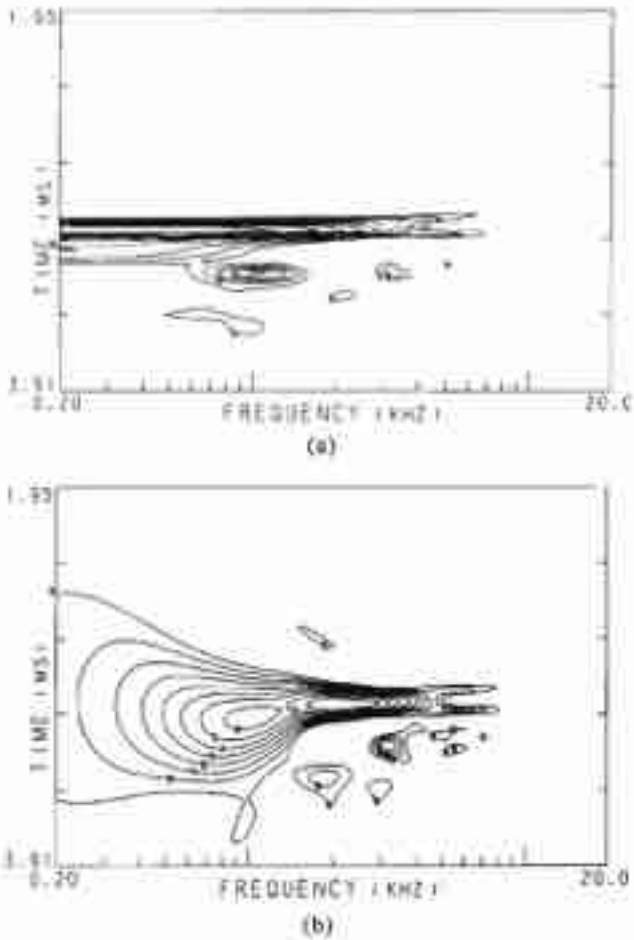

Fig. 13. (a) Wigner distribution of on-axis far-field sound radiation of Fig. 12. (b) Wigner distribution calculated with analytic signal.

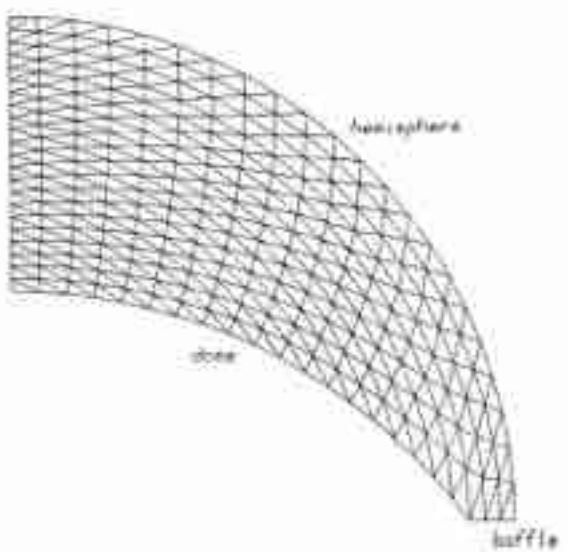

Fig. 14. Calculation mesh of dome-shaped radiator. Equivalent piston radius—30 mm; radius of hemisphere—33 mm; ratio of dome height to equivalent piston radius—0.5.

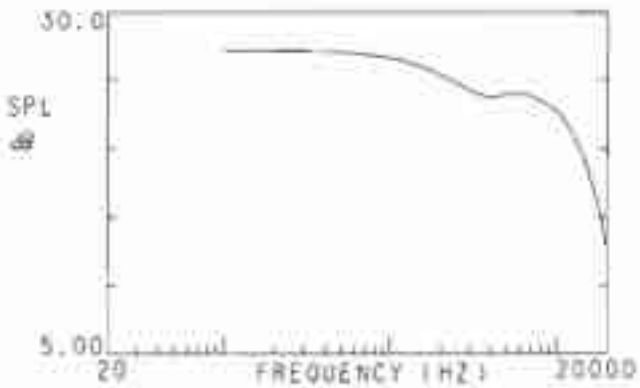

Fig. 15. Far-field sound pressure level of dome-shaped radiator with dimensions of Fig. 14.

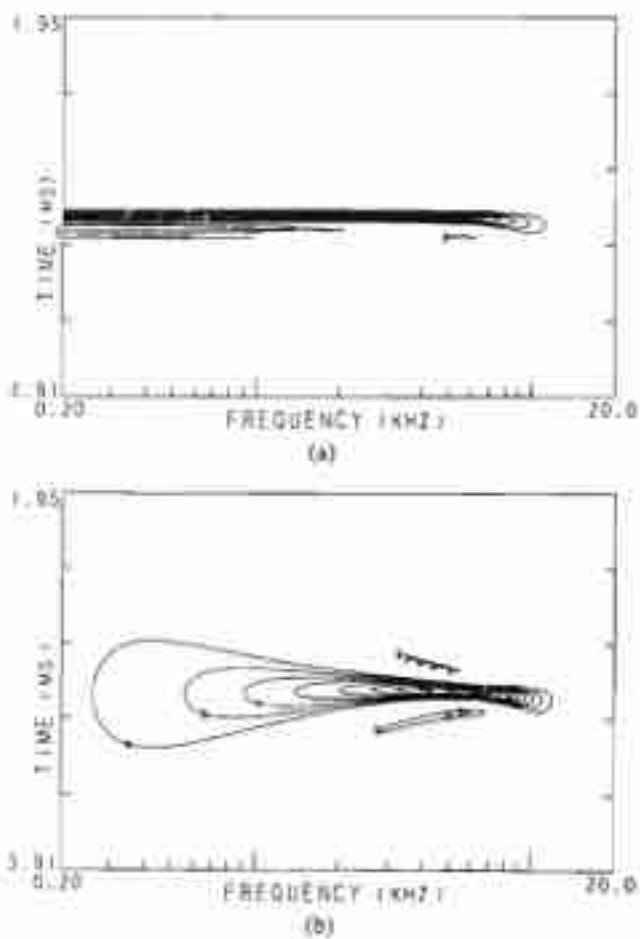

Fig. 16. (a) Wigner distribution of one-axis far-field sound radiation of Fig. 15. (b) Wigner distribution calculated with analytic signal.

crossover frequency region. This may be possible since the Wigner distribution of the sum of two transducers equals the sum of the Wigner distributions of the individual transducers plus an additional term, the cross-Wigner distribution of the two transducers [1, sec. 1.3], which yields the cancellations in the crossover region.

In this section we compare the transient behavior of several known crossover filters for coincident drivers. According to Linkwitz [16] the different types of

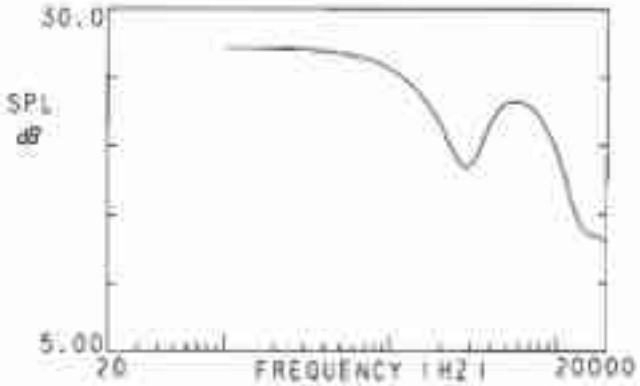

Fig. 17. Far-field sound pressure level of dome-shaped radiator of Fig. 14, but now with ratio of dome height to equivalent piston radius of 1.0.

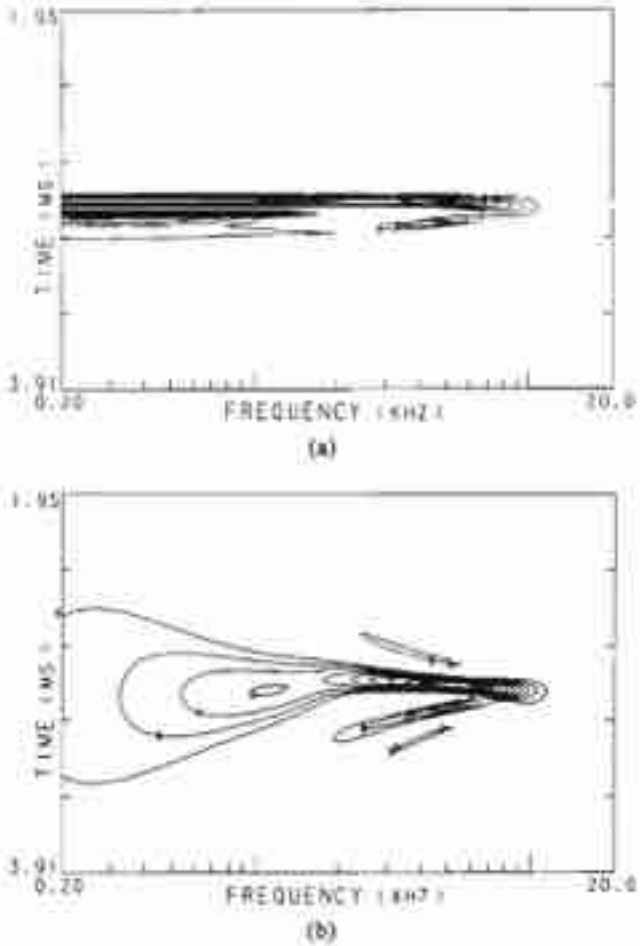

Fig. 18. (a) Wigner distribution of on-axis sound radiation of far-field sound radiation of Fig. 17. (b) Wigner distribution calculated with analytic signal.

crossover filters can be classified into three groups:

1) The constant-voltage crossover network, where the sum of the complex transfer functions of the low-frequency part and the high-frequency part is unity for all frequencies.

2) The all-pass crossover network, where only the magnitude of this sum is unity. Its amplitude response is thus unity at all frequencies, but its phase response is frequency dependent.

3) The compromise crossover network, where both the amplitude and the phase responses are frequency dependent.

Linkwitz compared the radiation patterns for these types of filters for noncoincident drivers at their crossover frequency region. For this purpose he used the following actual transfer functions.

1) For the constant-voltage network two third-order crossover filters with 12-dB-per-octave slopes as described by Small [17]:

$$F_l = \frac{1 + as_n}{1 + as_n + as_n^2 + s_n^3}, \tag{5a}$$

$$F_h = \frac{as_n^2 + s_n^3}{1 + as_n + as_n^2 + s_n^3}, \tag{5b}$$

where F_l and F_h are the low- and high-pass filter transfer functions, respectively; s_n denotes the normalized complex crossover frequency [Eq. (9)], and $a = 2 + \sqrt{3}$.

2) For the all-pass network the third-order Butterworth

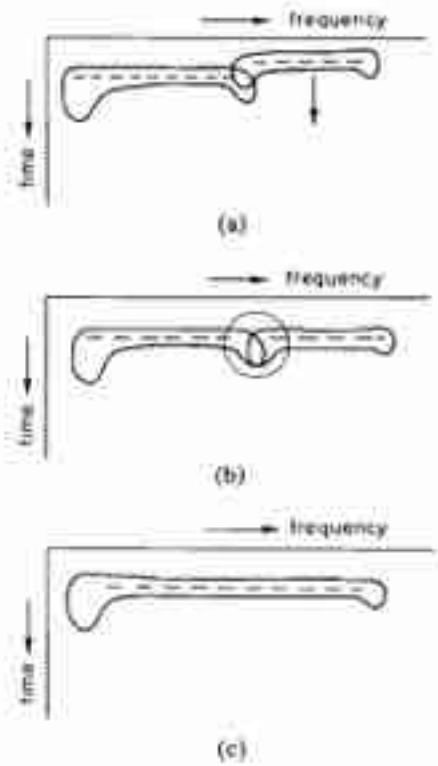

Fig. 19. (a) Contour plots of Wigner distributions of low- and high-frequency drivers mounted in same baffle. (b) Same contour plots, but with drivers aligned with respect to time. (c) Wigner distribution of combination of low- and high-frequency drivers of (a) with optimum crossover.

low- and high-pass filter functions:

$$F_l = \frac{1}{1 + 2s_n + 2s_n^2 + s_n^3} \tag{6a}$$

$$F_h = \frac{s_n^3}{1 + 2s_n + 2s_n^2 + s_n^3} \tag{6b}$$

3) For the compromise network the second-order Butterworth low- and high-pass filter functions:

$$F_l = \frac{1}{1 + \sqrt{2}s_n + s_n^2} \tag{7a}$$

$$F_h = \frac{s_n^2}{1 + \sqrt{2}s_n + s_n^2} \tag{7b}$$

To compare the crossovers of these filter functions we will use the band-pass Butterworth filter $H_{bp}(s)$ as a reference. The reason for using a band-pass filter function is that we cannot calculate a discrete Wigner distribution of a high-pass filter due to aliasing. Furthermore a loudspeaker acts as a band-pass filter. The filter $H_{bp}(s)$ has a rolloff of order 2 at 500 Hz and a rolloff of order 10 at 4000 Hz. The contour plot of the Wigner distribution of this filter is shown in Fig. 20. (The length of the ear at 4 kHz, that is, the ringing of the tenth-order rolloff, is not greater than the ear of the second-order rolloff at 500 Hz because the length of an ear is directly proportional to the rolloff slope and inversely proportional to the frequency [1].)

The total crossover function of the combined networks can be described with the equation

$$H_{co}(s) = F_l(s_n)\, H_{bp}(s) \pm F_h(s_n)\, H_{bp}(s) \tag{8}$$

where s is the complex frequency variable, $\pm$ denotes in- and out-of-phase connection, and s_n is the normalized complex frequency variable,

$$s_n = \frac{s}{2\pi f_c} \tag{9}$$

f_c being the crossover frequency. The crossover frequency in the examples is 2500 Hz.

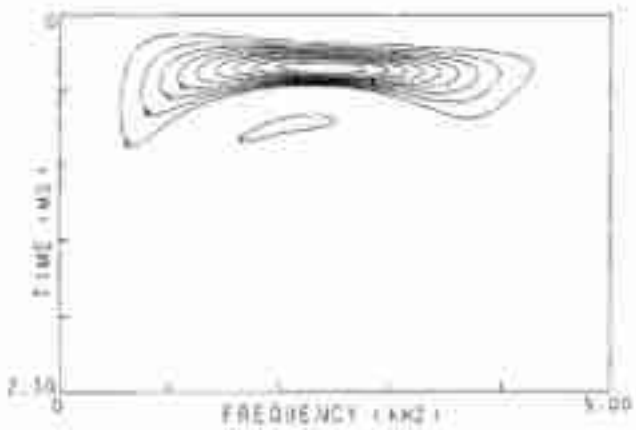

Fig. 20. Wigner distribution of band-pass filter $H_{bp}(s)$.

The "ideal" crossover function is given by

$$H_{co}(s) = H_{bp}(s) \quad \text{or} \quad F_l(s_n) + F_h(s_n) = 1 \tag{10}$$

and its transient behavior is shown in Fig. 20.

Such an "ideal" function (for coincident drivers) is the in-phase connection of the constant-voltage filter of Eq. (5), and its Wigner distribution is that of Fig. 20, as would be expected. The natural application of this crossover filter is the in-phase connection, but Fig. 21 also shows the Wigner distribution of the out-of-phase connection. This transient response is only slightly different from that of Fig. 20, mainly because of small differences in the amplitude response.

The next example is the all-pass crossover network [Eq. (6)]. Fig. 22(a) shows the contour plot of the Wigner distribution of the out-of-phase connection. The differences between Fig. 22(a) and Fig. 20 are small so that the transient behavior of this crossover is almost "ideal." The in-phase connection of this all-pass crossover is shown in Fig. 22(b). This connection has more influence on the transient behavior, as can be seen from the contraction in the time direction at the crossover frequency. Thus the out-of-phase connection of this all-pass filter has the least transient distortion.

However, if the delay of the low-frequency driver is relatively large (crossover frequency at low frequencies or high rolloff slope), then the proper alignment with respect to time will not be achieved. This topic is not discussed here, but can be found in [18], for example. Furthermore our preliminary experiments indicate that the audible effects of such an additional all-pass filter is very small for practical loudspeakers, which also has been reported elsewhere [19], [20].

The next example is the compromise network of Eq. (7). Fig. 23(a) shows the contour plot of the Wigner distribution of the out-of-phase connection. The transient response is almost equal to that shown in Fig. 20. The differences are due to different amplitude responses, but this transient response is without problems. However, this is not the case with the in-phase connection, as shown in Fig. 23(b). Here we find large distortions in the transient behavior of the combination. The composition of this response can be understood from Fig. 19(b): the ears at the crossover frequency have to cancel each other, which occurs correctly with the out-of-phase connection. With the in-phase connection of Fig. 23(b) we get a cancellation at earlier times and an amplification of the ears in the crossover region, since the sign of the cross-Wigner distribution is reversed. [There is no amplification of the ear at the low-frequency end, since the ear in Fig. 23(b) is emphasized due to different contour heights in Figs. 23(a) and (b).] It will be clear that with this compromise network only the out-of-phase connection should be considered.

The last example of this section is the optimum

crossover function for noncoincident drivers as proposed by Linkwitz [16]. It is the cascade of two identical Butterworth filters and acts like an all-pass filter. Cascading two identical first-order Butterworth filters yields the second-order low- and high-pass filter functions:

$$F_l = \frac{1}{(1 + s_n)^2} \tag{11a}$$

$$F_h = \frac{s_n^2}{(1 + s_n)^2}. \tag{11b}$$

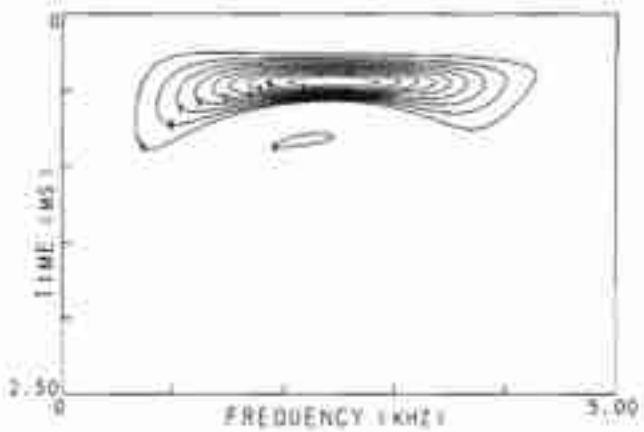

Fig. 21. Wigner distribution of out-of-phase connection of constant-voltage crossover filter of Eq. (5).

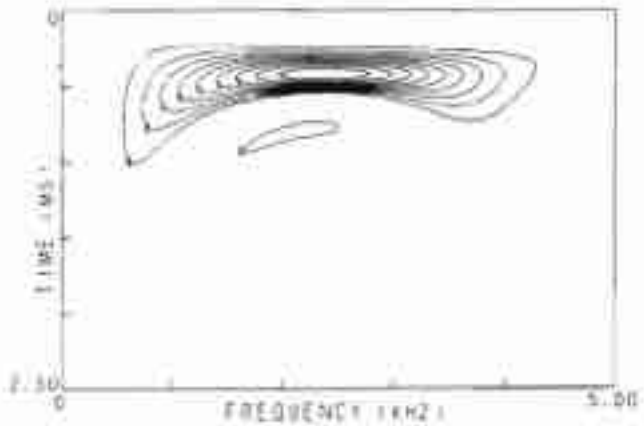

(a)

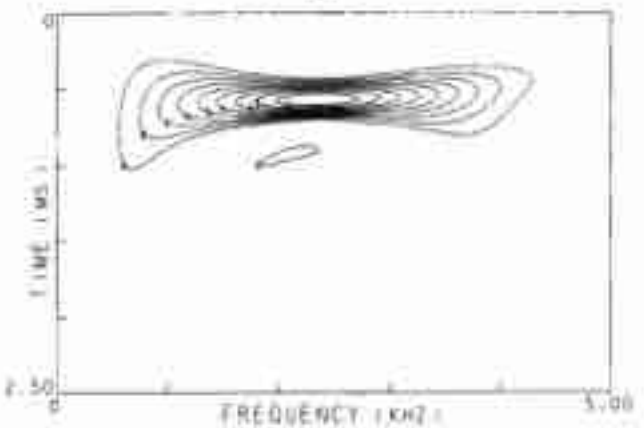

(b)

Fig. 22. (a) Wigner distribution of out-of-phase connection of all-pass crossover filter of Eq. (6). (b) Wigner distribution of in-phase connectionof all-pass crossover filter of Eq. (6).

Fig. 24 shows the contour plots of the Wigner distributions of the out-of-phase and the in-phase connections for coincident drivers. Again the in-phase connection of Fig. 24(b) should be rejected. The out-of-phase connection of Fig. 24(a) closely resembles the ideal crossover of Fig. 20, as would be expected. It can be concluded that none of the filter functions gives a substantial transient distortion for coincident drivers if the proper phasing is used.

3 DIRECTIONAL TRANSIENT BEHAVIOR OF CROSSOVER FILTERS FOR NONCOINCIDENT DRIVERS

As shown by Linkwitz [16] for steady-state signals, the optimum crossover for coincident drivers is not necessarily the optimum crossover for noncoincident drivers. This is caused by a possible tilting of the radiation pattern in the plane of the two driver axes in the case of noncoincident drivers. To avoid this tilting one has to take care that the on-axis phase difference between the two drivers vanishes in the crossover frequency region. To examine the transient behavior of noncoincident drivers, one can calculate the Wigner distributions at different directions θ in the plane of the two driver axes. The geometry of the two non-

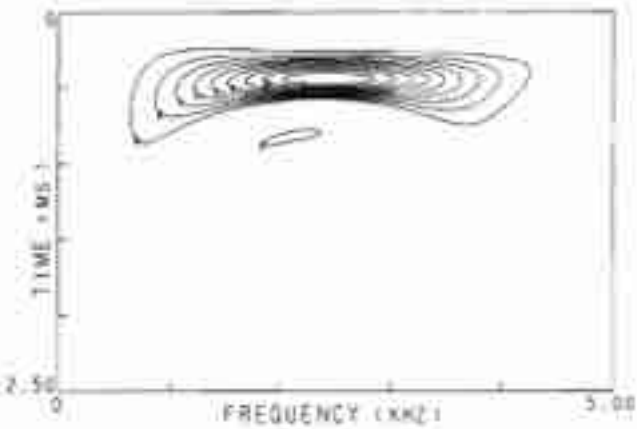

(a)

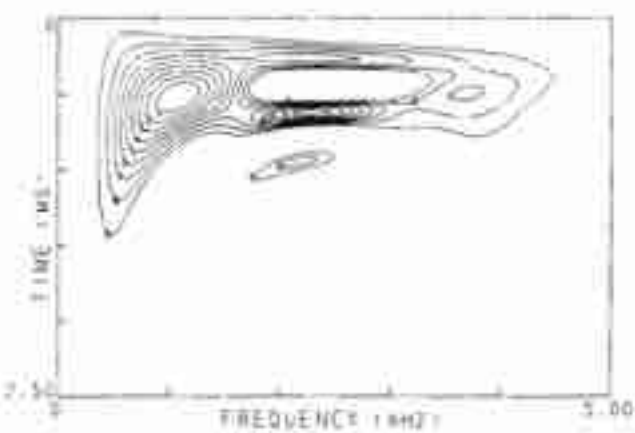

(b)

Fig. 23. (a) Wigner distribution of out-of-phase connection of compromise crossover filter of Eq. (7). (b) Wigner distribution of in-phase connection of compromise crossover filter of Eq. (7).

coincident drivers is shown schematically in Fig. 25. However, since the evaluation of many Wigner distributions can be cumbersome, we will use another representation in this section. This representation is based on the knowledge that the directional behavior of a crossover is most critical at the crossover frequency, where the amplitudes of the individual drivers measured on axis are the same. The representation is not the normal time–frequency Wigner distribution, but a time–direction distribution. It is composed of the cross sections in the time direction at a single frequency, such as the crossover frequency, of the Wigner distributions of the impulse responses in the different directions. This can be calculated efficiently if the Wigner distributions are calculated from frequency domain data. In that case we can calculate the cross sections at a single frequency directly [1] without the need to calculate the whole Wigner distribution for each impulse response.

With this directional representation of the transient behavior we will compare the different crossover functions that were described in the previous section. The difference with these examples is that the drivers are noncoincident. The actual spacing between the drivers is 100 mm, and the crossover frequency is again 2500 Hz.

The directional representation of the constant-voltage crossover of Eq. (5) is shown in Fig. 26 for the in-phase and the out-of-phase connections. Clearly visible is the tilting of the radiation pattern. In the case of an ideal omnidirectional radiator the cross section in the time direction at every angle would be the same. Then the contour plot would only contain straight lines perpendicular to the time axis. In the case of an ideal directional radiator the contour plot would be symmetrically located around the 0° cross section. The main lobe and side lobes are represented by separate contributions or islands in the contour plot.

The in-phase connection of the constant-voltage filter

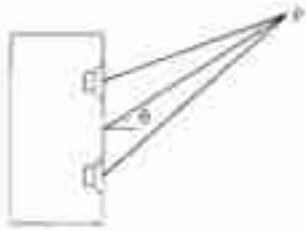

Fig. 25. Geometry of two noncoincident drivers. Distance from the baffle to field point P is much larger than spacing between drivers.

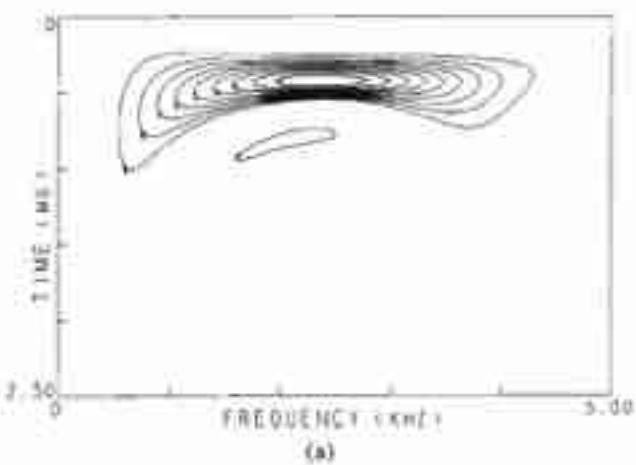

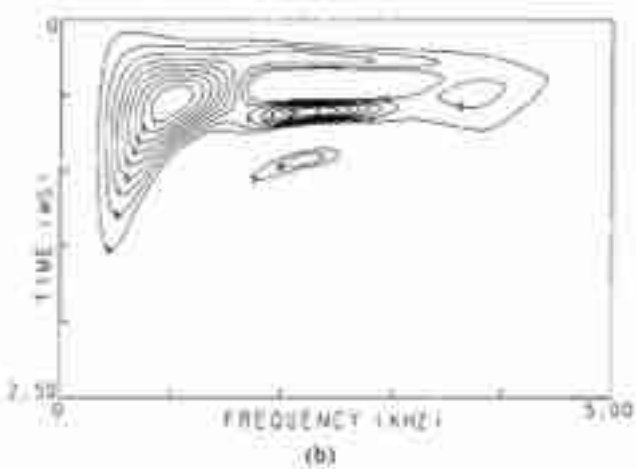

Fig. 24. (a) Wigner distribution of out-of-phase connection of second-order Linkwitz–Riley crossover filter of Eq. (11). (b) Wigner distribution of in-phase connection of second-order Linkwitz–Riley crossover filter of Eq. (11).

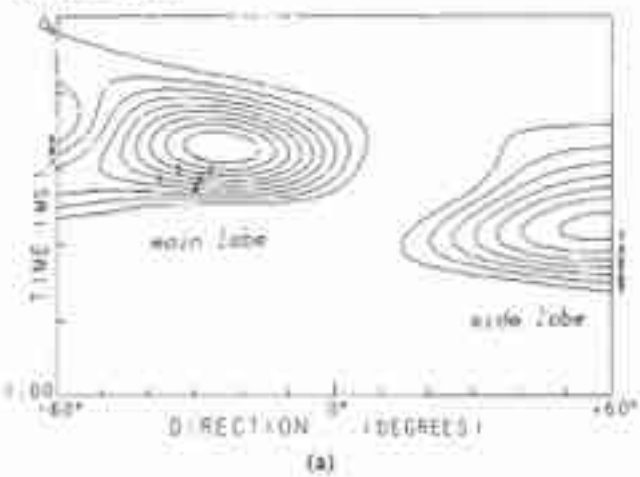

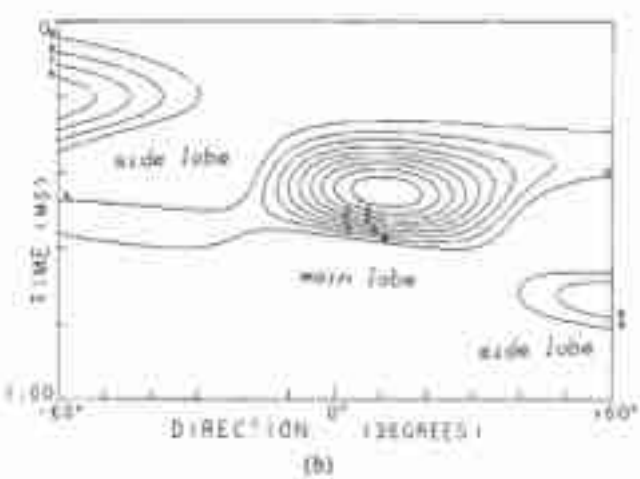

Fig. 26. Directional Wigner distribution representation of constant-voltage crossover filter of Eq. (5) at crossover frequency (2500 Hz). (a) In-phase connection. (b) Out-of-phase connection.

[Fig. 26(a)] shows the main lobe at about $-25°$ and a side lobe at about $+60°$, which is shifted relative to the main lobe in the time direction. The out-of-phase connection [Fig. 26(b)] shows the main lobe at $+10°$. This connection has a smaller amount of radiation pattern tilting than the in-phase connection, but both connections are not well suited for noncoincident drivers.

The directional representation of the all-pass crossover of Eq. (6) is shown in Fig. 27 for the out-of-phase and the in-phase connections. Fig. 27(a) shows the main lobe at about $-18°$ and a side lobe at about $+60°$, which is shifted in the time direction. The reverse or in-phase connection shown in Fig. 27(b) has the main lobe at about $+18°$ and a side lobe at about $-60°$, which precedes the main lobe in time. With this crossover, too, neither of the two connections are well suited for noncoincident drivers.

The directional behavior of the compromise network of Eq. (7) is shown in Fig. 28 for the out-of-phase and the in-phase connections. The plot for the in-phase connection shows two lobes at about $+38°$ and $-38°$, which are shifted in time relative to each other. It will be clear that this phasing should be rejected, but this could already be concluded from its amplitude characteristic, which shows a large dip at the crossover frequency.

The out-of-phase connection is a much better choice, as can be seen in Fig. 28(a). Its transient response of the main lobe is symmetrically located around the 0° cross section. The two side lobes, however, are shifted in the time direction. Therefore only the main lobe is aligned with respect to time with the low- and high-frequency parts of the total transient response on axis. [See the time–frequency Wigner distribution as shown in Fig. 23(a)]. This will be clear if we realize that the cross section at 2500 Hz of Fig. 23(a) equals the cross section at 0° in Fig. 28(a). Thus with this crossover we are able to maintain its time alignment within a limited symmetrically located beam width in the plane of the two driver axes.

The last example in this section is the optimum crossover network for noncoincident drivers as proposed by Linkwitz [16]. This Linkwitz–Riley filter is the cascade of two identical Butterworth filters. Thus the order of the filter is always even. These filters resemble the behavior of even Butterworth filters, for example, the second-order Linkwitz–Riley filter, which can be described by Eq. (11), has a similar behavior as the second-order Butterworth filter shown in Figs. 23 and 28. However, the Linkwitz–Riley filters have no peak in the on-axis amplitude characteristic at the crossover

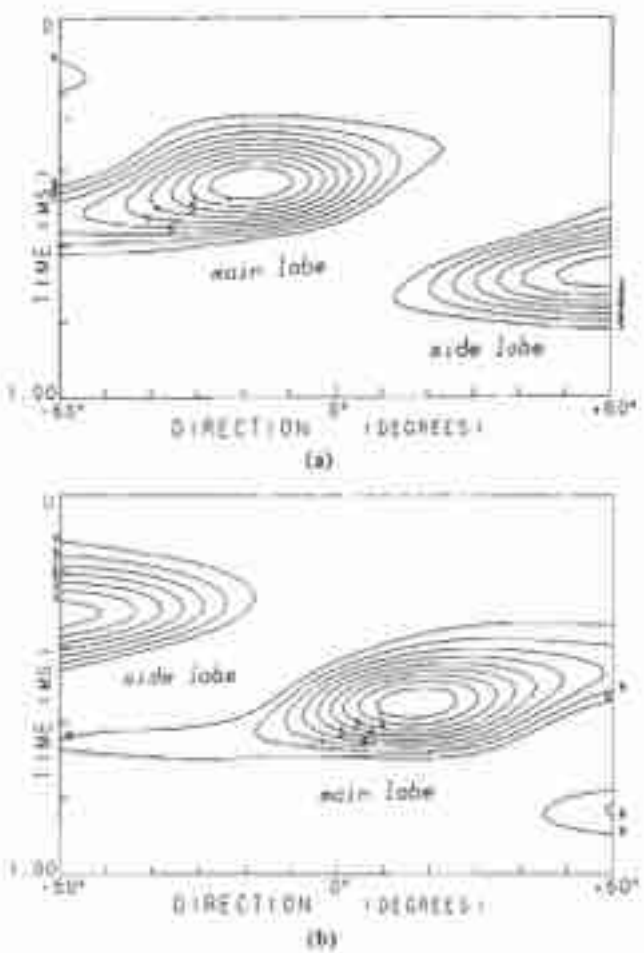

Fig. 27. Directional Wigner distribution representation of all-pass crossover filter of Eq. (6) at crossover frequency (2500 Hz). (a) Out-of-phase connection. (b) In-phase connection.

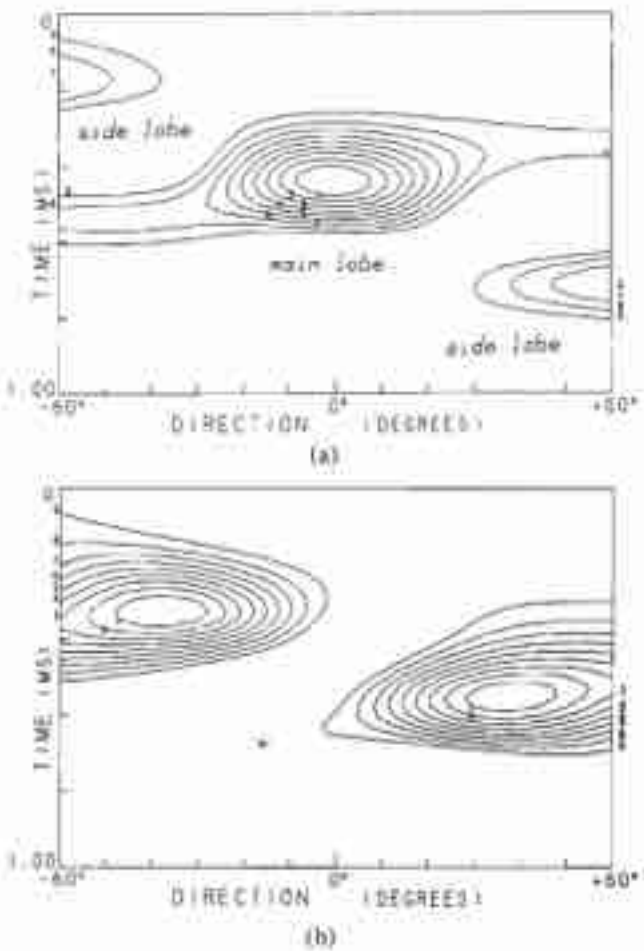

Fig. 28. Directional Wigner distribution representation of compromise crossover filter of Eq. (7) at crossover frequency (2500 Hz). (a) Out-of-phase connection. (b) In-phase connection.

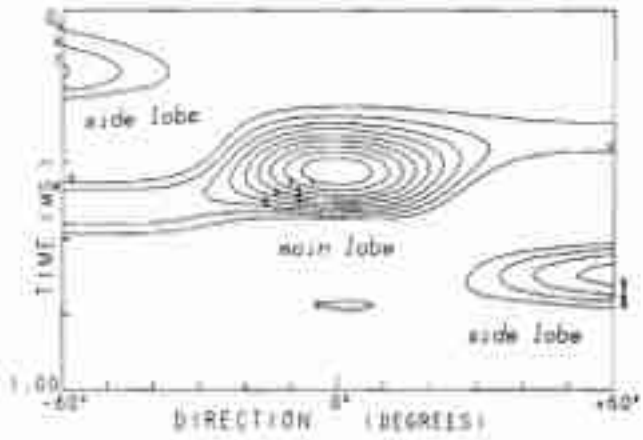

Fig. 29. Directional Wigner distribution representation of out-of-phase connection of second-order Linkwitz–Riley crossover filter at crossover frequency (2500 Hz).

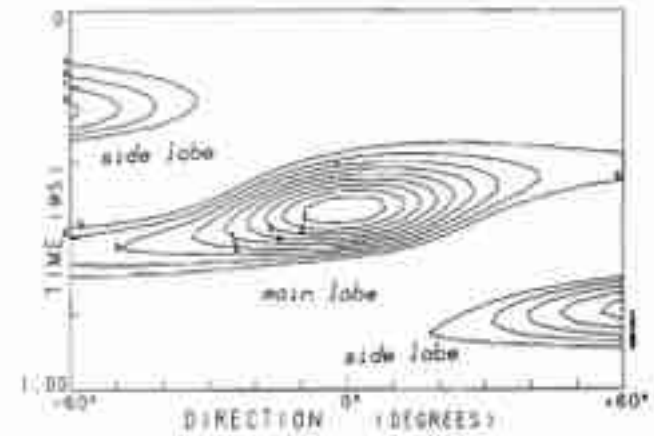

Fig. 30. Directional Wigner distribution representation of in-phase connection of fourth-order Linkwitz–Riley crossover filter at crossover frequency (2500 Hz).

frequency. In this case, too, one of the phasings should be rejected: the in-phase connection for the second-order and the out-of-phase connection for the fourth-order Linkwitz–Riley filters. Both have two side lobes, which are shifted in the time direction, comparable to those shown in Fig. 28(b).

The out-of-phase connection of the second-order Linkwitz–Riley crossover is shown in Fig. 29. This directional transient response resembles that of the second-order Butterworth crossover shown in Fig. 28(a), and the same discussion holds. The in-phase connection of the fourth-order Linkwitz–Riley filter, as shown in Fig. 30, maintains its time alignment over approximately the same beam width. This will be clear if we compare the Wigner distributions at different angles for both crossovers. The Wigner distributions of the second-order Linkwitz–Riley filter at different angles are shown in Fig. 31 for the angles +30°, 0°, and −30°. The corresponding distributions for the fourth-order Linkwitz–Riley filter are shown in Fig. 32. It may be concluded that for the transient response, too, the Linkwitz–Riley filters are the optimum choice for noncoincident drivers, provided that the proper phasing is used. However, from the directional representation of the transient response it is clear that the proper alignment with respect to time is only maintained within a limited beam width in the plane of the two driver axes. This beam width can be increased if the spacing between the drivers is decreased.

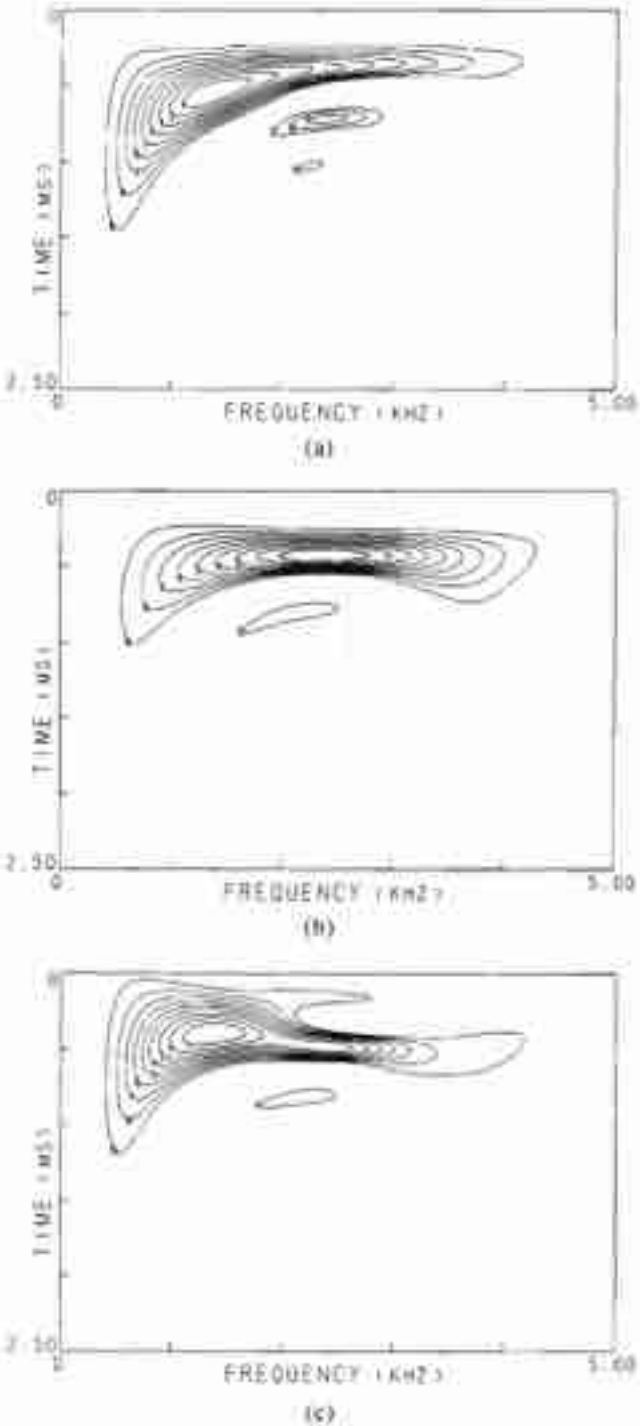

Fig. 31. Wigner distribution of second-order Linkwitz–Riley filter of Fig. 29. (a) At +30°. (b) At 0°. (c) At −30°.

4 CONCLUSIONS

In this paper we have been concerned with two topics associated with the transient behavior of loudspeakers and loudspeaker systems. First we discussed the influence of the geometry of a radiator on the transient behavior of the on-axis sound radiation. We have shown

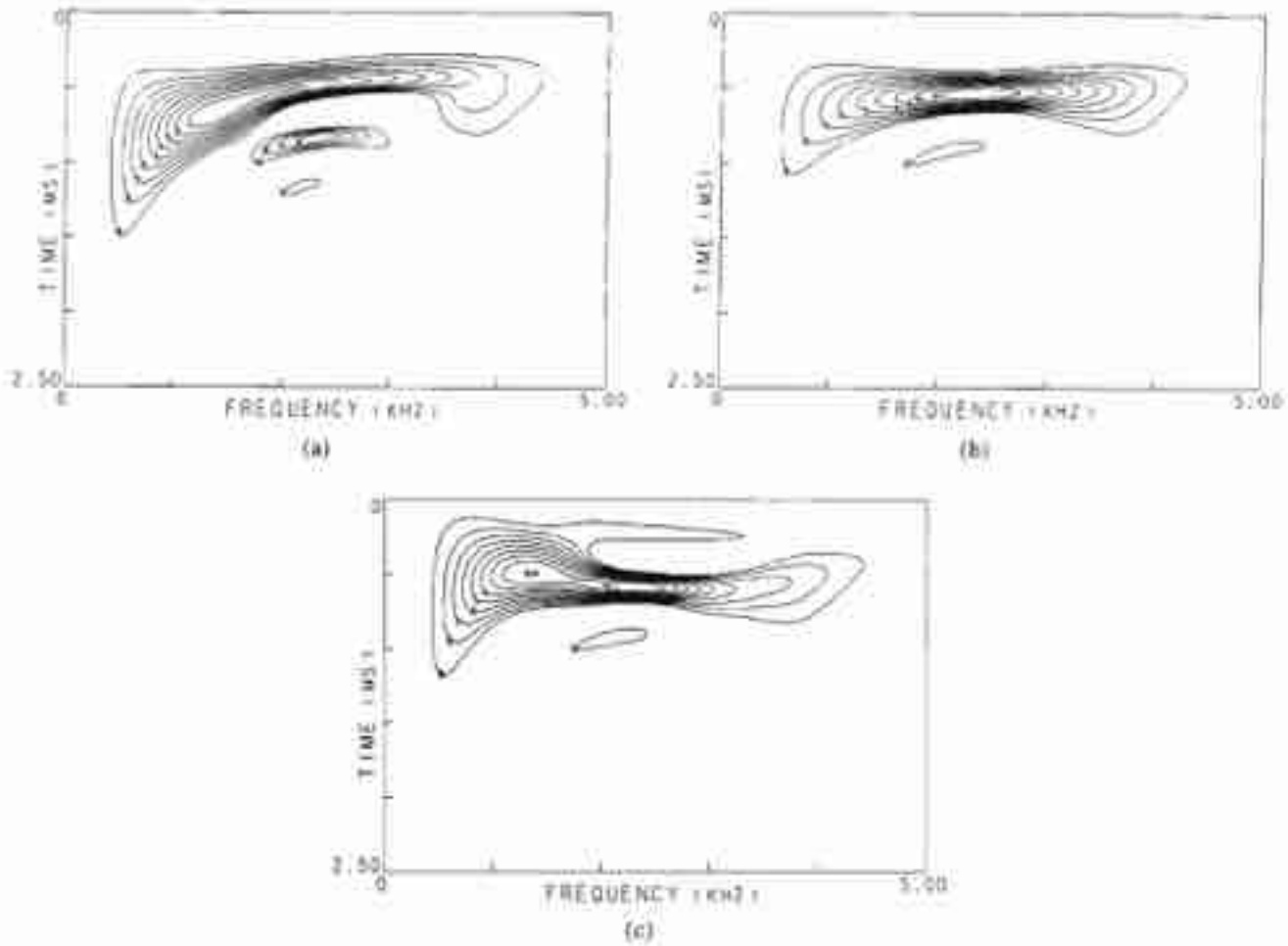

Fig. 32. Wigner distribution of fourth-order Linkwitz–Riley filter of Fig. 30. (a) At +30°. (b) At 0°. (c) At −30°.

that for a rigid axisymmetric radiator the plane piston has the best transient behavior. The transient behavior of dome-shaped radiators is also reasonable, especially if the ratio of dome height to equivalent piston radius is less than unity. The cone-shaped radiator, however, shows a considerable transient distortion in the form of a widening or spreading of the response in the time direction at middle and lower frequencies. This distortion is found with both the conical cone-shaped radiator and the bent cone-shaped radiator, like the convex and the concave cone. The effect of the transient distortion can be reduced by fitting a dust cap. If the size of the dust cap is increased, thus decreasing the cone cavity volume, the reduction of the transient distortion will be more pronounced.

The other topic of this paper was the transient behavior of some known crossover filters for coincident and noncoincident drivers. The types of crossover filter functions were the constant-voltage, the all-pass and the compromise filter functions. We also discussed an optimum choice of the crossover functions for noncoincident drivers, the all-pass Linkwitz–Riley filter functions. It was concluded that none of these filter functions gives rise to any substantial transient distortion with coincident drivers, provided that the proper phasing is used. In the case of noncoincident drivers it was concluded that, for the transient response, too, the Linkwitz–Riley filters are the optimum choice, provided that the proper phasing is used. However, for all these filter functions the proper alignment with respect to time is maintained only on a limited beam width in the plane of the two drivers' axes. This beam width can be increased if the spacing between the drivers is decreased.

5 REFERENCES

[1] C. P. Janse and A. J. M. Kaizer, "Time–Frequency Distributions of Loudspeakers: The Application of the Wigner Distribution," *J. Audio Eng. Soc.*, vol. 31, pp. 198–223 (1983 Apr.).

[2] R. C. Heyser, "Loudspeaker Phase Characteristics and Time-Delay Distortion, Pt. I," *J. Audio Eng. Soc.*, vol. 17, p. 30 (1969 Jan.).

[3] L. L. Beranek, *Acoustics* (McGraw-Hill, New York, 1954).

[4] S. Oie, R. Takeuchi, and T. Shindo, "Sound Radiation from a Concave Radiator in an Infinite Baffle," *Acustica*, vol. 46, pp. 268–275 (1980).

[5] H. Suzuki and J. Tichy, "Sound Radiation from Convex and Concave Domes in an Infinite Baffle," *J. Acoust. Soc. Am.*, vol. 69, pp. 41–49 (1981 Jan.).

[6] H. Suzuki and J. Tichy, "Sound Radiation from an Axisymmetric Radiator in an Infinite Baffle," *J. Acoust. Soc. Japan* (E), vol. 3, pp. 167–172 (1982).

[7] P. M. Morse and K. U. Ingard, *Theoretical Acoustics* (McGraw-Hill, New York, 1968).

[8] M. C. Junger and D. Feit, *Sound, Structures, and Their Interaction* (MIT Press, Cambridge, 1972).

[9] J. W. Strutt, *Lord Rayleigh, The Theory of Sound*, 2nd ed. (Macmillan, London, 1894).

[10] J. A. Riedel, "Berekening van het stralingsveld van luidsprekers met behulp van integraal vergelijkingen," M.Sc. Thesis, Eindhoven University of Technology (1981).

[11] J. B. Swenker, "Berekening van het stralingsveld van luidsprekers met behulp van de eindige elementen," M.Sc. Thesis, Eindhoven University of Technology (1982).

[12] R. C. Heyser, "Determination of Loudspeaker Signal Arrival Times, Pt. II," *J. Audio Eng. Soc.*, vol. 19, pp. 829–834 (1971 Nov.).

[13] F. J. M. Frankort, "Vibration and Sound Radiation of Loudspeaker Cones," Philips Res. Repts., Suppl., no. 2 (1975).

[14] T. Shindo, N. Kyono, and O. Yashima, "The Role of the Dust Cap in the Cone-Type Loudspeaker," presented at the 63rd Convention of the Audio Engineering Society, *J. Audio Eng. Soc. (Abstracts)*, vol. 27, p. 600 (1979 July/Aug.), preprint 1469.

[15] J. M. Kates, "Radiation from a Dome," *J. Audio Eng. Soc.*, vol. 24, pp. 735–737 (1976 Nov.).

[16] S. H. Linkwitz, "Active Crossover Networks for Noncoincident Drivers," *J. Audio Eng. Soc.*, vol. 24, pp. 2–8 (1976 Jan./Feb.); "Passive Crossover Networks for Noncoincident Drivers," *ibid. (Engineering Reports)*, vol. 26, pp. 149–150 (1978 Mar.).

[17] R. H. Small, "Constant-Voltage Crossover Network Design," *J. Audio Eng. Soc.*, vol. 19, pp. 12–19 (1971 Jan.).

[18] S. P. Lipshitz and J. Vanderkooy, "A Family of Linear-Phase Crossover Networks of High Slope Derived by Time Delay," *J. Audio Eng. Soc.*, vol. 31, pp. 2–20 (1983 Jan./Feb.).

[19] J. Blauert and P. Laws, "Group Delay Distortions in Electroacoustical Systems," *J. Acoust. Soc. Am.*, vol. 63, pp. 1478–1483 (1978 May).

[20] S. P. Lipshitz, M. Pocock, and J. Vanderkooy, "On the Audibility of Midrange Phase Distortion in Audio Systems," *J. Audio Eng. Soc.*, vol. 30, pp. 580–595 (1982 Sept.).

6. Analysis of the nonlinear distortion at low frequencies[1]

The simplified model of the electrodynamic loudspeaker, the lumped parameter model, described in chapter 2 assumes the loudspeaker to be a linear system. A loudspeaker, however, shows small nonlinearities that produce typical distortion phenomena. Possible nonlinearities may be found in many parts of the loudspeaker and it is convenient to refer to the lumped parameter model if the nonlinearities are to be localized. A list of possible nonlinearities is given below.

A. Nonlinearities in the motor part (magnet system/voice coil).

A1 The force on the voice coil in the case of a constant current drive depends on the position of the coil, owing to the fact that the electromagnetic coupling factor $\int B.dl$ is a function of the voice coil excursion. A typical $\int B.dl$ vs. displacement curve is shown in Fig. 6.1.

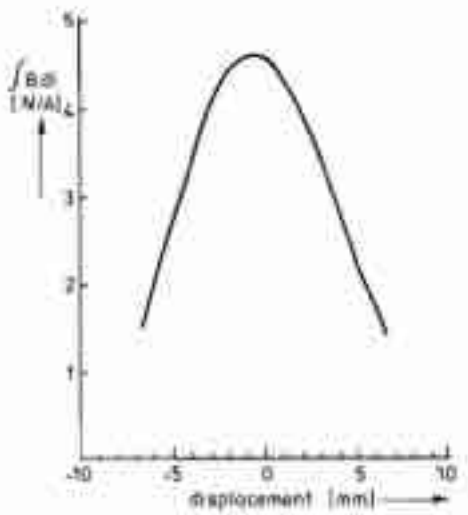

Fig. 6.1: Typical force vs. displacement curve of an actual loudspeaker. The air gap length is 5 mm and the voice coil height is 10 mm.

A2 The self-inductance of the voice coil depends on its position, because the voice coil protrudes from the central pole. This yields a reluctance force proportional to the squared current [41]

$$F_x = \tfrac{1}{2} i^2 \frac{dL(x)}{dx}, \qquad 6.1$$

where x is the voice coil excursion.

A3 The voltage across the self-inductance is not only proportional to the time derivative of the current but shows the relation:

$$U = L(x)\frac{di}{dt} + i\frac{dL(x)}{dx}\frac{dx}{dt}. \qquad 6.2$$

A4 The operating point of the permanent magnet is influenced by the voice coil current.

A5 Eddy currents occur which yield a nonlinear damping force.

B. Nonlinearities in the mechanical part.

B1 The force vs. displacement curves of the loudspeaker spider and outer rim are not straight lines and show hysteresis. A typical force vs. displacement curve of a spider is shown in Fig. 6.2.

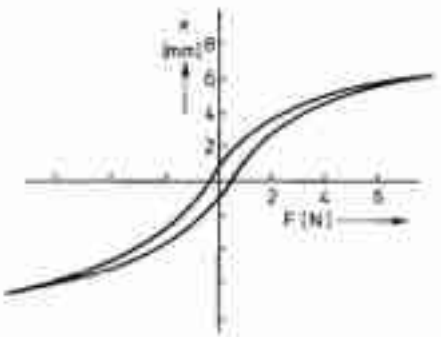

Fig. 6.2: Typical force vs. displacement curve of a spider.

B2 The excursion capability of the voice coil is limited (mechanical clipping). This nonlinearity only occurs at extreme drive levels.

B3 Sub-harmonics are generated at the loudspeaker cone [35]. This distortion occurs only at extreme drive levels.

C. Nonlinearities in the sound radiation.

C1 Adiabatic distortion: the volume compression is not proportional to the pressure but follows the relation:

$$p.V^{\gamma} = \text{constant}. \qquad 6.3$$

C2 Doppler distortion: a low-frequency excursion of the diaphragm yields a varying Doppler shift of a higher frequency tone. It has been reported that this distortion can be neglected in a practical situation [36].

It will be clear that the loudspeaker exhibits many types of nonlinearity. Most of these nonlinearities are relatively small because the total harmonic distortion is usually less than a few percents even at high drive

[1] The numerical analysis of the nonlinear distortion of a voltage-driven electrodynamic loudspeaker, as described in this chapter, is part of a M.Sc. thesis by G.H. van Leeuwen [42]. The measurements of the nonlinear responses and of the nonlinear component characteristics were carried out by W.D.A.M. van Gijsel.

levels and it shows a maximum at the lower frequencies where the excursion of the voice coil is maximum. If we restrict our analysis to the lower frequency range, around the loudspeaker's fundamental resonance frequency, then we have only to take into account those nonlinearities that depend closely on the voice coil excursion. In that case the most prominent nonlinearities are:

- The force factor $\int B.dl$, which depends on the voice coil excursion (A1).
- The electric self-inductance, which depends on the voice coil excursion (A3).
- The nonlinear suspension stiffness (B1).

The vibration of a loudspeaker diaphragm at low frequencies resembles that of a mass-spring system and the governing coupled differential equations are given by

$$E = R_E i + \frac{d(L_E i)}{dt} + Bl\,\dot{x}, \qquad 6.4$$

$$Bl\,i = m\ddot{x} + R_m\dot{x} + kx, \qquad 6.5$$

where x is the voice coil excursion.
The nonlinear differential equation that describes the nonlinear vibration can be derived if we approximate Bl, k and L_E by a truncated power series:

$$Bl = Bl_0 + b_1x + b_2x^2, \qquad 6.6$$

$$k = k_0 + k_1x + k_2x^2, \qquad 6.7$$

$$L_E = L_{E_0} + l_1x + l_2x^2. \qquad 6.8$$

In the power series 6.8 the frequency dependence of the self-inductance has been ignored. After insertion of 6.6, 6.7 and 6.8 into 6.4 and 6.5 and elimination of i, one obtains the following differential equation for the voice coil excursion:

$$\begin{aligned}&\alpha x + \beta\dot{x} + \gamma\ddot{x} + \delta\dot{\ddot{x}} + \\ &aE_g x + bx^2 + cx\dot{x} + dx\ddot{x} + ex\dot{\ddot{x}} + f\dot{x}^2 + g\dot{x}\ddot{x} \\ &+ AE_g x^2 + Bx^3 + Cx^2\dot{x} + Dx^2\ddot{x} + Ex^2\dot{\ddot{x}} + \\ &F\dot{x}\ddot{x}^2 + Gx\dot{x}\ddot{x} = E_g,\end{aligned} \qquad 6.9$$

where the terms with orders higher than three have been discarded. The parameters in this equation are listed in Appendix C.

6.1 Solving the nonlinear differential equation.

The nonlinear differential equation that describes the vibration of the loudspeaker can be solved by means of numerical methods. Two of these methods are described below.

Series expansion of the solution.
We assume the voltage E to vary sinusoidally according to $E_0\cos(\omega t)$ and the voice coil excursion to satisfy the series expansion

$$\begin{aligned}x = {} & B_0 + A_1\sin(\omega t) + A_2\sin(2\omega t) + \\ & A_3\sin(3\omega t)\ldots \\ & + B_1\cos(\omega t) + B_2\cos(2\omega t) + B_3\cos(3\omega t)\ldots\end{aligned} \qquad 6.10$$

The expansion is truncated after the k-th term and substituted in the differential equation. The resultant equation must be satisfied for any t so that the factors of $\sin(n\omega t)$ and $\cos(n\omega t)$ vanish. This yields a set of $2k$ nonlinear equations with $2k$ unknowns and a dependent equation that determines B_0. This set of nonlinear equations can be solved numerically. The method, however, is rather cumbersome, because we have to rewrite the whole set of nonlinear equations if another nonlinear effect is taken into account.

Direct integration.
Another method that can be used to solve the nonlinear differential equation is direct integration. The differential equation is written as a set of first order differential equations that can be integrated numerically [23]. The excitation is a sinusoidal voltage starting at $t = 0$ and the integration is terminated if the response is stationary, i.e. the difference between the solutions of two successive cycles is minimal. The higher harmonics can be found by harmonic analysis.

However, both methods are rather cumbersome if, for example, a difference frequency distortion component has to be determined. More powerful analytical techniques also are available:
- the Volterra series expansion of the response [37,38].
- the modelling of the system nonlinearities with a piecewise-linear approximation [39].

The main features of these two methods are:
- the Volterra series expansion has to be truncated in a numerical analysis after the n-th term, so that it describes the nonlinear response of the system up to the n-th order term.
- the Volterra series is only suited for small nonlinearities and a limited input signal, to guarantee the Volterra series to converge.
- the piecewise linear modelling approximates a nonlinear component characteristic by a finite number of linear pieces, and is able to cope with hysteresis effects, which is not possible with the Volterra series expansion.

In the remainder of this chapter the loudspeaker's nonlinear response will be modelled using the Volterra series expansion.

6.2 Volterra series expansion.

The loudspeaker is assumed to be a nonlinear, time-invariant system. The response of such a system can be written in a Volterra series expansion if the nonlinearities and the input signal are sufficiently small to guarantee the convergence of the series and if the response is unambiguous [37,38], which excludes a description of hysteresis effects and subharmonic generation [35].
The response $y(t)$ of the system can then be written in the form

$$y(t) = \int_0^\infty h_1(\tau)\, x(t-\tau)\, d\tau +$$

$$\int_0^\infty \int_0^\infty h_2(\tau_1,\tau_2)\, x(t-\tau_1)\, x(t-\tau_2)\, d\tau_1\, d\tau_2 + \qquad 6.11$$

$$\int_0^\infty \int_0^\infty \int_0^\infty h_3(\tau_1,\tau_2,\tau_3)\, x(t-\tau_1)\, x(t-\tau_2)$$

$$x(t-\tau_3)\, d\tau_1\, d\tau_2\, d\tau_3 + \ldots\ldots .$$

where $x(t)$ is the system input at time t and the h_n's are generalized impulse responses. The first term represents the convolution for a linear system.
Throughout the remainder of this chapter we will use a truncated Volterra series, which was truncated after the third-order term.
It should be noted that the loudspeaker response cannot be written as an ordinary power series of the input. This is only possible for a memoryless or frequency-independent (dispersion-free) system, like a network with nonlinear resistors. In that case the impulse responses are Dirac pulses and the Volterra series degenerates into a power series. The loudspeaker, however, is a dispersive system, for which we have to take the past values of the input into account, which leads to a Volterra series description.
By analogy with linear system theory, we can also find a relation between the Laplace transforms of the input and the output time signals [37,38].

$$Y(p) = H_1(p)X(p) + A\{H_2(p_1,p_2)\, X(p_1)\, X(p_2)\} +$$
$$A^2\{H_3(p_1,p_2,p_3)\, X(p_1)\, X(p_2)\, X(p_3)\} + \ldots , \qquad 6.12$$

in which A and A^2 denote the "contraction operators" or "association of variables" [37,38]. The operator A transforms a function of two variables into a function of a single variable and is defined by the integral transformation

$$Y_1(p) = \frac{1}{2\pi j} \int_{-j\infty}^{+j\infty} Y_2(p-s, s)\, ds . \qquad 6.13$$

The operator A^2 is defined in a similar way for a function of three variables.

The system functions $H_1(p)$, $H_2(p_1,p_2)$ and $H_3(p_1,p_2,p_3)$ are the multidimensional Laplace transforms of the corresponding impulse responses $h_1(t)$, $h_2(t_1,t_2)$ and $h_3(t_1,t_2,t_3)$ in the Volterra series.
The function $H_1(p)$ is the linear system response function. The system response function $H_2(p_1,p_2)$ can be found by driving the system with the signal $\exp(p_1 t) + \exp(p_2 t)$, which yields the response

$$e^{2p_1 t}\, H_2(p_1,p_1) + e^{2p_2 t}\, H_2(p_2,p_2)$$
$$+ 2\, e^{(p_1+p_2)t}\, H_2(p_1,p_2) . \qquad 6.14$$

and the system function $H_3(p_1,p_2,p_3)$ by driving the system with the signal $\exp(p_1 t) + \exp(p_2 t) + \exp(p_3 t)$, which yields the response

$$e^{3p_1 t}\, H_3(p_1,p_1,p_1) + e^{3p_2 t}\, H_3(p_2,p_2,p_2) +$$
$$e^{3p_3 t}\, H_3(p_3,p_3,p_3) + 3e^{(2p_1+p_2)t}\, H_3(p_1,p_1,p_2) +$$
$$3e^{(2p_1+p_3)t}\, H_3(p_1,p_1,p_3) +$$
$$3e^{(2p_2+p_1)t}\, H_3(p_2,p_2,p_1) +$$
$$3e^{(2p_2+p_3)t}\, H_3(p_2,p_2,p_3) +$$
$$3e^{(2p_3+p_1)t}\, H_3(p_3,p_3,p_1) +$$
$$3e^{(2p_3+p_2)t}\, H_3(p_3,p_3,p_2) +$$
$$6e^{(p_1+p_2+p_3)t}\, H_3(p_1,p_2,p_3) . \qquad 6.15$$

It can be noted that the functions h_i and H_i are symmetric [37,38], e.g. $h_2(\tau_1,\tau_2) = h_2(\tau_2,\tau_1)$.

6.3 Lumped parameter model system functions.

6.3.1 Voltage drive

If the loudspeaker is driven with a voltage of the form

$$E_g = e^{p_1 t} + e^{p_2 t} + e^{p_3 t} , \qquad 6.16$$

then the voice coil excursion can be written in the form

$$x(t) = q_1(p_1)\, e^{p_1 t} + q_1(p_2)\, e^{p_2 t} + q_1(p_3)\, e^{p_3 t} +$$
$$q_2(p_1,p_2)\, e^{(p_1+p_2)t} + q_2(p_1,p_3)\, e^{(p_1+p_3)t} + \ldots \qquad 6.17$$
$$q_2(p_2,p_3)\, e^{(p_2+p_3)t} + \ldots$$
$$q_3(p_1,p_2,p_3)\, e^{(p_1+p_2+p_3)t} + \ldots .$$

Substituting this equation in the differential Eq. (6.9) yields the linear, the second-order and the third-order response terms. The linear response term equals

$$q_1(p_1) = \frac{1}{(\alpha + \beta p_1 + \gamma p_1^2 + \delta p_1^3)} . \qquad 6.18$$

Eq. 6.17 describes the voice coil excursion versus

input voltage. The sound radiation, however, is proportional to the voice coil acceleration and therefore we define system functions that describe the voice coil acceleration versus input voltage. The first-order or linear system function equals

$$H_1(p_1) = p_1^2\, q_1(p_1)\,. \qquad 6.19$$

The second-order response term equals

$$q_2(p_1,p_2) = -q_1(p_1+p_2)\,q_1(p_1)\,q_1(p_2)\Big\{c(p_1^2+p_2^2) + g(p_1^2p_2+p_1p_2^2) + d(p_1^2+p_2^2) + c(p_1+p_2) + 2fp_1p_2 + 2b + a\left(\frac{1}{q_1(p_1)}+\frac{1}{q_1(p_2)}\right)\Big\}\,, \qquad 6.20$$

and $H_2(p_1,p_2) = \tfrac{1}{2}(p_1+p_2)^2\, q_2(p_1,p_2)\,, \qquad 6.21$

and the third-order term equals

$$q_3(p_1,p_2,p_3) = -q_1(p_1+p_2+p_3)\sum_{i=1}^{7}(Y_i+Y_j), \qquad 6.22$$

and

$$H_3(p_1,p_2,p_3) = -\frac{1}{6}q_1(p_1+p_2+p_3)\,(p_1+p_2+p_3)^2\sum_{i=1}^{7}(Y_i+Y_j)\,. \qquad 6.23$$

The parameters of Eqs. 6.18-6.23 are listed in Appendix C.

6.3.2 Current drive

If the excitation of the loudspeaker is a current, the governing differential equation of its vibration at low frequencies is given by

$$Bl\,i = m\ddot{x} + R_m\dot{x} + kx + F_r\,, \qquad 6.24$$

where F_r is the reluctance force (cf. Eq. 6.1). The current is asssumed to be of the form

$$i = e^{p_1t} + e^{p_2t} + e^{p_3t}\,. \qquad 6.25$$

Substituting Eqs. 6.1, 6.6 through 6.8 and 6.25 in the differential Eq. 6.24, yields the linear, the second-order and the third-order response terms. The linear response term equals

$$q_1(p_1) = \frac{Bl_0}{(p_1^2m + p_1R_m + k_0)}\,, \qquad 6.26$$

and

$$H_1(p_1) = p_1^2\cdot q_1(p_1)\,. \qquad 6.27$$

The second-order response term is given by

$$q_2(p_1,p_2) = \frac{b_1\{q_1(p_1)+q_1(p_2)\} - 2k_1q_1(p_1)q_1(p_2) + l_1}{(p_1+p_2)^2m + (p_1+p_2)R_m + k_0}\,, \qquad 6.28$$

and

$$H_2(p_1,p_2) = \tfrac{1}{2}(p_1+p_2)^2\, q_2(p_1,p_2)\,. \qquad 6.29$$

The third-order response term equals

$$q_3(p_1,p_2,p_3) = \frac{b_1\{A\} + 2b_2\{B\} - 2k_1\{C\} - 2k_2\{D\} + 2l_2\{E\}}{(p_1+p_2+p_3)^2m + (p_1+p_2+p_3)R_m + k_0}\,, \qquad 6.30$$

where the terms A to E are given by

$$\begin{aligned} A &= q_2(p_1,p_2) + q_2(p_1,p_3) + q_2(p_2,p_3)\\ B &= q_1(p_1)q_1(p_2) + q_1(p_1)q_1(p_3) + q_1(p_2)q_1(p_3)\\ C &= q_1(p_1)q_2(p_2,p_3) + q_1(p_2)q_2(p_1,p_3) + q_1(p_3)q_2(p_1,p_2)\\ D &= q_1(p_1)\cdot q_1(p_2)\cdot q_1(p_3)\\ E &= q_1(p_1) + q_1(p_2) + q_1(p_3)\,, \end{aligned} \qquad 6.31$$

and

$$H_3(p_1,p_2,p_3) = \tfrac{1}{6}(p_1+p_2+p_3)^2\, q_3(p_1,p_2,p_3)\,. \qquad 6.32$$

6.4 Lumped parameter model inverse system functions.

The description of a nonlinear system by its system functions is particularly suited to demonstrate the principle of a distortion reduction circuit. The response of the nonlinear system was shown to be

$$Y(p) = H_1(p)\,X(p) + A\{H_2(p_1,p_2)\,X(p_1)\,X(p_2)\} + A^2\{H_3(p_1,p_2,p_3)\,X(p_1)\,X(p_2)\,X(p_3)\}\,, \qquad 6.33$$

where the Volterra series is truncated after the third term.

The inverse circuit is defined by the equation

$$X(p) = G_1(p)\,Y(p) + A\{G_2(p_1,p_2)\,Y(p_1)\,Y(p_2)\} + A^2\{G_3(p_1,p_2,p_3)\,Y(p_1)\,Y(p_2)\,Y(p_3)\}\,. \qquad 6.34$$

In this series too the Volterra series was truncated after the third-order term. Substituting Eq. 6.33 into Eq. 6.34, and ignoring terms with an order higher than three, yields

$$X(p) \approx$$
$$G_1(p)\,H_1(p)\,X(p) + A\{[G_1(p_1+p_2)\,H_2(p_1,p_2) + G_2(p_1,p_2)\,H_1(p_1)\,H_1(p_2)]\,X(p_1)\,X(p_2)\} + A^2\{[G_1(p_1+p_2+p_3)\,H_3(p_1,p_2,p_3) + G_3(p_1,p_2,p_3)\,H_1(p_1)\,H_1(p_2)\,H_1(p_3)]\,X(p_1)\,X(p_2)\,X(p_3)\}. \quad 6.35$$

In the derivation the following property has been used [38]:

$$A\{F(p_1+p_2)\,G(p_1,p_2)\} = F(p)\,A\{G(p_1,p_2)\}. \quad 6.36$$

This equation has to be satisfied for all values of $X(p)$, which yields the equations

$$G_1(p) = \frac{1}{H_1(p)}, \quad 6.37$$

$$G_2(p_1,p_2) = \frac{-H_2(p_1,p_2)}{H_1(p_1)\,H_1(p_2)\,H_1(p_1+p_2)}, \quad 6.38$$

and $G_3(p_1,p_2,p_3) =$

$$\frac{-H_3(p_1,p_2,p_3)}{H_1(p_1)\,H_1(p_2)\,H_1(p_3)\,H_1(p_1+p_2+p_3)}. \quad 6.39$$

The first equation (Eq. 6.37) is the inverse of the linear transfer function. However, it is also possible to define a nonlinear inverse circuit that only inverts the nonlinear terms. The inverse cicuit can be described with the equation

$$Z(p) = K_1(p)\,X(p) + A\{K_2(p_1,p_2)\,X(p_1)\,X(p_2)\} + A^2\{K_3(p_1,p_2,p_3)\,X(p_1)\,X(p_2)\,X(p_3)\}, \quad 6.40$$

and the loudspeaker response is given by

$$Y(p) = H_1(p)\,Z(p) + A\{H_2(p_1,p_2)\,Z(p_1)\,Z(p_2)\} + A^2\{H_3(p_1,p_2,p_3)\,Z(p_1)\,Z(p_2)\,Z(p_3)\}. \quad 6.41$$

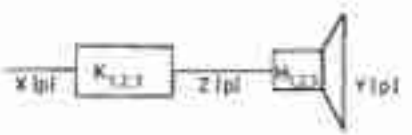

Fig. 6.3: Inverse nonlinear circuit for loudspeaker distortion reduction.

The total response of the cascade of the inverse circuit and the loudspeaker should be

$$Y(p) = H_1(p)\,X(p), \quad 6.42$$

for all values of $X(p)$, which yields the equations:

$$K_1(p) = 1, \quad 6.43$$

$$K_2(p_1,p_2) = \frac{-H_2(p_1,p_2)}{H_1(p_1+p_2)} = -\frac{1}{2}\frac{q_2(p_1,p_2)}{q_1(p_1+p_2)}, \quad 6.44$$

and

$$K_3(p_1,p_2,p_3) = \frac{-H_3(p_1,p_2,p_3)}{H_1(p_1+p_2+p_3)} = -\frac{1}{6}\frac{q_3(p_1,p_2,p_3)}{q_1(p_1+p_2+p_3)}. \quad 6.45$$

Inverting only the nonlinear terms of the Volterra series may be advantageous if the inverse function of the linear part is physically unrealizable, which occurs when $H_1(p)$ is a non-minimum phase function.

6.5 Synthesis of nonlinear system functions.

6.5.1 Voltage drive

Modelling a nonlinear system function can be done with frequency-independent nonlinear elements, such as a squarer, and frequency-dependent linear elements [38,40].
Combination of Eqs. 6.19, 6.21 and 6.23 with Eqs. 6.43, 6.44 and 6.45 yields the distortion reduction circuit system functions:

$$K_1(p) = 1, \quad 6.46$$

$$K_2(p_1,p_2) = q_1(p_1)\,q_1(p_2)\,[2(a\alpha+b) + (a\beta+c)(p_1+p_2) + (a\gamma+d)(p_1+p_2)^2 + (a\delta+e)(p_1+p_2)^3 - p_1p_2[2(a\gamma+d) - f + (3(a\delta+e)-g)(p_1+p_2)]]. \quad 6.47$$

and

$$K_3(p_1,p_2,p_3) = \tfrac{1}{6}\sum_{i=1}^{6}(y_i+Y_i). \quad 6.48$$

As an example the distortion reduction circuit implementation of Eqs. 6.46 and 6.47 is shown in Fig. 6.4. The elements of the circuit are amplifiers (1), adders (2), squarers (3) and the filter $q_1(p)$, all of which can easily be realized. However, the element p is a differentiator, which is more difficult to implement. The higher order distortion reduction circuits can also be synthesized, but show an increasing complexity.

6.5.2 Current drive

The distortion reduction system functions for the current drive case, which are found from Eqs. 6.43 through 6.45 and 6.26 through 6.32, can be realized more easily. The linear term equals

$$K_1(p) = 1. \quad 6.49$$

The second-order term is given by

$$K_2(p_1,p_2) = \frac{-1}{2Bl_0}[b_1\{q_1(p_1) + q_1(p_2)\} - 2k_1 q_1(p_1)q_1(p_2) + l_1], \quad 6.50$$

and the implementation of Eqs. 6.49 and 6.50 is shown in Fig. 6.5.

The third-order term equals

$$K_3(p_1,p_2,p_3) = \frac{-1}{6Bl_0}[b_1\{A\} + 2b_2\{B\} - 2k_1\{C\} - 6k_2\{D\} + 2l_2\{E\}], \quad 6.51$$

and its implementation is shown in Fig. 6.6.

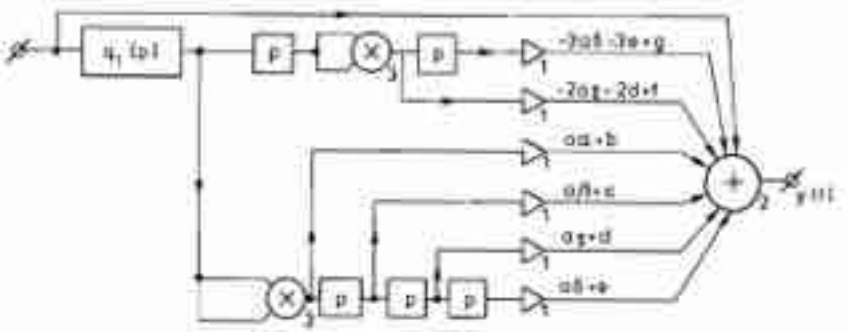

Fig. 6.4: Implementation of a voltage drive second-order distortion reduction circuit.

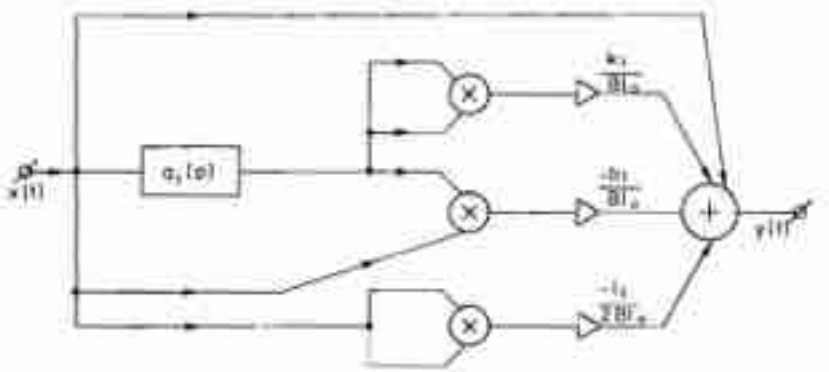

Fig. 6.5: Implementation of a current drive second-order distortion reduction circuit.

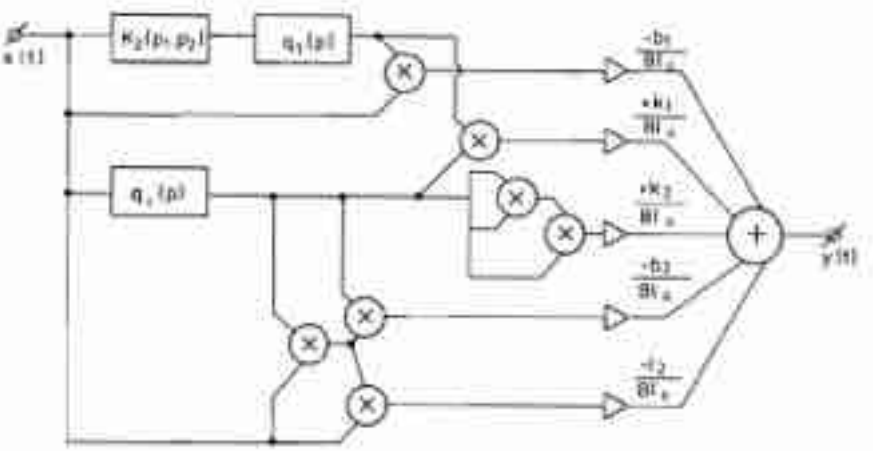

Fig. 6.6: Implementation of a current drive third-order distortion reduction circuit (the third-order term only). The implementation of $K_2(p_1,p_2)$ is shown in Fig. 6.5.

The distortion reduction system function for the current drive case, which includes the inversion of the linear term, can also be easily realized. Its first-order term equals

$$Q_1(p) = \frac{1}{H_1(p)} = \frac{p^2 m + pR_m + k_0}{p^2\, Bl_0^2}. \qquad 6.52$$

The second-order term is given by

$$Q_2(p_1,p_2) = \frac{-H_2(p_1,p_2)}{H_1(p_1)H_1(p_2)H_1(p_1+p_2)} = \frac{-\frac{1}{2}q_2(p_1,p_2)}{(p_1p_2)^2 q_1(p_1)q_1(p_2)q_1(p_1+p_2)}, \qquad 6.53$$

or

$$Q_2(p_1,p_2) = \frac{-1}{2Bl_0}\left[b_1\frac{1}{(p_1p_2)^2}\left\{\frac{1}{q_1(p_1)}+\frac{1}{q_1(p_2)}\right\} - \frac{2k_1}{(p_1p_2)^2} + \frac{l_1}{(p_1p_2)^2 q_1(p_1)q_1(p_2)}\right]. \qquad 6.54$$

Its implementation is shown in Fig. 6.7.

The third-order term equals

$$Q_3(p_1,p_2,p_3) = \frac{-H_3(p_1,p_2,p_3)}{H_1(p_1)H_1(p_2)H_1(p_3)H_1(p_1+p_2+p_3)} = \frac{-\frac{1}{6}q_3(p_1,p_2,p_3)}{(p_1p_2p_3)^2 q_1(p_1)q_1(p_2)q_1(p_3)q_1(p_1+p_2+p_3)}, \qquad 6.55$$

which can be written in the form

$$Q_3(p_1,p_2,p_3) = \frac{-1}{6Bl_0}\left[\frac{b_1\{A\}+2b_2\{B\}-2k_1\{C\}-6k_2\{D\}+2l_2\{E\}}{(p_1p_2p_3)^2 q_1(p_1)q_1(p_2)q_1(p_3)}\right], \qquad 6.56$$

where the terms A through E can be found from Eq. 6.31. Its implementation is shown in Fig. 6.8.

6.6 Calculated versus measured nonlinear response of an electrodynamic loudspeaker.

In the preceding sections a Volterra series analysis of the nonlinear response of an electrodynamic loudspeaker was presented. Compared with other types of analysis, this analysis has two advantages:

- The analysis of the physical model puts the relative significance of the different sources of nonlinearities into evidence. To obtain this information from experiments is very difficult in practice.
- In general, it is possible to design an inverse nonlinear distortion reduction circuit if the nonlinear system functions are known.

In this section it will be shown that the analysis described in the previous sections indeed predicts the nonlinear response of a loudspeaker with a reasonable accuracy.

It can be argued that the linear and nonlinear responses of individual loudspeakers may differ. Therefore twelve different loudspeakers (Philips AD80603/W4) were measured in a test box (25 liters). The measurements included the on-axis linear frequency response and second and third-order harmonic and intermodulation distortions under free field conditions. From these measurements it was concluded that for low frequencies below about 250 Hz all loudspeaker responses are fairly similar. This is illustrated in Figs. 6.9 and 6.10. Fig. 6.9 shows the on-axis linear and third harmonic responses of two

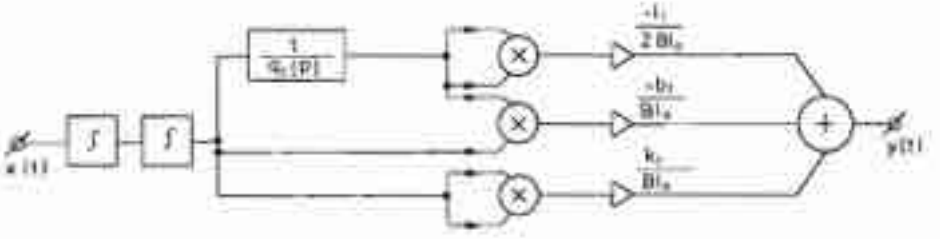

Fig. 6.7. Implementation of a current drive second-order distortion reduction circuit according to Eq. 6.54.

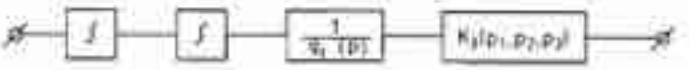

Fig. 6.8. Implementation of a current drive third-order distortion reductoon circuit according to Eq. 6.55. The implementation of $K_3(p_1,p_2,p_3)$ is shown in Fig. 6.6.

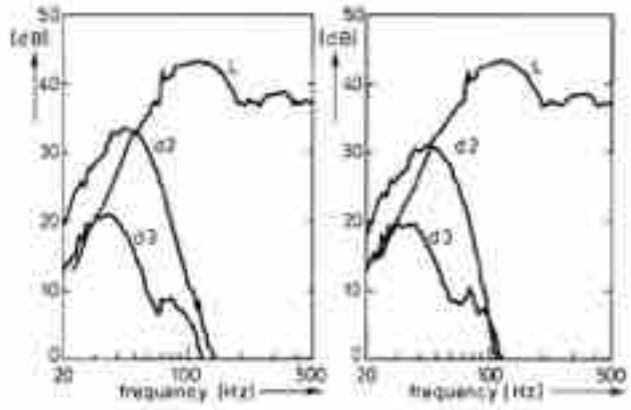

Fig. 6.9: Frequency response of two representative woofer loudspeakers. The linear response is indicated with L, whereas d2 and d3 are the second and third-order harmonic distortion products (raised 20 dB), respectively. The vertical scale is arbitrary.

representative loudspeakers which were driven with a sinusoidal input voltage of 2 V RMS.
Fig. 6.10 shows the same on-axis linear responses and a second and a third-order intermodulation product. The curve that is indicated with (im + 2) shows the response at $(f_1 + f_2)$ if f_1 is fixed at 80 Hz, as a function of f_2. The (im + 3) curve shows the response of $(2f_1 + f_2)$ with the same input signal. The vertical scales of both Figs. 6.9 and 6.10 are arbitrary.

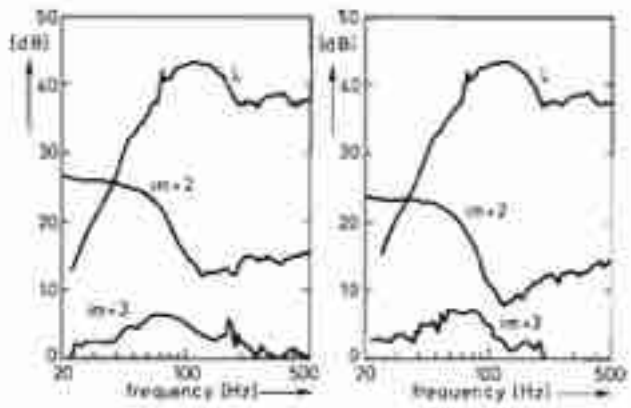

Fig. 6.10: Frequency response of two representative woofer loudspeakers. The linear response is indicated with L, whereas the (im + 2) and (im + 3) are second and third-order intermodulation products, which are raised 20 dB.

Although the responses of different loudspeakers are fairly similar, the linear responses show small irregularities, which are not predicted by the lumped parameter model. The acceleration of the voice coil shows a smoother response, at low frequencies, is in accordance with the lumped parameter model predictions. Also it is known that at low frequencies the loudspeaker response is proportional to the voice coil acceleration. Therefore we will use the voice coil acceleration data of a single loudspeaker for comparison of measured and calculated responses. This loudspeaker was modified in the following way: an accelerometer (Brüel and Kjaer type 8307) was mounted on the voice coil former, which increased the total moving mass from 17.8 to 19.1 grams. It is assumed that this modification does not influence the nonlinear effects of interest (force factor, suspension stiffness and voice coil self-inductance).

6.6.1 Measurement of loudspeaker linear parameters and estimation of the nonlinear characteristics.

The linear loudspeaker parameters can be measured with a straightforward technique [43]. The total moving mass was found to be 19.1 grams (including accelerometer), the voice coil resistance was 3.2 Ohm and the mechanical damping was 1.0 N.s/m.
The nonlinear parameters (force factor, self-inductance and suspension stiffness) were measured as a function of the voice coil excursion. The coefficients of the power series (Eqs. 6.6, 6.7 and 6.8) were found from a least-squares curve fitting of the measurement data. The curve fitting of the force factor measurement data yields the coefficients:

$$\begin{aligned} Bl_0 &= 5.05 \pm 0.05\ [\mathrm{N/A}] \\ b_1 &= -23 \pm 8\ [\mathrm{N/Am}] \\ b_2 &= -48000 \pm 1000\ [\mathrm{N/Am^2}]. \end{aligned} \qquad 6.57$$

The spring constant of the unmounted loudspeaker as a function of the excursion exhibits a hysteresis as shown in Fig. 6.11.

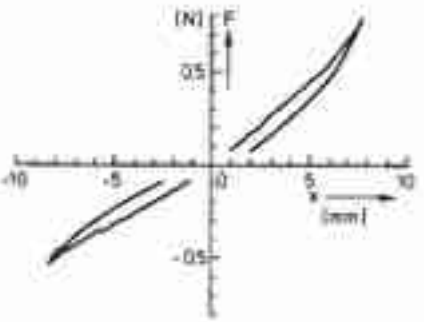

Fig. 6.11: Force vs. displacement curve of the suspension stiffness of an unmounted woofer loudspeaker.

Curve fitting yields the following values for the coefficients k_0, k_1 and k_2:

$$\begin{aligned} k_0 &= 574 \pm 30\ [\mathrm{N/m}] \\ k_1 &= 24000 \pm 2000\ [\mathrm{N/m^2}] \\ k_2 &= 3.2\ 10^6 \pm 0.6\ 10^6\ [\mathrm{N/m^3}] \end{aligned} \qquad 6.58$$

A dynamic measurement of the suspension stiffness (from the fundamental resonance frequency) yielded a value of 1120 N/m. This large discrepancy between the static and dynamic spring constants raises ques-

tions as to the reliability of the measured data.
The spring constant of the unmounted loudspeaker should be added to that of the box air spring constant. This box air stiffness too is nonlinear and its characteristic can be evaluated analytically. We assume the box air compression to be an adiabatic process, i.e. the total pressure (p_0+p) and the total volume (V_0+V) obey the relation

$$(p_0+p)(V_0+V)^\gamma = p_0 V_0^\gamma, \qquad 6.59$$

where $\gamma = 1.4$, p_0 is the static pressure, p_0+p the instantaneous pressure, V_0 the static volume and V_0+V the instantaneous volume.
The box air stiffness spring constant is given by

$$k_{box} = \frac{-dF_b}{dx} = -S\frac{d(p_0+p)}{dx}, \qquad 6.60$$

where S is the effective cone surface and x is the cone excursion. Rewriting Eq. 6.59 in the form

$$(p_0+p)(V_0+Sx)^\gamma = p_0 V_0^\gamma, \qquad 6.61$$

and differentiating with respect to x yields

$$\frac{dp}{dx} = -\gamma S(p_0+p)(V_0+Sx)^{-1}. \qquad 6.62$$

Combination of Eqs. 6.60, 6.61 and 6.62 yields

$$k_{box} = \gamma S^2 \frac{p_0}{V_0}\left(1+\frac{Sx}{V_0}\right)^{-(\gamma+1)}. \qquad 6.63$$

The power series expansion of $(1+x)^n$ is given by [44]

$$(1+x)^n = 1 + \sum_{n=1}^{\infty}\left\{\binom{\alpha}{n}x^n\right\}, \qquad 6.64$$

which is used to approximate 6.63 by

$$k_{box} = \gamma S^2 \frac{p_0}{V_0}\left[1-(\gamma+1)\left(\frac{Sx}{V_0}\right)+(\gamma+1)(\gamma+2)\left(\frac{Sx}{V_0}\right)^2\right]. \qquad 6.65$$

The coefficients of the series expansion of the box stiffness are found to be

$$\begin{aligned} k_{box_0} &= 2270\ [\mathrm{N/m}],\\ k_{box_1} &= -4357\ [\mathrm{N/m^2}],\\ k_{box_2} &= 5925\ [\mathrm{N/m^3}]. \end{aligned} \qquad 6.66$$

The coefficients of the series expansion of the total stiffness are the sum of the respective terms of unmounted loudspeaker and the box air stiffness:

$$\begin{aligned} k_0 &= 3389\ [\mathrm{N/m}],\\ k_1 &= 19500\ [\mathrm{N/m^2}],\\ k_2 &= 3.22\ 10^6\ [\mathrm{N/m^3}]. \end{aligned} \qquad 6.67$$

The last parameter to be determined is the voice coil self-inductance. The measurement of the voice coil self-inductance was done by fixing the voice coil at a known excursion x and measuring the magnitude and phase of the electrical input impedance. This self-inductance was found to depend both on the voice coil excursion and the frequency. The coefficients for the series expansion of the self-inductance in the vicinity of 100 Hz were determined by a least-squares curve fitting of the measured data:

$$\begin{aligned} L_{E_0} &= 1.5\ 10^{-3}\ [\mathrm{H}]\\ l_1 &= -83\ 10^{-3} \pm 7\ 10^{-3}\ [\mathrm{H/m}]\\ l_2 &= 3.3 \pm 0.9\ [\mathrm{H/m^2}] \end{aligned} \qquad 6.68$$

6.6.2 Harmonic and intermodulation distortion: measured versus calculated response.

The measured values in the series expansion coefficients of the nonlinear component characteristics were used to evaluate the second-order and third-order distortion components of the voice coil acceleration. The first result is shown in Fig. 6.12.

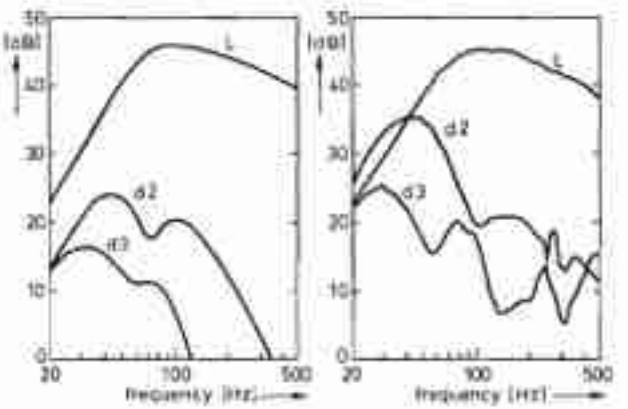

Fig. 6.12. Measured (right) and calculated (left) curves of the linear (L), second harmonic (d2) and third harmonic (d3) responses of the voice coil acceleration (arbitrary vertical scale).

The linear curves show a reasonable resemblance, but although a resemblance can be seen in the qualitative behavior of the distortion curves, it will be clear that the quantitative agreement is not satisfactory. In the preceding section it was argued that some care has to be taken in using the measured values of the nonlinear component characteristics, because of the large discrepancy between the statically and dynamically measured quantities. Therefore the coefficients of the excursion-dependent terms in the nonlinear characteristics were modified to fit the actual measured distortion responses. This was done by first fitting the second-order harmonic response data in a current-driven model, which eliminates the influence of the self-inductance, after which the self-inductance series coefficients in the voltage-driven model were adjus-

ted. This procedure was repeated for the third-order harmonic distortion. The resultant responses are shown in Fig. 6.13 and the qualitative agreement between the distortion response curves is reasonable at frequencies below 200 Hz. The measured and modified series expansion coefficients of the nonlinear component characteristics are listed in table 6-I.

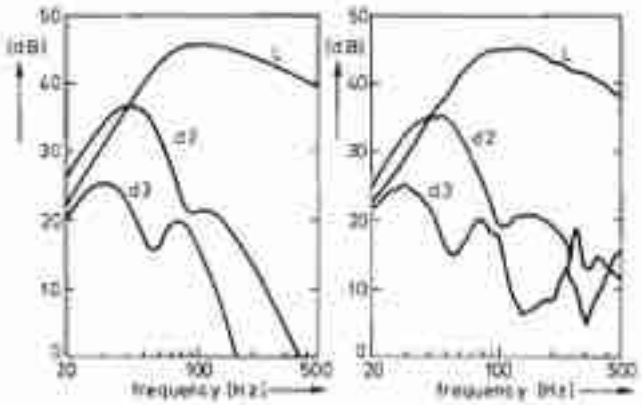

Fig. 6.13: Measured (right) and calculated (left) curves of the linear (L), second harmonic (d2) and third harmonic (d3) responses of the voice coil acceleration (arbitrary vertical scale).

parameter	measured value	optimization result	dimension
b_1	−23	−230	[N/Am]
b_2	−48000	$-1.0 \cdot 10^5$	[N/Am^2]
k_1	24000	60000	[N/m^2]
k_2	$3.22 \cdot 10^6$	$3.33 \cdot 10^6$	[N/m^3]
l_1	−0.083	-0.150	[H/m]
l_2	3.3	50.0	[H/m^2]

Table 6-I: Measured and modified series expansion coefficients.

The value of k_2 shows a good agreement, the values of b_2, k_1 and l_1 differ by about a factor of two and the values of b_1 and l_2 differ by more than one order of magnitude.
The set of modified coefficients was used to evaluate a second- and a third-order intermodulation distortion. Fig. 6.14 shows the response at $f_1 + f_2$ (im + 2) and $2f_1 + f_2$ (im + 3) for a fixed frequency f_1 at 80 Hz, as a function of the second frequency f_2.

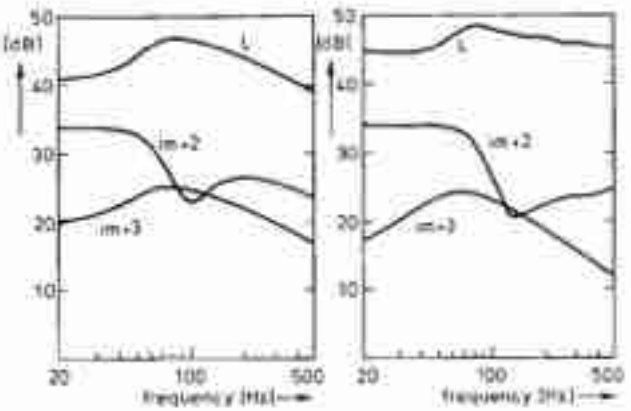

Fig. 6.14: Measured (right) and calculated (left) curves of the linear, second-order (im + 2) and third-order (im + 3) intermodulation responses of the voice coil acceleration with an arbitrary vertical scale.

Although no perfect agreement between calculated and measured responses is obtained, the resemblance is reasonable.

6.7 Discussion.

The agreement between measured and calculated distortion data of the voice coil acceleration was found to be reasonable at low frequencies below about 250 Hz for second and third-order harmonic and intermodulation distortion components. It may be concluded that the model is reliable in describing the second and third-order distortion responses for an electrodynamic loudspeaker at low frequencies.
It was found necessary, however, to modify the coefficients in the series expansion of the nonlinear component characteristics (by curve-fitting of the measured data) in order to improve the agreement between the measured and calculated data. Possible explanations for the discrepancies are:

- The difference between statically and dynamically measured data raises questions as to the reliability of such measurements.
- The model is too simple, but the distortion mechanisms used are capable of managing other distortion mechanisms to some extent.
- The model is too simple because the nonlinear component characteristics exhibit hysteresis and frequency dependence.

7. Conclusions

Chapter 2 of this thesis presents a description of a lumped parameter model of an electrodynamic loudspeaker, which is capable of describing the behavior of the loudspeaker at low frequencies. The model fails to describe the loudspeaker behavior at higher frequencies, i.e. above the transition frequency (cf. Eq. 2.4). Also the model cannot cope with the nonlinearities of an actual loudspeaker.

More sophisticated models of the loudspeaker, which supplement the simple lumped parameter model, are discussed in chapters 4, 5 and 6.

In chapter 3 a new description of the transient response of a loudspeaker or loudspeaker system is proposed: the Wigner distribution of its impulse response. This Wigner distribution is shown to be a powerful tool for evaluating the (transient) time-frequency response of a loudspeaker.

The Wigner distribution allows the introduction of objective optimization criteria for both a single transducer and a combination of transducers. Deviations from the ideal behavior can be located. For example, the decaying ringing contributions of the bending and membrane resonances of cone and dome loudspeakers, as well as time delays and reflections, can be recognized from the occurrence of spurious contributions.

To simplify the interpretation of the distribution or to emphasize particular effects it may be convenient to use an adapted representation. Examples are the use of the analytical signal to suppress disturbing interference contributions and the contour plot, in which time delays are easily recognized. In order to suppress disturbing or irrelevant contributions one could also average the distribution with a suitable window. It is important to note that although such processing may make sense, we always have to return to the original Wigner distribution of the signal if we have any problem with the interpretation of a particular representation. It may be advantageous to carry out a conversion of the axes, e.g. a logarithmic frequency or amplitude scaling. This might be important when the deviations of the time-frequency behavior from the ideal behavior are to be emphasized. This is closely related to the audibility of phenomena, which is not discussed in this thesis. It is clear that for a proper evaluation of the significance of deviations from ideal time-frequency responses, it is important to have more knowledge about the audibility of these deviations. However, the audibility of many transient phenomena is not yet known.

If a satisfactory theory could be found for this important domain of acoustical perception, it might be possible to average the Wigner distribution with an appropriate function, which would result in a representation showing only the audible contributions of the distribution. Given the state of the art concerning our knowledge about the perception of acoustical transient phenomena and our ability to formulate mathematical or physical models of this hearing mechanism, this requires much additional research. The Wigner distribution can be very useful in this study, since it gives a proper distribution of the energy of the stimulus signal, which allows an accountable application of weighting, averaging and transformation.

Also considered is the usefulness of a linear-phase loudspeaker design (not to be confused with time-alignment of separate transducers). Such an approximated linear-phase behavior is often claimed to affect the transient response of a loudspeaker favorably. From the Wigner distributions of the minimum-phase and linear-phase filter systems (Chapter 3, Figs. 18 and 21) it is clear that the only differences are the position of the "ears" relative to the mountain ridge and the delay of this mountain ridge.

The "ears" in the graphical representation of the Wigner distribution of an actual loudspeaker system are located in frequency regions that are assumed to have hardly any effect on perceptional phenomena. If these frequency regions are not considered to be important, then there is no difference between the minimum- and linear-phase systems. This indicates that the need to design a loudspeaker system with an approximated linear-phase behavior is questionable.

The influence of a nonrigid cone on the sound radiation has been discussed in chapter 4. The sound radiation from a nonrigid cone increases in the break-up frequency region. The average increase is correctly predicted by the membrane model, i.e. the model in which the bending stiffness vanishes. In the break-up frequency region the idealized (lossless) membrane model differential equations show a singularity on the cone, the position of which moves from the outer to the inner edge with increasing frequency according to Eq. 4.11. A trapping of energy at the singularity on the cone in the lossless membrane model was reported by van der Pauw [32], which effect results in a large transverse amplitude of the vibration at this point. This large transverse amplitude of the membrane vibration generates a bending vibration at the site of the singularity. However, bending waves cannot propagate at the inner cone part (between the inner edge and the singularity point), as shown in Ref. [25], and will decrease exponentially with increasing distance from the singularity point.

At the outer cone part (between the singularity point and the outer edge), bending waves do propagate and,

after reflection at the outer edge, lead to standing waves. In effect, at the singularity we find a conversion from membrane energy into bending energy [32].
The influence of the material damping on the membrane vibration in the break-up frequency region is small, because the conversion of energy to bending waves can be interpreted as a damping mechanism. On the other hand the bending waves are strongly influenced by the material damping.
The sound radiation of the nonrigid cone can be split into the contributions of the independent solutions of the differential equations that describe its vibration. In contrast to a plane plate, the membrane vibrations in the cone have a transverse component in the displacement and thus contribute to the sound radiation. In the break-up frequency region the amplitude of the transverse membrane vibration is relatively large, which results in a rise of the sound radiation in the break-up frequency region. At frequencies below the break-up frequency region bending waves cannot propagate and a generated bending wave will decay exponentially. Therefore, the sound radiation below break-up is mainly determined by the membrane solutions.
In the break-up frequency region the sound radiation due to the membrane solutions of the conical-shaped and concave cone show a considerable rise. The contributions of the bending solutions to the sound radiation of a cone with a conical shape are small compared with those of the membrane solutions and cause a fine structure on the sound pressure curve. The contributions of the bending solutions to the sound radiation of a concave cone shape are even smaller and can be neglected.
The convex cone shows only a small rise in the sound radiation of the membrane solutions. The contributions of the bending solutions to the sound radiation are much higher and can no longer be neglected. The bending solutions yield a number of bending resonance peaks and dips in the break-up frequency region.
The moving average of the sound radiation in the break-up frequency region, which is correctly predicted by the membrane model, is strongly influenced by the voice coil mass. Such a mass yields an additional roll-off of the sound radiation in this frequency region. Therefore, the sound radiation of a concave cone with voice coil mass shows a peak which originates from the membrane solutions. These membrane solutions are not very sensitive to a material damping in the break-up frequency region and the peak amplitude is hardly affected by such a damping.
The sound radiation from a convex cone with a voice coil mass shows a number of peaks and dips that originate from the bending solutions, which vanish after application of some suitable smoothing. The amplitudes of these peaks and dips can be decreased by increasing the material damping.
The choice of a cone shape depends on the material properties. For example, metal has a large specific mass and the thickness of a metal cone should be small in order to limit the total moving mass, which yields a small bending stiffness. The ratio E/ρ is relatively large compared with that of a commonly used cone material such as paper, so that the break-up frequency region starts at relatively high frequencies. Furthermore the material damping of a metal is small. Therefore the concave cone shape is optimum for a metal cone: the influence of the bending resonances is minimal and the break-up peak is located at relatively high frequencies.
A commonly used cone material, for example paper or plastic (e.g. polypropylene) material, has a much smaller ratio of E/ρ and a much larger material damping, which is able to damp the bending resonances effectively. Therefore the convex cone shape is optimum for such a cone material: the sound pressure response shows a smooth curve (provided that the bending resonances are damped sufficiently) which extends towards relatively high frequencies.
In Chapter 5 two topics associated with the transient behavior of loudspeakers and loudspeaker systems have been discussed. Section 5.1 considers the influence of the geometry of a radiator on the transient behavior of the on-axis sound radiation. It is shown that for a rigid axisymmetric radiator the plane piston has the best transient behavior. The transient behavior of a dome-shaped radiator is also reasonable, especially if the ratio of dome height to equivalent piston radius is less than unity. The cone-shaped radiator, however, shows a considerable transient distortion in the form of a widening or spreading of the response in the time direction at middle and lower frequencies. This distortion is found with both the straight cone-shaped radiator and the bent cone-shaped radiator, like the convex and the concave cone. The effect of the transient distortion can be reduced by fitting a dust cap. If the cone cavity volume is decreased by increasing the size of the dust cap, then the transient distortion will be further reduced.
The topic of sections 5.2 and 5.3 is the transient behavior of some known crossover filters for coincident and noncoincident drivers. The types of crossover filter functions are the constant-voltage, the all-pass and the compromise filter function. Also discussed is an optimum choice of the crossover functions for noncoincident drivers, the all-pass Linkwitz-Riley filter functions. It is concluded that none of these filter functions gives rise to any substantial transient distortion with coincident drivers, provided that the proper phasing is used. In the case of noncoincident drivers it is concluded that, for the

transient response too, the Linkwitz-Riley filters are the optimum choice, provided that the proper phasing is used. However, for all these filter functions the proper alignment with respect to time is maintained only on a limited beamwidth in the plane of the two drivers' axes. This beamwidth can be increased if the spacing between the drivers is decreased.

Finally in section 6 it is shown that the low frequency distortion of an electrodynamic loudspeaker can be predicted from a Volterra series model.

The agreement between measured and calculated distortion data of the voice coil acceleration is found to be reasonable for low frequencies below about 250 Hz for second and third-order harmonic and intermodulation distortion components. It may be concluded that the model is reliable in describing the second and third-order distortion responses for an electrodynamic loudspeaker at low frequencies.

It is found necessary, however, to modify the coefficients in the series expansion of the nonlinear component characteristics (by curve-fitting of the measured data) in order to improve the agreement between the measured and calculated data. Possible explanations for the discrepancies are:

- The difference between statically and dynamically measured data raises questions as to the reliability of such measurements.
- The model is too simple, but the distortion mechanisms used are capable of managing other distortion mechanisms to some extent.
- The model is too simple because the nonlinear component characteristics exhibit hysteresis and frequency dependence.

8. References

1. L.L. Beranek, Acoustics,
McGraw-Hill, New York, 1954.
2. H.F. Olson, Acoustical Engineering,
Van Nostrand, 1957.
3. R.B. Randall, Application of BK Equipment to Frequency Analysis,
Brüel and Kjaer, Naerum, Denmark, 1977.
4. J.M. Berman and L.R. Fincham, The Application of Digital Techniques to the Measurement of Loudspeakers,
JAES, vol. 25, no. 6, 1977.
5. S.H. Linkwitz, Active Crossover Networks for Non-Coincident Drivers,
JAES, vol. 24, no. 1, 1976, pp. 2-8.
S.H. Linkwitz, Passive Crossover Networks for Non-Coincident Drivers,
JAES, vol. 26, no. 3, 1978, pp. 149-150.
6. R.H. Small, Constant-Voltage Cross-Over Network Design,
JAES, vol. 19, no. 1, 1971, pp. 12-19.
7. H.F. Olson, Dynamical Analogies,
Van Nostrand, 1958.
8. P.M. Morse and K.U. Ingard, Theoretical Acoustics,
McGraw-Hill, New York, 1968.
9. W. Soedel, Vibrations of Shells and Plates,
M. Dekker Inc., 1981.
10. A.W. Leissa, Vibration of Shells,
Nasa 1973, SP-288.
11. V.V. Novozhilov, The Theory of Thin Shells,
Noordhof, Groningen, 1959.
12. E. Reissner, A New Derivation of the Equations for the Deformations of Elastic Shells,
Amer. J. Math., 63, 1941, p.177.
13. F.J.M. Frankort, Vibration and Sound Radiation of Loudspeaker Cones,
Philips Res. Rep. Suppl., 1975, no. 2.
14. A.E.H. Love, On the Small Free Vibrations and Deformations of Thin Elastic Shells,
Phil. Trans. Royal Soc., vol. 179A, 1888.
15. E. Skudrzyk, Simple and Complex Vibratory Systems,
Pennsylvania University Press, London, 1968.
16. A.W. Leissa, Vibration of Plates,
Nasa 1969, SP-160.
17. J.C. Snowdon, Vibration and Shock in Damped Mechanical Systems,
John Wiley, 1968.
18. C. Zwikker, Technische Physik der Werkstoffe,
Springer Verlag, Berlin, 1942.
19. A. Kalnins, Analysis of Shells of Revolution Subjected to Symmetrical and Nonsymmetrical Loads,
Journal of Applied Mechanics, vol. 31, 1964, p 467.
20. E.W. Ross, Asymptotic Analysis of the Axisymmetric Vibrations of Shells,
Journal of Applied Mechanics, vol. 33, 1966, p 85.
21. E.W. Ross, Transition Solutions for Axisymmetric Shell Vibrations,
Journal of Math. and Physics, vol. 45, 1966, p 335.
22. R.W. Hamming, Numerical Methods for Scientists and Engineers,
McGraw Hill, 1962.
23. J. Zonneveld, Automatic Numerical Integration,
Math. Centre Tracts, no. 6, 1964, Math. Centrum, Amsterdam.
24. G. Dahlquist and A. Bjorck, Numerical Methods,
Prentice-Hall, 1974.
25. E.W. Ross and W.T. Matthews, Frequencies and Mode Shapes for Axisymmetric Vibration of Shells,
Journal of Applied Mechanics, vol. 34, 1967, p 73.
26. A. Kalnins, Free Vibration of Rotationally Symmetric Shells,
J.Acoust.Soc.Am., vol. 36, no. 7, 1967, p 1355.
27. O.C. Zienkiewicz, The Finite Element Method,
McGraw Hill, 1977.
28. M.R. Schroeder, Models of Hearing,
Proceedings of the IEEE, vol. 63, no. 9, 1975, p 1332.
29. H.W. Bode, Network Analysis and Amplifier Feedback Design,
Van Nostrand, 1946.
30. L. Cremer and M. Heckl, Structure-Borne Sound,
Springer, Berlin, 1973.
31. A.J.M. Kaizer, Numerical Calculations of the Vibration and Sound Radiation of Cone and Dome Loudspeakers with Nonrigid Diaphragms,
Proceedings 62nd Convention Audio Engineering Society, no. 1437, Brussels, 1979.
32. L.J. van der Pauw, The Trapping of Acoustical Energy by a Conical Membrane and its Implications for Loudspeaker Cones,
J.Acoust.Soc.Am., vol. 68, 1980, p 1163.
33. T. Shindo et al., Effect of Voice-Coil and Surround on the Vibration and Sound Pressure Response of Loudspeaker Cones,
JAES, vol. 28, no. 7/8, 1980, p 490.
34. R.P. de Wit, A.J.M. Kaizer and F.J. Op de Beek, Numerical Optimization of the Cross-Over Filters in a Multiway Loudspeakersystem,
Proceedings 75th Convention Audio Engineering Society, no. 2057, Paris, 1984.
Submitted to the Journal of the Audio Engineering Society.
35. P.O. Pedersen, Sub-Harmonics in Forced Oscillations in Dissipative Systems,
Danmarks Naturvidenskabelige Samfund, Ingeniorvidenskabelige Skrifter A 35, Copenhagen, 1933.
36. D.W. Van Wulfften Fahlte, Doppler Effect in Loudspeakers,
Acustica, vol. 28, no. 1, 1973, pp. 1-11.
37. M. Schetzen, The Volterra and Wiener Theories of Non-Linear Systems,
John Wiley, 1980.
38. H.-J. Butterweck, Frequenzabhängige nichtlineare Übertragungssysteme,
Archiv Elektr. Übertragung, vol. 21, no. 5, 1967, pp. 239-254.
39. W.M.G. Van Bokhoven, Piecewise-Linear Modelling and Analysis,
Thesis, Eindhoven University of Technology, 1981.
40. H.B. Smets, Analysis and Synthesis of Nonlinear Systems,
IRE Trans. on Circuit Theory, vol. CT-7, no. 4, 1960, pp. 459-469.
41. W.J. Cunningham, Non-Linear Distortion in Dynamic Loudspeakers due to Magnetic Effects,
J.Acoust.Soc.Am., vol. 21, no. 3, 1949, pp. 202-207.
42. G.H. van Leeuwen, Loudspeaker Distortion,
M.Sc. Thesis, Eindhoven University of Technology, 1983.
43. J.R. Ashley and M.D. Swan, Experimental Determination of Low-Frequency Loudspeaker parameters,
JAES, vol. 17, no. 5, 1969, p 525.
44. M. Abramowitz et al., Handbook of Mathematical Functions,
Dover Publications, 1972.
45. M.C. Junger and D. Feit, Sound, Structures, and Their Interaction,
MIT Press, Cambridge, 1972.
46. J.D. Lambert, Computational Methods in Ordinary Differential Equations,
John Wiley, 1973.

Appendix A: Matrices of the thin shell differential equations.

The matrices A_{11}, A_{12} and A_{22} of Eq. 4.8 are given by:

$$A_{11} = \begin{bmatrix} \frac{2\pi Eh\sin^2(\varphi)}{r} - \omega^2\rho 2\pi rh & \frac{2\pi Eh}{r}\sin(\varphi)\cos(\varphi) & 0 \\ \frac{2\pi Eh}{r}\sin(\varphi)\cos(\varphi) & \frac{2\pi Eh}{r}\cos^2(\varphi) - \omega^2\rho 2\pi rh & 0 \\ 0 & 0 & \frac{2\pi Eh}{12r}\cos^2(\varphi) \end{bmatrix},$$

$$A_{12} = (A_{21})^T = \begin{bmatrix} 0 & \frac{1}{R_\varphi} + \frac{\nu}{r}\sin(\varphi) & 0 \\ -\frac{1}{R_\varphi} & \frac{\nu\cos(\varphi)}{r} & 0 \\ \frac{1}{h} & 0 & \frac{\nu\cos(\varphi)}{r} \end{bmatrix} \quad \text{and}$$

$$A_{22} = \begin{bmatrix} 0 & 0 & 0 \\ 0 & \frac{(1-\nu)^2}{Eh}\frac{1}{2\pi r} & 0 \\ 0 & 0 & \frac{12(1-\nu)^2}{Eh}\frac{1}{2\pi r} \end{bmatrix},$$

where R_φ is the radius of curvature in the meridional direction, E is the Young's modulus and ρ the density of the shell material, ω is the angular frequency, φ is the angle between the normal on the shell surface and the axis of symmetry, ν is Poisson's ratio, r is the distance from a shell element to the axis of symmetry and h is the shell thickness.

The coefficients B_{11}, B_{12}, B_{22}, C_1 and C_2 of Eq. 4.13 are given by:

$$B_{11} = \frac{2\pi\omega^2\rho r}{T}(\omega^2\rho r^2 - E),$$

$$B_{12} = B_{21} = \frac{-\nu\cos(\varphi)}{r} + \left(\frac{1}{R_\varphi} + \frac{\nu\sin(\varphi)}{r}\right)\frac{E}{T}\sin(\varphi)\cos(\varphi),$$

and

$$B_{22} = \frac{(1-\nu^2)}{2\pi rE} + \left(\frac{1}{R_\varphi} + \frac{\nu\sin(\varphi)}{r}\right)^2\frac{r}{2\pi T},$$

where

$$T = (E\sin^2(\varphi) - \omega^2\rho r^2).$$

$$C_1 = -\frac{E}{T}\sin(\varphi)\cos(\varphi),$$

and

$$C_2 = -\left(\frac{1}{R_\varphi} + \frac{\nu\sin(\varphi)}{r}\right)\frac{r}{2\pi T}.$$

The coefficients H_{11}, H_{12} and H_{22} of Eq. 4.21 are given by:

$$H_{11} = \frac{-2\pi\coth(\bar{z})}{\cos(\varphi)}\left(1 - \coth^2(\bar{z})\sin^2(\varphi)\right)$$

$$H_{12} = H_{21} = \nu\coth(\bar{z})$$

and

$$H_{22} = \frac{1 - \coth^2(\bar{z})(1-\nu^2)}{2\pi\cos(\varphi)\coth(\bar{z})}$$

where $\bar{z}$ is the complex variable as defined in Eq. 4.20.

Appendix B: The geometrical and material parameters of the loudspeaker cones that have been used in the numerical calculations discussed in Chapter 4.

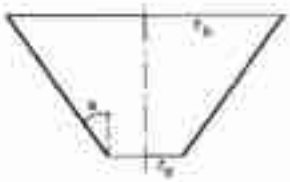

Fig. 4.6:

cone:			
inner radius	r_a	= 12.5	mm
outer radius	r_b	= 80	mm
semi-apex angle	α	= 60	degrees
cone thickness	h	= 0.55	mm
Young's modulus	E	= $1.9\,10^9$	N/m^2
mass density	ρ	= 310	kg/m^3
Poisson's ratio	ν	= 0.3	
loss factor	δ	= 0.1	
outer edge suspension:			
inner radius	r_a	= 80.5	mm
outer radius	r_b	= 89.5	mm
thickness	h	= 0.48	mm
radius of curvature	R_φ	= 4.5	mm
Young's modulus	E	= $8.0\,10^8$	N/m^2
mass density	ρ	= 540	kg/m^3
Poisson's ratio	ν	= 0.3	
loss factor	δ	= 0.2	

Fig. 4.7:

inner radius	r_a	= 15	mm
outer radius	r_b	= 80	mm
semi-apex angle	α	= 60	degrees
cone thickness	h	= 0.33	mm
Young's modulus	E	= $4.5\,10^9$	N/m^2
mass density	ρ	= 600	kg/m^3
Poisson's ratio	ν	= 0.3	
loss factor	δ	= 0.1	

Fig. 4.8:

inner radius	r_a	= 17	mm
outer radius	r_b	= 83	mm
semi-apex angle	α	= 50	degrees
cone thickness	h	= 0.23	mm
Young's modulus	E	= $2.2\,10^9$	N/m^2
mass density	ρ	= 1160	kg/m^3
Poisson's ratio	ν	= 0.3	
loss factor	δ	= 0.1	

Figs. 4.10, 4.11 and 4.12:

inner radius	r_a	= 12.5	mm
outer radius	r_b	= 80	mm
semi-apex angle	α	= 60	degrees
cone thickness	h	= 0.35	mm
Young's modulus	E	= $2.0\,10^9$	N/m^2
mass density	ρ	= 600	kg/m^3
Poisson's ratio	ν	= 0.3	
loss factor	δ	= 0	(Fig.4.10)
loss factor	δ	= 0.1	(Fig. 4.11)
loss factor	δ	= 0.1	(Fig. 4.12)

Figs. 4.14, 4.15, 4.16 and 4.17:

inner radius	r_a	= 12.5	mm
outer radius	r_b	= 80	mm
semi-apex angle	α	= 60	degrees
cone thickness	h	= 0.35	mm
Young's modulus	E	= $3.5\,10^9$	N/m^2
mass density	ρ	= 440	kg/m^3
Poisson's ratio	ν	= 0.3	
loss factor	δ	= 0.1	

radius of curvature R_φ is infinite (Fig. 4.14)
radius of curvature R_φ = 100 mm concave (Fig. 4.15)
radius of curvature R_φ = -100 mm convex (Fig. 4.16 and 4.17)

Fig. 4.18

cone:			
inner radius	r_a	= 12.5	mm
outer radius	r_b	= 80	mm
semi-apex angle	α	= 60	degrees
cone thickness	h	= 0.35	mm
Young's modulus	E	= $2.2\,10^9$	N/m^2
mass density	ρ	= 1160	kg/m^3
Poisson's ratio	ν	= 0.3	
loss factor	δ	= 0.1	
outer edge suspension:			
inner radius	r_a	= 80.5	mm
outer radius	r_b	= 89.5	mm
thickness	h	= 0.35	mm
radius of curvature	R_φ	= 4.5	mm
Young's modulus	E	= $0.05\,10^9$	N/m^2
mass density	ρ	= 1325	kg/m^3
Poisson's ratio	ν	= 0.5	
loss factor	δ	= 0.6	

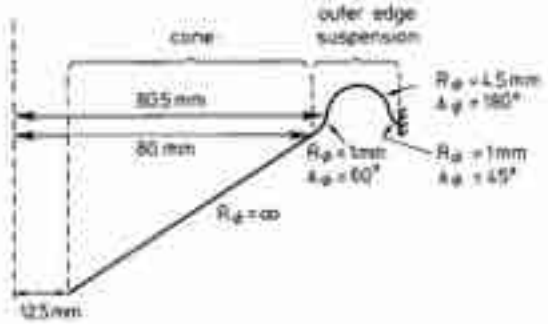

Appendix C: Parameters of Eqs. 6.9, 6.18, 6.20, 6.22 and 6.23

$$\alpha = k_0 R_E / Bl_0$$

$$\beta = (R_E R_m + k_0 L_{E_0} + Bl_0^2) / Bl_0$$

$$\gamma = (mR_E + L_{E_0} R_m) / Bl_0$$

$$\delta = mL_{E_0} / Bl_0$$

$$a = -2\, b_1 / Bl_0$$

$$b = (k_1 R_E Bl_0 + b_1 k_0 R_E) / Bl_0^2$$

$$c = (b_1 R_E R_m + 2 l_1 k_0 Bl_0 + 2 k_1 L_{E_0} Bl_0 + 3 b_1 Bl_0^2) / Bl_0^2$$

$$d = (b_1 mR_E + b_1 L_{E_0} R_m + l_1 R_m Bl_0) / Bl_0^2$$

$$e = (b_1 mL_{E_0} + l_1 mBl_0) / Bl_0^2$$

$$f = (l_1 R_m Bl_0 - b_1 L_{E_0} R_m) / Bl_0^2$$

$$g = (l_1 mBl_0 - b_1 mL_{E_0}) / Bl_0^2$$

$$A = (-2\, b_2 Bl_0 - b_1^2) / Bl_0^2$$

$$B = (k_2 R_E Bl_0 + b_2 k_0 R_E + b_1 k_1 R_E) Bl_0^2$$

$$C = (b_2 R_E R_m - b_2 k_0 L_{E_0} + 3 l_2 k_0 Bl_0 + 3 k_2 L_{E_0} Bl_0 + 3 b_2 Bl_0^2 + b_1 l_1 k_0 + 3 k_1 l_1 Bl_0 + b_1 k_1 L_{E_0} + 3 b_1^2 Bl_0) / Bl_0^3$$

$$D = (b_2 mR_E + b_2 L_{E_0} R_m + l_2 R_m Bl_0 + b_1 l_1 R_m) / Bl_0^2$$

$$E = (b_2 mL_{E_0} + l_2 mBl_0 + b_1 l_1 m) / Bl_0^2$$

$$F = (2\, l_2 R_m Bl_0 - 2\, b_2 L_{E_0} R_m) / Bl_0^2$$

$$G = (2\, l_2 mBl_0 - 2\, b_2 mL_{E_0}) / Bl_0^2$$

$$y_1 = a\,\{q_2(p_1,p_2) + q_2(p_1,p_3) + q_2(p_2,p_3)\}$$

$$y_2 = 2b\,\{q_1(p_1)q_2(p_2,p_3) + q_1(p_2)q_2(p_1,p_3) + q_1(p_3)q_2(p_1,p_2)\}$$

$$y_3 = c\,(p_1 + p_2 + p_3)\,\frac{y_2}{2b}$$

$$\begin{aligned} y_4 = {} & d\,(p_1^2 + p_2^2 + p_3^2 + 2p_2p_3)\,\{q_1(p_1)\,q_2(p_2,p_3)\} + \\ & + d\,(p_1^2 + p_2^2 + p_3^2 + 2p_1p_3)\,\{q_1(p_2)\,q_2(p_1,p_3)\} + \\ & + d\,(p_1^2 + p_2^2 + p_3^2 + 2p_1p_2)\,\{q_1(p_3)\,q_2(p_1,p_2)\} \end{aligned}$$

$$\begin{aligned} y_5 = {} & e\,(p_1^2 + p_2^2 + p_3^2 + 3p_2p_3(p_2 + p_3))\,\{q_1(p_1)\,q_2(p_2,p_3)\} + \\ & + e\,(p_1^2 + p_2^2 + p_3^2 + 3p_1p_3(p_1 + p_3))\,\{q_1(p_2)\,q_2(p_1,p_3)\} + \\ & + e\,(p_1^2 + p_2^2 + p_3^2 + 3p_1p_2(p_1 + p_2))\,\{q_1(p_3)\,q_2(p_1,p_2)\} \end{aligned}$$

$$\begin{aligned} y_6 = {} & 2fp_1(p_2 + p_3)\,\{q_1(p_1)\,q_2(p_2,p_3)\} + \\ & + 2fp_2(p_1 + p_3)\,\{q_1(p_2)\,q_2(p_1,p_3)\} + \\ & + 2fp_3(p_1 + p_2)\,\{q_1(p_3)\,q_2(p_1,p_2)\} \end{aligned}$$

$$\begin{aligned} y_7 = {} & g\,(p_1^2p_2 + p_1^2p_3 + p_1p_2^2 + p_1p_3^2 + 2p_1p_2p_3)\,\{q_1(p_1)\,q_2(p_2,p_3)\} + \\ & + g\,(p_1^2p_2 + p_1p_2^2 + p_2^2p_3 + p_2p_3^2 + 2p_1p_2p_3)\,\{q_1(p_2)\,q_2(p_1,p_3)\} + \\ & + g\,(p_1^2p_3 + p_1p_3^2 + p_2^2p_3 + p_2p_3^2 + 2p_1p_2p_3)\,\{q_1(p_3)\,q_2(p_1,p_2)\} \end{aligned}$$

$$Y_1 = 2A\,\{q_1(p_1)q_1(p_2) + q_1(p_1)q_1(p_3) + q_1(p_2)q_1(p_3)\}$$

$$Y_2 = 6B\,\{q_1(p_1)q_1(p_2)\,q_1(p_3)\}$$

$$Y_3 = 2C\,(p_1 + p_2 + p_3)\,\{q_1(p_1)\,q_1(p_2)\,q_1(p_3)\}$$

$$Y_4 = 2D\,(p_1^2 + p_2^2 + p_3^2)\,\{q_1(p_1)\,q_1(p_2)\,q_1(p_3)\}$$

$$Y_5 = 2E\,(p_1^3 + p_2^3 + p_3^3)\,\{q_1(p_1)\,q_1(p_2)\,q_1(p_3)\}$$

$$Y_6 = 2F\,(p_1p_2 + p_1p_3 + p_2p_3)\,\{q_1(p_1)\,q_1(p_2)\,q_1(p_3)\}$$

$$Y_7 = G\,\{p_1^2(p_2+p_3) + p_2^2(p_1+p_3) + p_3^2(p_1+p_2)\}\,\{q_1(p_1)\,q_1(p_2)\,q_1(p_3)\}$$

Summary

This thesis discusses the analysis and design of broadband electrodynamic loudspeakers and multiway loudspeaker systems.

After an introduction in chapter 1, chapter 2 presents a description of a lumped parameter model of an electrodynamic loudspeaker, in terms of an analogous electric circuit. Such a simple model can be used to derive many properties of the loudspeaker and serves as a basis for further discussions.

The application of the Wigner distribution in the analysis of the loudspeaker response is discussed in chapter 3. The Wigner distribution of a signal can be interpreted as a distribution of the signal energy in time and frequency. It is a basic time-frequency distribution, and it has properties that allow simple physical interpretations. Furthermore the Wigner distribution facilitates the interpretation of other time-frequency distributions since these distributions can be expressed as a convolution of the Wigner distribution and a weight function determined by the particular distribution considered. The Wigner distribution of the impulse response of a loudspeaker can therefore provide useful information about the transient behavior of the loudspeaker, and it enables a designer to formulate optimization criteria for this behavior.

The influence of the diaphragm break-up on the sound radiation can be predicted by calculating numerically the vibrations of a nonrigid loudspeaker diaphragm, which is the topic of chapter 4.

In chapter 5 the influence of the cone depth on the sound radiation is treated in section 1. In that section the sound radiation from a radiating surface is calculated by solving the Helmholtz equation numerically.

Sections 5.2 and 5.3 discuss the consequence of a crossover network in a multiway loudspeaker system for the transient response of the total system.

Finally chapter 6 gives an overview of possible nonlinearities in a practical electrodynamic loudspeaker and presents a model of the nonlinear loudspeaker behavior which can be used to predict the low frequency distortion of a loudspeaker.

Samenvatting

Dit proefschrift beschrijft de analyse en het ontwerp van elektrodynamische luidsprekers en meerweg-luidsprekersystemen.
Na een inleiding in hoofdstuk 1, geeft hoofdstuk 2 een beschrijving van het lumped-parameter model van een elektrodynamische luidspreker in de vorm van een elektrisch vervangingsschema. Een dergelijk eenvoudig model kan gebruikt worden om eigenschappen van een luidspreker te verklaren en dient als basis voor de verdere diskussies.
Hoofdstuk 3 bevat een diskussie van de toepassing van de Wigner-distributie in de analyse van de responsie van een luidspreker. De Wigner distributie van een signaal kunnen we interpreteren als de verdeling van de signaalenergie naar tijd en frequentie. Het is een basis tijd-frequentie verdeling en heeft een aantal eigenschappen welke een eenvoudige fysische interpretatie van de distributie mogelijk maken. Verder is de Wigner distributie geschikt voor het interpreteren van andere tijd-frequentie distributies, omdat die distributies geschreven kunnen worden als een konvolutie van de Wigner distributie en een weegfunktie welke bepaald wordt door de specifieke distributie. Daarom kan de Wigner distributie van een luidspreker nuttige informatie leveren omtrent het transient gedrag van die luidspreker en stelt het een ontwerper in staat om optimalisatie-kriteria voor dat gedrag te formuleren.
De invloed van het opbreken van het luidsprekermembraan op de geluidsafstraling kan voorspeld worden door numeriek de trillingen van een niet-stijf luidsprekermembraan te berekenen, hetgeen beschreven wordt in hoofdstuk 4.
De invloed van de konusdiepte op de geluidsafstraling wordt beschreven in hoofdstuk 5. In dat hoofdstuk wordt de geluidsafstraling van een stralend oppervlak berekend door de Helmholtz vergelijking numeriek op te lossen. Hoofdstuk 5 behandelt ook de invloed van het overnamefilter in een meerweg-luidsprekersysteem op het transient gedrag van de totale systeemresponsie.
Als laatste geeft hoofdstuk 6 een model dat de niet lineariteiten van een elektrodynamische luidspreker beschrijft, waarmee de laagfrequente vervorming van een luidspreker voorspeld kan worden.

Levensloop

Adrianus Jozef Maria Kaizer werd geboren te Amsterdam op 5 april 1950. In 1966 behaalde hij de diploma's MULO A en B en in 1969 het diploma HBS-B.

Hierna ging hij elektrotechniek studeren aan de Technische Hogeschool Twente te Enschede, waar hij in maart 1973 het baccalaureaatsexamen en in januari 1976 het doctoraal examen aflegde.

In januari 1976 trad hij in dienst van het Philips Natuurkundig Laboratorium en werkt sindsdien als wetenschappelijk medewerker in de groep "Acoustics and Noise Control".

Zijn werk concentreerde zich op het verbeteren van elektro-akoestische omzetters en omvatte onder andere de numerieke analyse van de trillingen en de geluidsafstraling van luidspreker membranen, het toepassen van CAD technieken in de elektro-akoestiek, het analyseren van het niet-lineaire gedrag van een elektrodynamische luidspreker en het ontwerp van aktieve luidsprekerboxen.

STELLINGEN

bij het proefschrift van A.J.M. Kaizer
14 januari 1986, Technische Hogeschool, Eindhoven

1

Een geschikte grootheid voor het beoordelen van het (akoestisch) transient gedrag van een luidspreker in een reflektie-vrije ruimte is de Wigner-distributie van de (akoestische) impulsresponsie van die luidspreker in die ruimte.

(Dit proefschrift hoofdstuk 3).

2

De meest geschikte vorm van een luidsprekerkonus wordt bepaald door de mechanische eigenschappen van het konusmateriaal.

(Dit proefschrift hoofdstuk 4).

3

Het maximale vermogen dat een luidspreker kan verwerken wordt gedefinieerd als U^2/R. De grootheid U is de effectieve waarde van de maximaal toe te laten spanning van het testsignaal op de luidsprekerklemmen en R is een door de fabrikant op te geven nominale weerstand van de spreekspoel. De waarde van R mag niet groter zijn dan 1,25 maal de minimale waarde van de modulus van de ingangsimpedantie van de luidspreker in het (frekwentie-)werkgebied. Wat echter ontbreekt is een specifikatie van de minimale waarde van R.

(IEC 268-5, punten 3.2.2b en 15.1).

4

Een elektrodynamische luidspreker wordt meestal zodanig ontworpen dat in het werkgebied van de luidspreker de amplitude van de door de luidspreker geproduceerde geluidsdruk, gemeten in een punt in een reflektie-vrije ruimte, als funktie van de frekwentie bij konstante elektrische ingangsspanning zo goed mogelijk onafhankelijk is van de frekwentie. Dit legt beperkingen op aan het rendement van die luidspreker.

(L.L. Beranek, Acoustics, McGraw-Hill, New York, 1954.)

5

Voor het verminderen van de niet-lineaire vervorming in een elektrodynamische luidspreker wordt dikwijls gebruik gemaakt van een tegenkoppeling gestuurd door de stroom door of de spanning over de spreekspoel. Een

tegenkoppeling gestuurd door het signaal van een aparte mechanische bewegingsopnemer op de spreekspoelkoker kan echter betere resultaten leveren, omdat deze ook de vervorming tengevolge van het plaatsafhankelijke statische magneetveld onderdrukt.

(P. Scherer and B. Dick, Controlling the sound pressure by controlling the movement of the diaphragm, Proc. of the 77th Conv. of the Audio Eng. Soc., no 2208, Hamburg, 1985.)

6

De neiging van een papieren luidsprekerkonus tot het genereren van subharmonischen neemt toe met de malingsgraad van het papier. Dit zou verband kunnen houden met het feit dat papier met een hogere malingsgraad een grotere stijfheid bezit.

(P.O. Pedersen, Sub-Harmonics in Forced Oscillations in Dissipative Systems, Danmarks Naturvidenskabelige Samfund, Ingeniorvidenskabelige Skrifter A 35, Copenhagen, 1933.)

7

De eis dat, gemeten in een reflektie-vrije ruimte, de modulus van de overdrachtsfunktie van een elektro-akoestisch weergavesysteem onafhankelijk is van de frekwentie, lijkt tegenstrijdig te zijn met het feit dat de overdrachtsfunktie van een ruimte waarin zo een systeem gebruikt wordt, zeer grillig is. Men moet echter, gebaseerd op psycho-akoestische gronden, onderscheid maken tussen het direkte geluid en de galm.

(J. Blauert, Spatial Hearing, MIT Press 1983.)

8

De penetratie van digitale technieken in de totale elektro-akoestische keten, inclusief de generatie en de perceptie van geluid, heeft een natuurlijke grens: een geluidsgolf laat zich niet digitaliseren, het menselijk oor evenmin.

(B. Blesser, Digitalization of Audio, J. Audio Eng. Soc., vol. 26, no 10, pag. 739, 1978.)

9

„The purpose of computing is insight, not numbers." (R.W. Hamming) Daarom verdient het aanbeveling om in een kollege numerieke wiskunde aan een Technische Hogeschool ook enige aandacht te besteden aan het gebruik van computeralgebra.

10

Het gebruik van niet-FORTRAN programmeertalen wordt bemoeilijkt doordat de meeste bestaande programmabibliotheken geschreven zijn in FORTRAN. Het verdient daarom aanbeveling bij de specifikatie van een programmeertaal ook de aanroepwijze van een in FORTRAN geschreven programma op te nemen.

11

Het optimaliseren van de responsiefunktie van een optisch systeem in gangbare rekenpaketten gebeurt via een minimalisatie van de golffrontfouten of van de geometrische dwarsaberraties. Dit levert echter nogal uiteenlopende eindresultaten op. Het verdient dan ook aanbeveling om als doelfunktie van de minimalisatie een kombinatie van de genoemde fouten te nemen.

(Code V User's manual, Chapter 5, Optical Research Associates, Pasadena California, 1982.)

12

In de akoestiek en soortgelijke disciplines wordt gebruik gemaakt van soms zeer verfijnde numerieke analyse- en optimalisatietechnieken. Een systematische synthese zoals we die uit de netwerktheorie kennen, zal echter bij dergelijke compliceerde continue fysische systemen, door het grote aantal vrijheidsgraden, vrijwel onmogelijk zijn. Daarom zal de invoering van numerieke technieken in het ontwerpproces nooit de vindingrijkheid van de ontwerper overbodig maken.

(R.P. de Wit, A.J.M. Kaizer and F.J. Op de Beek, Numerical Optimization of the Cross-Over Filters in a Multiway Loudspeakersystem, Proceedings 75th Convention of the Audio Engineering Society, no. 2057, Paris, 1984.)

13

Bij het oplossen van knelpunten in ons wegennet wordt vaak eerst gedacht aan een vergroting van de capaciteit. Echter, gezien de krapte in de overheidsfinanciën zouden alle middelen om de bezettingsgraad van auto's te vergroten, bijvoorbeeld het „poolen" in het woon-werkverkeer, eveneens overwogen dienen te worden.